MICROPHYSIOLOGICAL SYSTEM WITH CONTINUOUS CONTROL AND SENSING OF OXYGEN ELUCIDATES HYPOXIC INTESTINAL EPITHELIAL STEM CELL FATES

Kristina R. Rivera

A dissertation submitted to the faculty at the University of North Carolina at Chapel Hill in partial fulfillment of the requirements for the degree of Doctor of Philosophy in the Department of Biomedical Engineering.

Chapel Hill
2020

Approved by:

Michael Gamcsik

Michael Daniele

Scott Magness

Anthony Blikslager

Dror Baron

ABSTRACT

Kristina R. Rivera: Microphysiological system with continuous control and sensing of oxygen elucidates hypoxic intestinal epithelial stem cell fates
(Under the direction of Scott Magness and Michael Daniele)

Providing primary human stem cells with the optimal environmental factors required to promote expansion and differentiation is no trivial task in biomedical research. Many diseases and pathologies are caused by deficiencies in oxygen supply or regulation. Here, intestinal ischemia/reperfusion injury is presented as an example to highlight the detrimental impact of loss of oxygen, i.e. hypoxia, on the intestinal epithelium. This dissertation focuses on oxygen as one key environmental factor that must be monitored to mediate cell death and facilitate cell expansion. Typical tissue culture platforms, such as polystyrene well plates or flasks, cannot supply adequate oxygen to cells nor measure oxygen concentrations at the cell-media or cell-tissue interface. A microphysiological system (MPS) provides an advantageous platform to design and fabricate more physiologically relevant cell culture microenvironments that can be continuously monitored in real-time. Oxygen can also be controlled in MPS using the appropriate materials, and, furthermore, oxygen can be monitored with many integrated sensors. Here, two MPS are designed and built to investigate the role of severe tissue hypoxia on (i) tumorigenesis in breast epithelial tissue and (ii) on stem cell function, i.e. proliferation and pluripotency, in the intestinal epithelium. Oxygen monitoring is performed in each MPS using embedded micro-hydrogel oxygen sensors via phosphorescence detection. For the study of hypoxia on intestinal epithelial stem cell function using the developed MPS, significant molecular biology, including bulk and single cell RNA sequencing, data is also presented.

To my baby sister Juliana Rosa Rivera; I miss you forever.

ACKNOWLEDGEMENTS

Many integral people supported and encouraged me while I was here. I thank Dr. Magness for welcoming me into UNC. I never knew I loved Cheez-It® as much as I did, thank you Leigh Ann (Dr. Samsa) for the snacks and wisdom. I never knew a lab meeting on animal handling could be so enjoyable, thank you Bailey (Dr. Zwarycz) for the beautiful, delicious chocolate cherry mice and kindness. I am thankful to all my Magness lab mates, especially Dr. Ian Williamson for the engineering tips and words of support in life/love. I thank my crew at the BioInterface Lab at NC State University. Everyone had my back from start to finish, especially the fearless leader Dr. Daniele. I especially want to thank Dr. Vladimir Pozdin for the research help, and Dr. Ashlyn Young for teaching me all her tricks to making hydrogels for happy cells.

I am thankful for my family. Titi Elaine thanks for letting us crash at your house (twice!) while visiting Orlando and Miami for conferences. Thank you, older sis Alinessa for the support and cheer of seeing Anahi growing up in pictures from AZ; I hope to return to the west soon. Thank you, older bro Nate and wifey Jocelyn for the food and treats whenever I needed to take a break and come to Greensboro. Thank you, Sami and Angelina, my darling little sisters, for texting me and keeping me in the know, although I rarely replied or only sent a single emoji. Thank you, baby bro Henry for telling me to “do good in college”. And thank you momma and daddy for paying my health insurance and printing off my presentations to take to work. Tyler Gilmore, thank you for getting me a bicycle to ride to lab and also picking me (and my bike) up from lab when it was raining, and I just couldn’t do it anymore. To many more years together.

TABLE OF CONTENTS

LIST OF TABLES

LIST OF FIGURES

LIST OF ABBREVIATIONS

6G	6-Gingerol
BNIP3	BCL2 (B-cell lymphoma 2) interacting protein 3
BT474	Non-metastatic tumorigenic human breast epithelial cells
CAB	Cellulose acetate butyrate
CO_2	Carbon dioxide
CT	Clark-type
E. coli	*Escherichia coli*
ECM	Extracellular matrix
FACS	Fluorescence-activated cell sorting
FEA	Finite element analysis
FLIM	Fluorescence lifetime imaging microscopy
GelMA	Gelatin methacrylamide
H/R	Hypoxia/Reoxygenation
H_2O_g	Gaseous water
HIF-1	Hypoxia-inducible factor 1
HIF1A	Hypoxia-inducible factor 1α
HIMEC	Human intestinal microvascular endothelial cell
hiPS	Human induced pluripotent stem cells
hiPSCs	Human induced pluripotent stem cells
HUVEC	Human umbilical vein endothelial cells
I/R	Ischemia/Reperfusion
IBD	Inflammatory bowel disease

IHC	Immunohistochemical
IL6	Interleukin-6
IL10	Interleukin-10
IL22	Interleukin-22
iNOS	inducible nitric oxide synthase
iPOB	Integrated Phosphorescence-based Photonic Biosensor
ISC	Intestinal stem cell
kPa	kilopascal
LED	Light emitting diode
LGG	*Lactobacillus rhamnosus GG*
M30	Cytokeratin 18
MCF-10A	Immortalized benign human breast epithelial cells
MDCK	Madin-Darby canine kidney cells
MFY	Macrolex Fluorescent Yellow
MIMEC	Murine intestinal microvascular endothelial cells
mmHg	Millimeters of mercury
MPO	Myeloperoxidase
MPS	Microphysiological system
MUC3	Mucin 3
N_2	Nitrogen gas
NEAA	Non-essential amino acid
NHEK	Normal human epidermal keratinocytes
NIR	Near infrared

NO	Nitric oxide
Nurr1	Nuclear receptor-related protein 1 murine gene
OFE	Organoid forming efficiency
P. aeruginosa	*Pseudomonas aeruginosa*
Parylene-C	Poly(chloro-p-xylyene)
PC	Polycarbonate
Pd-BPD	Palladium-benzoporphyrin derivatives
Pd-TCPP	Palladium-meso-tetra (4-carboxyphenyl) porphyrin
PDDA	Poly(diallyl dimethylammonium)
PDMS	Polydimethylsiloxane
PdTPTBPF	Palladium(II) meso-tetra(4-fluorophenyl) tetrabenzoporphyrin
PET	Polyethylene terephthalate
pHEMA	Poly(2-hydroxyethyl methacrylate
PMMA	Polymethyl methacrylate ()
pO_2	Partial pressure of oxygen
Pt-OEPK	Platinum octaethylporphine-ketone
PtOEP	Platinum octaethylporphyrin
PtTFPP	Platinum (II)-5,10,15,20-tetrakis-(2,3,4,5,6-pentafluorphenyl) porphyrin
PtTPTBPF	Platinum(II) meso-tetra(4-fluorophenyl) tetrabenzoporphyrin
PVC	Poly(vinly chloride)
qRT-PCR	Quantitative real-time polymerase chain reaction analyses
ROS	Reactive oxygen species
SLC2A1	Solute carrier family 2 member 1

SMA	Superior mesenteric artery
TER	Transepithelial electrical resistance
Tff3	Intestinal trefoil factor 3 murine gene
VEGF	Vascular endothelial growth factor

CHAPTER 1: MODELS OF INTESTINAL PHYSIOLOGY

1.1. Cellular Components of the Human Small Intestine

In the small intestine, a crypt and villus architecture supports an epithelial monolayer that absorbs nutrients and maintains a barrier against luminal contents and bacteria. The epithelial monolayer is rapidly renewed by a pool of intestinal stem cells (ISCs) located at the base of the crypt (**Fig. 1.1**). The epithelial lining of the small intestine absorbs and transports nutrients while maintaining a protective barrier against environmental pathogens.[1] Intestinal epithelial cells respond to stimuli from adjacent cells and their surrounding microenvironment to regulate cell turnover, cell death and detachment (anoikis), proliferation, and differentiation.[2] ISCs, located at the base of the intestinal crypt between Paneth Cells, are essential to initiate physiologic self-renewal of all differentiated cells that make up the intestinal epithelium. At the crypt base, Paneth Cells are responsible for secreting antimicrobial peptides and enzymes to protect the epithelium from microbes and provide critical growth factors to support ISC survival and differentiation.[3, 4] Paneth Cells can be identified via expression of Lysozyme and other Defensins.[5] Above the crypt base are transit amplifying cells, which undergo up to five rounds of cell division during a 48-hour cycle, differentiating to become one of four main intestinal epithelial cell lineages (**Fig. 1.1**).[6] The differentiated intestinal epithelial cell lineages include absorptive enterocytes, often marked by Alkaline Phosphatase expression, goblet cells (marked by Mucin 2,3)[7], enteroendocrine cells (marked by Chromogranin A)[8], and tuft cells (marked by Dcamk1)[9], Paneth cells and M Cells.

Migrating from the crypt and entering the villus region of the epithelium, there is a unique geometric interplay between the cell population and the environment that gives rise to differentiation, form, and function. Microvascular networks exist within villi and provide oxygenated blood flow to the epithelial barrier. The amount of microenvironmental oxygen available to each intestinal epithelial cell depends largely on the location of the cell along the crypt-villus axis.

The microenvironment of the intestinal epithelium is characterized by a steep oxygen gradient. The molecular oxygen concentration levels from the outermost, serosal aspect of the small intestine are significantly lower than those of the inner submucosa.[10] While the gut lumen is nearly entirely oxygen-depleted or anoxic, the mucosa is highly perfused by oxygen via the vast capillary bed surrounding the microarchitecture of the crypts and villi.[11] Despite an underlying microvascular network, compared to oxygen-rich tissues of the human body such as the arteries, alveoli, and the trachea (physiological oxygen levels from 13% to 18%), the low oxygen (approximately 8% O_2) environment of intestinal tissue constitutes a state of physiologic hypoxia.[12] A common feature of a number of GI-related health conditions occurs when there are extensive periods of severe lower oxygen availability (less than 8% O_2) in the intestinal tissue.[13] Although long term pathophysiologic hypoxia can lead to detrimental intestinal damage, little is known about how the duration and magnitude of hypoxia, particularly acute ischemia injuries, impact ISC function.

1.2. Physiological Consequences of Ischemia and Hypoxia in the Small Intestine

Intestinal ischemia (blockage of blood flow and nutrients) is an aggressive disease state often diagnosed after the onset of necrosis in the bowel, offering few treatment options, and, consequently, is associated with high morbidity and mortality.[14] Dysregulation of normal ISC-

driven epithelial renewal causes a loss of the epithelial barrier, inflammation, and, in severe cases, death. During intestinal ischemia, if the reduction in dissolved oxygen concentration (hypoxia) goes unresolved, then irreversible cellular damage can occur.[15-17]

Ischemic injury occurs when blood flow is interrupted for a short (minutes) or long (hours) period of time and is often caused by surgery (for abdominal aortic aneurysm, small bowel transplantation, strangulated hernias, or neonatal necrotizing enterocolitis), collapse of systemic circulation during hemorrhagic or septic shock, or heat stress.[18] There exist both occlusive and non-occlusive (surgeries) causes for intestinal ischemia. Occlusive causes, such as abdominal aortic aneurysms, acute mesenteric thrombi, and mesenteric emboli, involve a blockage in circulation, such as from a blood clot or even an air bubble trapped in vessels (**Fig. 1.2**). If the blockage is resolved, a second tissue insult from reperfusion injury can occur when return of blood flow initiates a complex cascade of events, including pro-inflammatory cytokine release and increase in harmful reactive oxygen species (ROS) that damage cells and degrade extracellular matrix components beneath the epithelium.[19]

The intestinal microvascular network is the first responder to ischemic damage, as ischemia is presented as a blockage in blood flow. The suspended blood flow causes subsequent inadequate supply of oxygen to the affected tissue (**Fig. 1.2**). Decreased oxygen during ischemia causes mucosal epithelial cell damage, including sub-epithelial lifting and villi tip sloughing.[20] Prolonged ischemia (50+ minute) furthermore prevents the exchange of nutrients and oxygen to the epithelium, causing epithelial cell apoptosis and loss of membrane integrity when all villous epithelium sloughs off, leaving the crypt is severely damaged.[21]

Mechanisms leading to irreversible damage of the intestinal epithelium following reperfusion are well-documented.[22, 23] During ischemia, hypoxanthine builds up and xanthine oxidase is

produced from xanthine dehydrogenase. Once oxygen is reintroduced during reperfusion, xanthine oxidase reacts with oxygen to produce dangerous ROS, including superoxide. Superoxide further damages the epithelial cell membrane via peroxidation, increasing neutrophil activation and inflammation. Oxidative injury continues as more ROS are released by neutrophils. At the cellular level, ischemic injury decreases mitochondrial Adenosine Triphosphate generation and cell membrane selective permeability.[24] As the duration of ischemia increases, epithelial cells that line the intestinal lumen lose their attachment to the basement membrane and become necrotic.[15] Furthermore, the duration of intestinal ischemic insult is directly proportional to the severity of mucosal injury.[20, 25, 26] *In vivo* ischemia models have revealed that short-term (15 minute) ischemic damage appears to be reversible in murine jejunum, with rapid initiation of repair mechanisms in the intestinal epithelium, while long-term (50+ minute) is predominantly irreversible.[21] Determining important time dependent epithelial repair mechanisms could mitigate ischemic injuries.

1.3. HIF-1 Activation During Ischemia

From the initial ischemic event to the restoration of blood flow, many signaling pathways are activated in the intestine during Ischemia/Reperfusion (I/R) injury that lead to substantial infiltration of pro-inflammatory mediators to and from distant organs.[14] To understand how to mitigate intestinal damage and injury to distant organs, the events and pathways activated during either ischemia or reperfusion must be segregated and studied in depth. To allow for in depth studies of ischemia, cells and tissues must be removed from native vasculature and never re-exposed to environmental oxygen.

At the molecular level, ischemia triggers the master transcriptional factor hypoxia-inducible-factor-1 (HIF-1) to stabilize and translocate to the nucleus, where it reprograms genes

to regulate epithelial cell response to low oxygen.[27] While HIF-1 dependent mechanisms have primarily been studied in differentiated epithelial cells or colon cancer cell lines and are known to impart a number of protective phenotypes, the impact of the ischemia on the self-renewal and differentiation capacity (i.e. stemness) of ISCs has not been studied.[28, 29] Immunohistochemical analyses of normoxic healthy human intestinal epithelium reveal HIF-1 expression is absent in the proliferative crypt and importantly demonstrate that the HIF-1 activation mechanisms are not engaged and have adapted to physiologic hypoxia.[30] However, hypoxic conditions imposed during ischemic injury result in an upregulation of HIF-1, suggesting a key role for HIF-1 in ISC function.[31] Murine ischemia models of the intestinal jejunum have shown that the long-term (50 min) ischemia causes a dramatic reduction in epithelial cell viability and membrane integrity.[21] As long-term ischemia causes reduced cell viability and influences HIF-1 stabilization along the crypt-villus axis, the duration of ischemic injury may influence ISC survival.

Ischemia triggers a key transcriptional response governed by hypoxia-inducible factors (HIFs) normally repressed by a family of oxygen-sensing HIF hydroxylases under normoxic conditions.[32] During ischemia, hydroxylases can no longer hydroxylate HIF-1α subunits due to the lack of available molecular oxygen as a co-factor, thereby allowing for HIF-1 stabilization and translocation to the nucleus, producing transcriptionally active complexes.[33] Functional HIF transcription factors trigger changes in the gene expression of many vital proteins that control epithelial response to ischemic conditions, including proteins activated during cell proliferation and death.[27] Because intestinal epithelial cells normally experience a low oxygen level on their apical surface that would be severely hypoxic in other tissues, precise oxygen

sensing is crucial to keep oxygen levels from dropping below threshold levels that impair cell viability and function.

It is known that ischemia increases the expression of differentiation markers, including goblet cell marker Mucin 3 (MUC3), in a HIF-1-dependent manner in mature intestinal epithelial cells.[34] HIF-elicited intestinal protection can also occur through anti-inflammatory pathways.[35] For example, increased expression of HIF-1 in intestinal epithelial cells from IBD patients suggests HIF-1 improves barrier protection and prevents epithelial cell apoptosis.[36] In a similar study, conditional knockout of HIF-1 expression in intestinal epithelial cells exacerbated barrier injury and resulted in more severe symptoms in a murine colitis model.[35] Furthermore, the barrier-protective protein intestinal trefoil factor (*Tff3*) gene, which is induced during hypoxia, has a binding site for HIF-1 in its promoter.[31] *Tff3* activation by HIF-1 may be important to restore the epithelial barrier post-ischemic injury.

As HIF-1 expression correlates with oxygenation, the absence of HIF-1 in the intestinal crypt and presence of mature intestinal epithelial cells in the intestinal lumen corresponds to the oxygen gradient present during physiologic hypoxia. This localization also supports the notion that exposure to ischemia is important to trigger HIF-1 target genes, such as *Tff3*, that are essential for intestinal lumen barrier formation and injury repair in the intestinal mucosa. Hypoxic conditions result in both a mobilization of HIF-1 and an upregulation of HIF-1 expression, suggesting a protective role for HIF-1 in the intestinal epithelium and ISCs.[31] In other stem cell types, including breast cancer stem cells and embryonic stem cells, ischemia and hypoxia cause increased proliferation and pluripotency in a HIF-1 dependent manner.[37-39] The potential for intestinal stem cell protection and expansion *in vitro* following a short or long

duration of hypoxia could facilitate enhanced mucosal epithelial regeneration and will be investigated further in Chapter 4.

1.4. Animal Models to Study Intestinal Ischemia

In the 1990s, studies of I/R injury in animals began by first occluding the Superior Mesenteric Artery (SMA) for 10 to 60 minutes with microvascular clamps (to represent an ischemic event) and then reperfusion was performed for 2 to 6 hours.[40] Results from these initial animal studies in rats revealed I/R injury caused intestinal lipid absorption issues, along with necrosis and apoptosis of intestinal epithelial cells.[25, 41] The SMA occlusion model of I/R injury in rodents was also used to investigate how luminal nutrients, like arginine and glutamine, impacted the production of inflammatory mediators like inducible nitric oxide synthase (iNOS) and myeloperoxidase (MPO). One study used intestinal sacs filled with glutamine or arginine in conjunction with SMA occlusions to show that arginine, but not glutamine, increased iNOS and gut mucosal injury.[42] This finding was insightful, as arginine is a precursor of nitric oxide, which reacts with superoxide ions present during reperfusion and produces a highly toxic oxidant called peroxynitrite.[43] Although arginine had been previously considered a luminal nutrient, this study provided support for a harmful role of arginine in I/R injury due to enhanced iNOS production. Generally, the presence of iNOS during I/R injury further exacerbates injury to the intestine, as nitric oxide (NO) is a byproduct of iNOS that causes cell apoptosis and inflammatory injury. This study suggests reperfusion-based NO production can exacerbate ischemic injury to the intestine.

Another animal study of NO production sought to unravel the protective effect of the female sex hormone estradiol on acute lung inflammation induced during intestinal I/R.[44] Female rats were subject to ischemia via SMA occlusion after receiving an ovariectomy and a

single injection of 17b-estradiol. The authors found that, as compared to control female rats that received I/R without an ovariectomy, ovariectomy rats had enhanced microvascular permeability and increased MPO activity in pulmonary tissue, indicative of neutrophil sequestration into the lungs. Treatment with estradiol recovered extravasation levels in the lungs of ovariectomy rats. In contrast, treatment with a NOS inhibitor (aminoguanidine) increased MPO activity in the lung of intestinal I/R-injured rats that underwent ovariectomy. Overall, this study revealed that in the absence of ovaries female rats develop substantial dye extravasation (permeability) and MPO activity in the lungs following intestinal I/R. These results are in stark contrast to those of normal, untreated female rats that were subject to intestinal I/R alone and had no inflammatory lung responses. Estradiol exhibits an anti-inflammatory effect on the lung during I/R injury, but the mechanism of action causing lung injury after intestinal I/R remains to be determined.

As the above study highlights, animal models of I/R injury can reveal important relationships between the intestine and distant organs during this mode of injury. Despite these important findings, *in vivo* models of I/R injury are not standardized across studies or species. Recently, many animal studies of I/R injury have included 45 minutes of ischemia via SMA occlusion followed by 1.5 to 2 hours of reperfusion.[44-46] Although these times for ischemia and reperfusion are commonly used to recapitulate I/R injury, there are also recent studies using either shorter or longer periods of ischemia and longer periods of reperfusion (more similar to the studies performed in the 1990s).[47-49] These differences in durations of occlusion and reperfusion make interpreting findings across studies confounding and comparing results problematic. Species differences also complicate potential translation of research findings. Small animal models of I/R injury are pathophysiologically different than humans, as rodents have a high number of oxygen generating enzymes that are absent in human tissues. Rodent I/R injuries

are also difficult to create surgically due to microscale features and high mortality rate, rendering the results from rodent models less predictive.[50]

1.5. Human Models to Study Intestinal Ischemia

While animal models may allow for some controlled experimental parameters and methods, they may not accurately reflect human pathophysiology due to morphological differences in mucosal epithelial cell populations compared with humans.[50] To study I/R injury in humans, intestinal tissues can be collected from patients who have undergone traumatic injuries (vehicle collisions, gunshot wounds, soldiers in battle, etc.) or received elective bowel resections. The intestinal tissues obtained intraoperatively from patients with acute traumatic injuries can be compared to control bowel resection tissues. Human studies of I/R injury have revealed many interesting findings regarding intestinal epithelial damage and repair mechanisms.

Clinicians have been able to investigate intestinal epithelial cell and lymphocyte apoptosis by using intestinal tissue samples obtained from patients with acute traumatic injuries and comparing them to patient samples from elective bowel resections.[51] From a cohort of 10 trauma tissues and 6 normal tissues, the authors found that trauma tissues from the highest injury severity scores also had the most severe apoptosis. Using Hematoxylin and Eosin and caspase-3 and cytokeratin 18 (M30) immunohistochemical staining, M30+ epithelial cells and Caspase-3+ lymphocytes with morphological changes in the form of cell shrinkage with condensed nuclei (pyknosis) and nuclear fragmentation (karyorrhexis) were considered apoptotic. By following two trauma patients from their first to their second operations, the researchers found a reduction in apoptosis in intestinal epithelial cells and lymphocytes in the second operation as compared to the first. Overall, focal apoptosis in both cell types occurred rapidly (within the first 2 to 3 hours) after injury and may support a mechanism for bacterial translocation into the systemic circulation

and a predisposition to infection following bowel injury. The authors of this clinical study showed for the first time that the apoptotic mechanism of cell death in lymphocytes and intestinal epithelial cells is conserved between animal models and human patients that suffered from shock and trauma.

Another option to study an I/R injury in a human model is to coordinate with patients before elective surgeries. For example, intestinal I/R models have been employed in humans undergoing Roux-en-Y gastric bypass or pancreaticoduodenectomy. Before removal from a patient, a normal segment of jejunum is isolated and subject to 30 to 45 minutes of mesenteric vascular occlusion, with varying lengths of reperfusion.[16, 52, 53] The newly I/R-injured intestinal segment is then resected, preserved, and processed for downstream analysis. Results from studies of experimental human intestinal I/R damage have shown that the human small intestine is resistant to short (30 minute) ischemic periods, with the jejunal epithelial lining remaining intact, and that reperfusion can cause intestinal damage that is rapidly restored, limiting inflammation.[53] These findings contrast similar animal studies that show short ischemia, when followed by reperfusion, can still cause an inflammatory response.[54-56] In a prolonged (45 minute) ischemic injury followed by reperfusion, the human jejunal intestinal barrier showed integrity loss, significant translocation of endotoxin, and an inflammatory response that included endothelial activation and release of proinflammatory mediators into the circulatory system. Although prolonged I/R injury in humans showed similar inflammatory responses as those seen in animals, it is unlikely that a comprehensive inflammatory response could be observed before intestinal tissues had to be resected from the patients and preserved.

Controlled human studies of ischemic injury are only possible during intestinal reconstruction surgeries and do not recapitulate the magnitude (% oxygen available) or duration

of ischemic damage typically experienced during severe hypoxia, and rodent models likely do not accurately represent pathophysiological I/R injury in humans.[50] Studies utilizing bypass patient tissues are limited in terms of their significance because patients suffering from ischemic injury experience much more severe ischemic damage than possible during these clinical studies performed in the middle of elective surgeries. Additionally, cellular resolution and statistically robust controlled perturbations (i.e. biological replicates) are substantially limited with these *in vivo* studies.

1.6. *In Vitro* Models to Study Hypoxia/Reoxygenation

Conventional *in vivo* ischemic injury studies are often performed along with restitution of oxygen (reperfusion) and lack spatial control of the oxygen conditions inside the intestinal tissue. To address this concern *in vitro*, hypoxic chambers are used to culture epithelial cells in low oxygen environments for an experimentally defined duration of time. Following hypoxic conditioning, cells are transferred to a normoxic incubator for reoxygenation, the *in vitro* equivalent to reperfusion. Recently, Y. Li et al. discovered 6-Gingerol (a main pungent principle of ginger) protected the intestinal barrier from I/R-induced damage using both a rat intestinal I/R model and Caco-2 cells incubated under hypoxia/reoxygenation (H/R) conditions.[45] For the animal intestinal I/R model, rats, pretreated with or without intragastrically administered 6-Gingerol (6G) for 3 days, were subject to 45 minutes of SMA occlusion ischemia followed by 90 minutes of reperfusion. For the H/R *in vitro* culture, Caco-2 cells, pretreated with a range of 6G concentrations, were incubated in a microaerophilic system containing 1% oxygen, 5% carbon dioxide, and 94% nitrogen gas for 12 hours, and then cells were moved to a normobaric incubator to be cultured for 6 hours under normoxic (18.5% oxygen gas) conditions. Authors of

this study found that the 6G pretreatment reduced villus injury and maintained goblet cell viability in the intestine histological samples. Moreover, the 6G pretreatment reduced expression of proinflammatory cytokines (TNF-α, IL-6, IL-1b) and neutrophil infiltration (MPO) as quantified using ELISA kits. Cell viability measurements revealed mid to high concentrations of 6G significantly enhanced cell viability, as compared to untreated H/R-injured Caco-2 cells. ROS production was also decreased in the 6G pretreated Caco-2 cells in a concentration-dependent manner. Both *in vivo* and *in vitro* results align and support the conclusion that 6G attenuated intestinal I/R injury.

I/R injury is associated with increased intestinal barrier permeability as the epithelial barrier loses cells to apoptosis or necrosis. To study intestinal barrier permeability in *in vitro* cell culture systems, measurements of Transepithelial electrical resistance (TER) are often performed on monolayers of epithelial cells cultured on protein-coated permeable polycarbonate membranes inside Transwells. Transwell inserts are used inside a standard 24-well plate but remain suspended approximately a millimeter above the bottom of the well.[57] TER is measured across the epithelial monolayer using chopstick electrodes placed inside the Transwell insert and beside the insert inside the same well. High TER is associated with high resistance and corresponding low barrier permeability, whereas low TER signals a more permeable or potentially impaired barrier. Using a Transwell seeded with porcine intestinal epithelial cells, Yang et al. found that non-essential amino acid (NEAA) deprivation impaired barrier function.[58] In the absence of NEAA in the culture medium, impaired barrier function caused a significant reduction in TER, along with a reduction in the levels of important tight junction proteins, claudin-1 and ZO-1. This study showed a potential NEAA pathway influencing

epithelial apoptosis and barrier repair following injury where the addition of a NEAA could promote epithelial barrier restoration.

In another recent study that used Transwell cell cultures and TER measurements, Caco-2 cells exhibited reduced TER when a gene called nuclear receptor-related protein 1 (*Nurr1*) was knocked down.[59] Animal studies in mice showed enhanced intestinal epithelial proliferation and barrier function when mice were treated with a *Nurr1* activator. The mice that received treatment had increased Occludin and ZO-1 protein expression, which supports the theory that *Nurr1* may improve intestinal barrier restoration following I/R injury. Inhibition of the *Nurr1* suppressor (miR-381-3p) in intestinal epithelial cells exposed to H/R conditions helped to mitigate paracellular permeability, as evident from decreased FITC-dextran leakage into the basal media from the Caco-2 cell monolayer on the Transwell membrane. Moreover, measurements of Ki-67 immunofluorescence showed that anti- miR-381-3p elevated epithelial proliferation. These findings both *in vitro* and *in vivo* boast the therapeutic potential of miR-381-3p inhibition for mitigating intestinal epithelial damage following I/R injury.

Although Transwell studies and H/R conditions induced on Caco-2 cells provide useful insights into I/R injury *in vitro*, these conventional culture models using transformed cell lines are limited in their ability to recapitulate physiological relevance and the pathophysiology of human ischemia. Tumor-derived Caco-2 cells have been shown to exhibit aberrant responses to stimuli, such as dietary compounds, when compared to primary human-derived epithelial cells.[60] The discovery of conditions that enable primary intestinal stem cells to be expanded in culture enables highly pure populations of ISCs to be studied in H/R conditions.[61, 62] With primary human intestinal epithelial cells cultured in a physiologically relevant intestinal

microenvironment, ischemic processes can be studied at the cellular level without phylogenetic differences.[63]

A microphysiological system (MPS) is an *in vitro* cell culture tissue construct designed to represent a specific biological organ, tissue, or cell microenvironment. For studying intestinal diseases, a MPS would require unique architecture to simulate the intestinal barrier, representative human intestinal cells, and nutrients and gases continuously supplied to promote cell expansion and physiological cell turnover. MPS of hypoxia offer a novel method to investigate intestinal ischemia that allow for strict control of oxygen. With an MPS incorporating primary human intestinal epithelial cells cultured in a physiologically relevant intestinal microenvironment, ischemic processes, specifically pathophysiologic hypoxia, can be studied at the cellular and molecular level without phylogenetic differences. Understanding how hypoxia affects the ISC niche has generally been limited by a) the inability to identify, select, and culture stem cell populations, and b) the inability to expose these populations to hypoxic conditions of varying magnitude and duration without reperfusion. Technologies and methods discussed in subsequent chapters will provide a framework to study oxygen-related processes using human intestinal tissues.

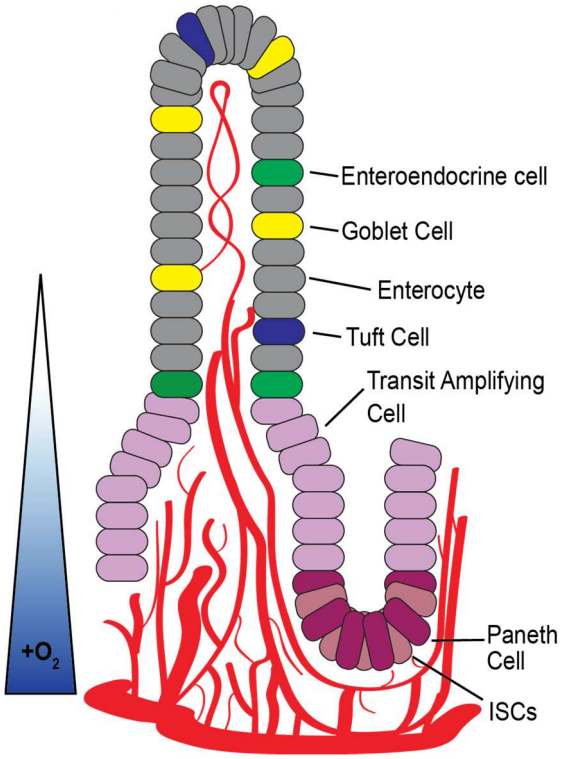

Figure 1.1. Small intestinal crypt-villus unit. Schematic of human *in vivo* crypt-villus unit showing epithelial monolayer containing intestinal stem cells (ISCs), transit amplifying cells, and mature enterocyte lineages. The ISCs are located at the base of the crypt in a steep oxygen (O_2) gradient that stretches from the underlying vascular network to the nearly anoxic villus tip.

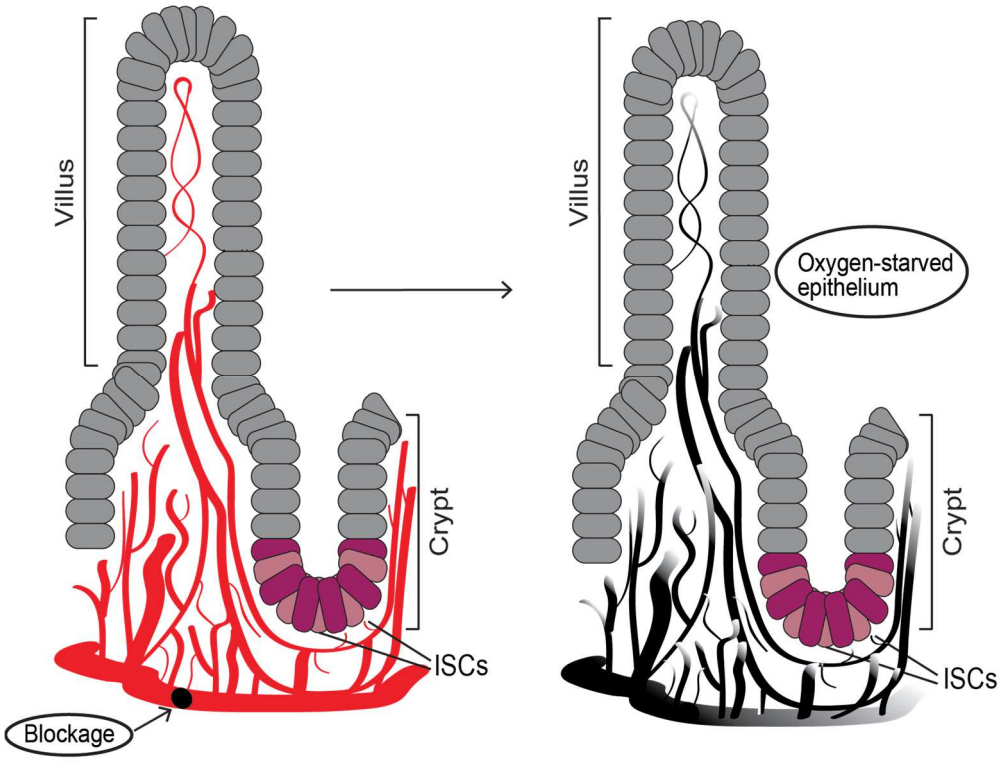

Figure 1.2. Ischemic crypt-villus unit schematic. (Left) Human small intestine crypt-villus unit with healthy epithelium just as an intestinal blockage is trapped inside the underlying vascular network. (Right) Ischemic intestinal tissue with oxygen-starved epithelium as vascular network can no longer sustain blood circulation.

CHAPTER 2: MEASURING AND REGULATING OXYGEN LEVELS IN MICROPHYSIOLOGICAL SYSTEMS (MPS)[1]

2.1. Overview

As microfabrication techniques and tissue engineering methods improve, microphysiological systems (MPS) are being engineered that recapitulate complex physiological and pathophysiological states to supplement and challenge traditional animal models. Although MPS provide unique microenvironments that transcend common 2D cell culture, without proper regulation of oxygen content, MPS often fail to provide the biomimetic environment necessary to activate and investigate fundamental pathways of cellular metabolism and sub-cellular level. Oxygen exists in the human body in various concentrations and partial pressures; moreover, it fluctuates dramatically depending on fasting, exercise, and sleep patterns. Regulating oxygen content inside MPS necessitates a sensitive biological sensor to quantify oxygen content in real-time. Measuring oxygen in a microdevice is a non-trivial requirement for studies focused on understanding how oxygen impacts cellular processes, including angiogenesis and tumorigenesis. Quantifying oxygen inside a microdevice can be achieved *via* an array of technologies, with each method having benefits and limitations in terms of sensitivity, limits of detection, and invasiveness that must be considered and optimized. This article will review oxygen physiology in organ systems and offer comparisons of organ-specific MPS that do and do not consider oxygen microenvironments. Materials used in microphysiological models will

[1] Chapter previously appeared in Analyst. The original citation is as follows: Kristina R. Rivera, Murat A. Yokus, Patrick D. Erb, Vladimir A. Pozdin, Michael A. Daniele. Measuring and regulating oxygen levels in microphysiological systems: Design, material, and sensor considerations. Analyst 144(10), 3190-3215. (2019).

also be analyzed in terms of their ability to control oxygen. Finally, oxygen sensor technologies are critically compared and evaluated for use in MPS.

2.2. Introduction

The terminology for describing oxygen content in human tissue, or even cell culture, requires a fairly complex description and has been thoroughly described previously.[12] Briefly, the partial pressure of oxygen, *i.e.* oxygen tension, is how much pressure oxygen alone would exert if it occupied the volume. In a liquid, such cell culture media, dissolved oxygen is proportional to the partial pressure of oxygen in equilibrium with the liquid at the same temperature and pressure. However, in blood, hemoglobin binds and transports oxygen throughout the body, and the quantity of bound oxygen greatly exceeds the dissolved oxygen content. Both *in vivo* and *in vitro,* cells, tissues, and organs respond to changes in the oxygen tension, *i.e.* proportional to dissolved gases, and total oxygen availability, *i.e.* the combination of dissolved gases and chemically bound gases, in their local microenvironment. For brevity and clarity, we will discuss oxygen content as it relates to the total percentage of oxygen present (<21% O_2) in a local microenvironment for the extent of this review.

In the human body, regions of low oxygen (<5% O_2), such as the brain and muscle, exist in proximity to regions of much higher oxygen (11% O_2), such as the arterial blood and kidneys.[12] While atmospheric oxygen levels typically are near 21% O_2, the oxygen level in inhaled air decreases to approximately 14.5% O_2 by the time it reaches the alveoli, *i.e.* the primary gas exchange site of the lungs.[12, 64] To traverse the alveoli, oxygen binds to hemoglobin in a higher concentration than dissolved O_2, and it is subsequently delivered through the body *via* red blood cells. From the alveoli to capillary beds, oxygen-rich blood moves across into tissues and disseminates through the body along a network of arterioles and arteries. During

aerobic cellular respiration, oxygen molecules are consumed during the production of the necessary energy to perform physiological functions.[65] Many physiological and pathophysiological pathways are initiated by changes in these fundamental processes due to localized deficiency of oxygen, termed "hypoxia," including angiogenesis and tumor metastasis.[66, 67] During severe or chronic hypoxia, most cells of the human body, apart from gut anaerobes, will experience severe stress and become apoptotic and/or necrotic.

Although there can be no quantitative oxygen level standardized to describe either hypoxic or hyperoxic environments in tissues, as they differ widely across tissues, normoxia can be used to describe the physiologic environment of any healthy tissue. The intricate delineations of normoxic oxygen levels and localized oxygen gradients across tissues impact cell proliferation, angiogenesis, migration, and apoptosis as studied across *in vivo* and *in vitro* models.[25, 65, 67-73]

While the normobaric (1 atm) composition of gases in dry air can be estimated at approximately 21% O_2 and 79% N_2, studies of cellular physiology using *in vitro* models are most often performed inside a cell culture incubator under non-ambient conditions. This level of oxygen is much higher than any present in tissue. In a typical cell culture incubator, the controlled supplementation of 5% carbon dioxide (CO_2) and maintained relative humidity of 100% results in a normobaric composition of gases at 37°C, as follows: 70.2% nitrogen gas (N_2), 6.2% water vapor (H_2O_g), 5.0% CO_2, and 18.6% O_2.[74] To achieve reduced oxygen levels, a common practice is to use expensive, bulky hypoxic incubators that only supply one specific level of oxygen by either regulating gas composition by using a pre-defined gas mixture or introducing more N_2 to reduce the partial pressure of O_2. The latter systems are called Tri-Gas incubators, and neither result in the control of microscale oxygen gradients in cell culture

systems during the studies. These all or nothing oxygen environments cannot recapitulate any physiological tissue and represent a gap in past model systems.

Microsystems providing precise control of environmental parameters such as oxygen can help bridge the gap between *in vivo* tissue conditions and *in vitro* models. To alleviate the burden of animal testing and better inform clinical testing, researchers are using microphysiological systems (MPS) that aim to replicate specific micro-anatomies or physiological function by integrating engineered human tissue constructs and microfluidic devices. By replicating specific physiological function at the micro-scale with human cells and tissues, precise questions concerning cell-cell and cell-environment interactions are investigated in a more physiologically-relevant manner.[75, 76]

The exquisite control of both fluid transport and subsequent experimental conditions in MPS provides a novel capability to control oxygen levels across the engineered tissue; nevertheless, measurement and control of oxygen levels in microfluidic devices and MPS has not become a standard practice. MPS are typically gas-permeable microdevices kept inside an incubator operating at hyperoxic oxygen levels (19% O_2), as endogenous oxygen levels experienced by cells within tissues are much less (**Table 2.1**).[12] If a MPS requires an oxygen concentration different from that of an incubator or ambient air, this necessitates a closed off environment and constant reduction or addition of oxygen *via* perfusion of fluid.

Engineering MPS that provide a means to control oxygen content while maintaining viable cell culture requires consideration of materials science, cellular physiology, and mechanical engineering. One scheme to limit oxygen heterogeneity in a microdevice involves using only materials that have minimal oxygen diffusivity, and oxygen is only introduced into the microdevice through oxygenated media or gas.[77] Another method involves using oxygen

permeable materials for the microdevice with isolation inside a hypoxic chamber.[78, 79] Specifics of diffusion-controlled methods for regulating oxygen levels in microfluidics have been described in prior reviews.[80-82]

Herein, we review and assess current methods to measure and regulate oxygen levels in MPS. Specifically, we summarize the physiologically relevant oxygen levels for different tissues and organ systems, and we address the implications of hypoxic and hyperoxic conditions on function and performance of the MPS. With this information in hand, we compare and contrast the available methods for measuring and regulating oxygen levels in microfluidic devices, in the framework of engineering better MPS. This tutorial review will first discuss microdevices and systems used for physiologic studies of oxygen in organs. Next, we explore materials used to build microdevices and *in silico* modeling used to design MPS and predict experimental outcomes. We end with a critical assessment of current methods of measuring oxygen in microdevices. This review is intended to present a general description of design considerations and parameters for measuring and controlling oxygen levels in microphysiological modes; it is not intended to serve as a comprehensive review of this rapidly evolving area of research.

2.3. Microdevice models of physiological organ systems and phenomena

Microdevice models are rapidly transitioning to function as biological analogues for cell studies *in vitro*. MPS accommodate 3D architecture, mechanical stressors, and other appropriate biochemical cues that are present *in vivo* and necessary to study physiological processes.[83-88] Despite advancements in modeling cell mechanics, microdevices often fail to recapitulate the air-liquid interfaces known to influence cells *in vivo*. One of the most important air-liquid interfaces is between oxygen and tissue, as 100 to 200 micrometers (μm) is the upper limit of oxygen diffusion through parenchymal tissue to reach cells before reduced oxygen availability inflicts

cellular damage.[67] Although 200 μm is the common marker of physiologic oxygen diffusion, the true quantity of oxygen available to individual cells depends more on the microenvironment provided by the organ that encompasses them and the density and proximity of surrounding vasculature.

Translating *in vitro* cellular responses into accurate predictions of *in vivo* outcomes requires mimicking the same physiologic oxygen levels found in the native organ. Recent advancements in MPS, both in material fabrication and real-time monitoring, show promise in measuring and controlling oxygen diffusion in cell culture. With each organ presenting unique oxygen environments, it is important to first define the organ-specific normoxic condition for the desired MPS. The normoxic oxygen conditions and relevant cellular composition for the most popular engineered tissue models are illustrated in **Figure 2.1**.

2.3.1. Lung

Oxygen first enters the body *via* inhalation. During respiration, oxygen interacts with multiple layers of body tissue, from mucosal membranes in nasal passages to alveolar ducts in the lung, resulting in gas exchange with the circulatory system. The unique alveolar-capillary interface of the lung is composed of a symbiotic sandwich, composed of epithelial and endothelial cells separated by an interstitial space at which inspired oxygen-rich air enters the body while expired air composed of carbon dioxide exits. Following pathological foreign invasion, endothelial cells facilitate extravasation of inflammatory cells to the upper layer of the epithelium, where inflammatory cells phagocytose foreign invaders before further damage ensues.[89] Diseases that damage the alveolar-capillary interface, such as pulmonary edema, have been studied in MPS of lung tissue.[84] Despite the novelty of studying the alveolar-

capillary interface with a co-culture model system, cell damage in the lung can be caused by factors dependent on gas exchange, including reduced or excess oxygen.[90, 91] Considering the influence of oxygen on the lung, a MPS that includes an air-liquid interface and the appropriate cell types will enable more informative *in vitro* studies.

In 2010, the first MPS was reported as an alveolar-capillary lung mimic that recapitulated organ-level function.[92] Huh *et al.* created this MPS with an alveolar-capillary interface using human pulmonary epithelial and human pulmonary microvascular endothelial cells to study the impact of breathing motions on lung pathophysiology.[84] The lung MPS showed that the cyclic mechanical strain induced to mimic breathing motions could cause increased vascular leakage and was associated with progression of pulmonary edema.[84] More recently, the same co-culture MPS of human lung tissue, with an additional non-small cell lung cancer cell component integrated into the upper epithelium, was used to study drug resistance to cancer therapies and found that non-small cell lung cancer cells respond to tyrosine kinase inhibitor treatment and cyclic mechanical strain (breathing motions) by limiting proliferation and spreading.[93] These findings associated with pulmonary diseases and cancer could be further explored in relation to oxygen availability in a more advanced lung MPS.

A critical component lacking in this lung MPS is controlled oxygen regulation, as oxygen deficiency can be caused by pulmonary diseases, and hypoxia is an important development during cancer progression. Although this lung MPS was seminal in creating a proof-of-concept for using microdevices to study organ-level functions, no iteration of this MPS included oxygen control or measurements of oxygen transports between the alveolar and endothelial cell layers.

Simultaneously while Dr. Huh and other members of the Wyss Institute worked on integrating multiple cell types into a lung MPS, other researcher teams built lung MPS focused

on oxygen regulation. To study how oxygen influences lung epithelial cells, Chen *et al.* seeded carcinomic human alveolar basal epithelial (A549) cells in a microdevice with varied oxygen gradients.[83] Chemical reaction channels on either side of a central cell culture channel provided oxygen scavenging and oxygen generating gas reactions to facilitate the development of an oxygen gradient across the cell culture channel, isolated from the chemical reaction channels by polydimethylsiloxane (PDMS) walls (**Fig. 2.2c**). The oxygen scavenging channel was created using pyrogallol, a powerful organic reducing agent that absorbs oxygen in an alkaline solution, in combination with sodium hydroxide. The oxygen-generating channel was filled with hydrogen peroxide, which decomposed into water and oxygen gas with the addition of sodium hypochlorite. After seeding and overnight attachment, Chen *et al.* exposed A549 cells to hypoxia (≈ 0.5% O_2) for 48 hours and found that a relatively low oxygen tension did not affect A549 cell growth. In a second set of experiments, the authors found inducing a hyperoxic environment (70% O_2) for 6 hours caused A549 cells to peel off the substrate and induced cell death. One major drawback of the microdevice created by Chen *et al.* was the use of potentially cytotoxic chemicals. Furthermore, Chen *et al.* revealed how oxygen influences only one cell type found in lung tissue. Oxygen as it relates to more dynamic cell systems should be explored with a MPS that incorporates an endothelial component, if not more cell types. Furthermore, oxygen permeation through each material in the microdevice could potentially impact cellular response to any drug treatment and should be considered when building a lung MPS.

2.3.2. Kidney

The kidneys filter blood to regulate blood pressure, pH and to maintain a balance of water, electrolytes, and hormones. The kidneys generate energy for tubular reabsorption and

secretion by consuming oxygen to create ATP. The partial pressure of oxygen in the kidney is low, ranging from 10-15 mmHg (approximately 2% oxygen) in the inner medulla and papilla to 40-45 mmHg (6% oxygen) in the renal cortex (**Fig. 2.1**).[94-97] Due to the higher oxygen levels in the renal cortex, cortical cells are the most sensitive kidney cell type to fluctuations in oxygen. In contrast, the inner medullary and papillae cells demonstrate a reduced sensitivity to hypoxic conditions because they generate ATP from glucose *via* anaerobic glycolysis.[98] Oxygen diffusion through the kidney is tightly regulated to ensure proper pH and molecular composition of the blood. A dense network of arteries channel oxygen-rich blood to the kidneys, where blood flows at the highest rate per gram of tissue in the entire body.[99] Reactive oxygen species (ROS) produced during periods of hypoxia have been shown to inhibit kidney function and cause renal damage.[100] Studies of kidney function and ROS have thus far been limited to *in vivo* models, but by developing kidney MPS that include oxygen gradients, the mechanisms of oxygen inhibition can be better understood, especially in oxygen sensitive cortical cells.

ROS are signalling molecules that correlate directly with the local oxygen environment and are released during both hyperoxic and hypoxic events. Kidney cells at the organ level are sensitive to increased ROS production during oxidative stress.[101] To study the modulation of intracellular ROS levels in Madin-Darby canine kidney (MDCK) cells, Lo *et al.* created oxygen gradients in an open-well culture model by diffusing oxygen through PDMS.[88] The open-well culture model was fabricated with a 100 μm-thick PDMS diffusion barrier between a 3 mm PDMS bottom with two gas microchannels and a 5 mm PDMS top with a 1 cm diameter reservoir space for cells and media. By flowing 0% and 100% oxygen through either microchannel, a linear oxygen profile was generated that diffused across the barrier to reach MDCK cells in the reservoir space (**Fig. 2.2a**). MDCK cells exposed to the highest oxygen

concentration in a microdevice produced ROS levels 1.5 times more than the initial ROS reading at time zero. MDCK cells exposed to the lowest oxygen concentration in a microdevice produced ROS levels 1.4 times more than the initial ROS reading at time zero. The 1.5 and 1.4-fold increases in ROS production at hyperoxic and hypoxic extremes, respectively, show that MDCK cells are influenced by oxygen and, furthermore, that a diffusion-based MPS can be used to probe oxygen as a controlled and dose-dependent variable.

An important functional unit of the kidney is a capillary network called the glomerulus. Here, circulating blood is filtered into urine *via* filtration across the capillary wall supported by differentiated epithelial cells called podocytes.[102] A recent publication by Musah *et al.* has defined culture conditions necessary to direct the differentiation of human induced pluripotent stem cells (hiPS) into podocytes.[103] Using the hiPS-cell-derived podocytes and human glomerular endothelial cells seeded on opposite sides of a porous flexible PDMS membrane inside a microfluidic device, the authors of this study showed for the first time that a glomerulus-on-a-chip could functionally mimic differential clearance of large and small molecules, including albumin and inulin, respectively, and recapitulate drug-induced podocyte injury *in vitro*. While the glomerulus-on-a-chip offers a novel platform to study kidney glomerular function, the glomerulus structure is highly influenced by oxygen, as hypoxia-inducible factor (HIF)-1 and HIF-2 regulate podocyte development.[104, 105] Incorporating oxygen regulation into such a platform of the glomerulus could reveal mechanistic insight into factors that influence kidney diseases.

2.3.3. Liver

In the liver, oxygen gradients modulate cellular functions over a median physiological range from 5 to 6% O_2.[12] The drop in oxygen tension from the periportal (11-13%) to centrilobular (4-5%) regions of the liver is considered a primary regulator of liver zonation.[106, 107] Liver zonation, or variant cell function from the portal vein to the central vein, facilitates carbohydrate metabolism and detoxification. Hepatocytes exposed to venous and arterial oxygen levels have shown different cellular responses, including binding activity and gene expression.[106]

To study liver oxygen gradients, Allen *et al.* created a parallel-plate perfusion bioreactor system from a polycarbonate block milled with inlet and outlet ports and two microscope slides. Following perfusion of media equilibrated with either 10% or 21% O_2, subsequent diffusion gradients of oxygen were generated in the bioreactor comprised of a monolayer of primary rat hepatocytes. Controlled oxygen gradients influenced a heterogeneous distribution of protein levels in hepatocytes, including phosphoenolpyruvate carboxykinase (PEPCK, predominately localized upstream) and cytochrome P450 2B (CYP2B, predominately localized downstream).[87] The protein levels correlate with *in vivo* distribution, as PEPCK is predominately located in the higher oxygen periportal region and CYP2B is found in the lower oxygen pericentral region.[108] Despite validation of liver zonal induction and oxygen gradient generation (with miniature Clark-type electrodes), the authors of this study found that the bioreactor was limited to short-term experimentation (3 to 4 days), as primary hepatocytes in their monolayer culture quickly lost their differentiation function.

To better mimic the oxygen gradient in the native liver microenvironment, Bavli *et al.* expanded upon the work of Allen *et al.* to create a liver-on-chip that could maintain 3D

aggregates of immortalized human hepatocellular carcinoma cells (HepG2/C3A) for 28 days. In the previous parallel-plate perfusion bioreactor system, cells were organized in a single 2D monolayer. In contrast, the microdevice created by Bavli *et al.* included 9 individual microwells for the 3D HepG2/C3A aggregates. The 3D HepG2/C3A aggregates cultured as spheroids inside microwells introduced complexity to this system, as oxygen was depleted in the center of the spheroid. By incorporating tissue-embedded phosphorescent microprobes and a computer-controlled microfluidic switchboard, oxygen consumption and glucose and lactate levels were monitored in real time.[109] This platform also included continuous controlled perfusion of cell culture medium. The sensor-integrated platform tracked in real-time the minute shifts from oxidative phosphorylation to glycolysis or glutaminolysis, signalling mitochondrial dysfunction and chemical toxicity before any effects on cell or tissue viability could be observed.

Another example of a real-time MPS that established an oxygen gradient was created by Domansky *et al.*[110] The authors designed a perfused multiwell with isolated bioreactors, each containing a reactor well, a reservoir well, and an integrated micropump. The reactor well had a collagen-coated scaffold with a diameter of 14.9 mm for cells to self-assemble into an array of ~0.2 mm 3D tissue structures, while the reservoir well contained continuously circulating culture medium. With a co-culture of half murine hepatocytes and half murine liver sinusoidal endothelial cells seeded onto the scaffold in the reactor well, cells consuming oxygen created an oxygen gradient (**Fig. 2.2e**). The authors found that a flow rate of 0.25 mL min^{-1} created a tissue outlet oxygen concentration of approximately 50 μM (~5% O_2). An oxygen concentration of approximately 50 μM provided a reasonable approximation of physiological oxygen gradients, as reported human *in vivo* perivenous (sinusoidal exit) region dissolved free oxygen concentrations range from 42 to 49 μM.[111] The oxygen consumption rates of hepatocytes in

the bioreactor were comparable to rates for perfused rat livers (2.6 versus 1.8 μmol·hour^{-1}·mg protein^{-1}).

The microreactor system used in the study by Domansky *et al.* has been further advanced with addition of primary human liver cells and commercialized by CN Bio Innovations (Hertfordshire, UK), with multiple researchers using the LiverChip to analyze drug metabolism and drug-drug interactions.[112-114] The LiverChip platform includes a pneumatically-driven on-board microfluidic pumping system, distributing positive and negative air pressure to individual valves and pump chambers, to perfuse each scaffold with culture medium and control oxygenation.[115] Each reactor well and reservoir well contains a filter with 5 μm pores and a filter support to prevent cells from entering the valves and pumps beneath them. The open well format provides for quick cell seeding and media exchange with pipettes. Overall, the LiverChip is a promising example of a commercialized MPS that considers oxygen regulation for drug studies. The LiverChip platform, containing both primary rat hepatocytes and primary rat sinusoidal endothelial cells, could also be used to investigate the impact of oxygen on liver zonation. Incorporation of additional cells, including Kupffer cells that line the sinusoids and are responsible for phagocytizing bacteria and foreign invaders and stellate cells that are activated during liver injury, would enable for more complex studies of liver function. These additional cells have recently been incorporated in a liver MPS, but this platform fails to include primary human cells or oxygen regulation.[116]

2.3.4. Vasculature and Skin

Integrated throughout all tissues is a vascular network critical for supplying nutrients and removing waste, including oxygen and carbon dioxide transport. Oxygen exchange is facilitated

largely by blood flow from the macroscale aortic valve of the heart down to the microscale capillary beds within tissue. Many vasculature-like structures have been created using microdevice technologies. In most examples, microscale vasculature is formed using hydrogels seeded with stem cells or mature endothelial cells and growth factors to encourage angiogenesis and induce vascularization.[117-120] With a random and spontaneous formation of capillary networks, perfusion of media is impossible and the low density of mature capillary networks limits diffusion of oxygen. Another option for creating vasculature inside a microdevice involves creating a synthetic vessel system composed of a combination of biological and synthetic materials.[121-123] The synthetic vessel system provides for perfusion and acts as a nutrient supply pathway.

Although all living tissues require blood supply via a vascular network, most MPS of various organs were first developed without consideration for a vasculature, as the focus was to ensure the key cells relevant to a specific organ were recapitulating *in vivo* functionality. One organ in which vasculature was not overlooked initially in MPS fabrication was the skin, as oxygen concentration differs significantly across specific layers of the epithelium. Oxygen increases significantly from 1% O_2 at the outer epidermis layer of human skin to 3% O_2 at the dermal papillae and 5% O_2 oxygen at the sub-papillary plexus.[12] Many MPS have been made to include a vascular component (i.e. endothelial cells) in a skin equivalent, but few have realized perfusable networks.[124-127]

Recently, Mori *et al.* built a skin-on-chip with a perfusable network of channels coated with human umbilical vein endothelial cells (HUVECs).[123] The channels were created inside a culture device with 0.52 mm diameter nylon wires strung across connectors of the device. Collagen solution containing normal human dermal fibroblasts was polymerized inside the

culture device and then removal of the nylon wires left behind hollow channels, where HUVECs were seeded to form vascular channels. A dermal skin layer seeded with normal human epidermal keratinocytes (NHEKs) was added on top of the collagen hydrogel to complete the fabrication of the skin-equivalent with vascular channels. Characterizing the skin MPS, the authors found perfused vascular channels remained open while non-perfused channels nearly closed. HUVECs and NHEKs were also influenced by nutrient supply, as the perfused skin-equivalent had 3-fold higher average cell density than the non-perfused skin-equivalent. Interestingly, cell density was highest closest to the nutrient supply, a depth range of 0 to 100 μm from the perfused skin-equivalent, and cell density was maintained on the order of 10^8 cells·mL^{-1} around the vascular channels. These results are promising support for using perfusion systems to fabricate thick tissues with proper nutrient and oxygen supply. Although levels of oxygen were not measured in this skin-on-chip, measuring and controlling oxygen inside the perfusion system would enable more interesting findings in skin and vascular tissue engineering research.

2.3.5. Heart

The heart is the only organ relegated to dealing with the burden of handling deoxygenated blood from the body, pumping it to the lungs for oxygen restoration, and delivering oxygenated blood to the rest of the body. Blood flow begins when deoxygenated blood enters the vena cava and fills the right atrium, causing the right atrium to contract. Contraction leads blood to the right ventricle, causing the ventricle to contract, the tricuspid valve to close, and blood to flow through the pulmonary artery to the lungs. The deoxygenated blood becomes oxygenated as it flows through the alveoli and out through the pulmonary vein (**Fig. 2.1**). From the pulmonary vein, oxygenated blood enters the left atrium. The left atrium

contracts, as the mitral valve closes, and blood fills the left ventricle. After filling the left ventricle, the oxygenated blood enters the opened aortic valve and flows through the aorta to the rest of the body. The muscles of the heart also require oxygen to function; therefore, coronary arteries are necessary to pump oxygen-rich blood throughout the heart itself. The meticulous path of oxygenated blood flow throughout the body illuminates why the heart is a vital component to consider when investigating oxygen physiology. If there are any problems with the heart, such as arrhythmia, palpitations, or angina, the rest of the body can immediately be subject to oxygen deficiency. To study oxygen in the heart, cardiac muscle cells or cardiomyocytes have been cultured in various oxygen environments in 2D and 3D.[85, 128-131]

The impact of periods of low or no blood flow and subsequent low oxygen availability (ischemia) on the heart have been studied using primary porcine cardiomyocytes in a low-shear MPS of ischemia-reperfusion injury.[85] Using PDMS bonded to a glass slide to create 2 channels, one for culturing primary porcine cardiomyocytes and one for an oxygen-sensitive dye, a microdevice was created. The cell culture channel was coated with Matrigel, loaded with cardiomyocytes, and placed inside an incubator for cells to attach before inducing an ischemic event. After 2 hours, the microdevice was placed inside a polycarbonate box on a microscope stage. The box had an opening on the bottom for cells to be imaged and inlet and outlet ports on the top for nitrogen flow to displace oxygen and induce ischemia within 30 minutes. Reperfusion was induced *via* rapid restoration of oxygen to the microdevice. The authors of this study found that during a 3-hour period cardiomyocytes exhibited 0% apoptosis while in "normoxic" conditions. By contrast, the number of cardiomyocytes that underwent apoptosis increased from 3% to 22% O_2 from hour 2 to hour 3 in the ischemic condition. Further evidence of ischemic injury came from morphological assessment of cardiomyocytes. After 1 hour of ischemia,

cardiomyocytes retracted from the Matrigel-coated surface and displayed spheroid morphologies, indicative of cell stress. Overall, this microdevice with controlled oxygen levels proved useful for revealing cellular responses to controlled ischemic events that would not have been possible in typical cell culture systems. With the perfusable polycarbonate box, oxygen content on the microdevice could be rapidly and precisely controlled, to simulate ischemic events of varying durations, from acute to long-term, to be further investigated using cardiomyocytes harvested from a single animal. The microdevice could be translated to clinical outcomes of ischemia/reperfusion injury by incorporating cardiomyocytes derived from patient-specific human induced pluripotent stem cells (hiPSCs).

Another MPS created to recapitulate myocardial function was designed to include a co-culture of hiPSC derived cardiomyocytes and hiPSC-derived endothelial cells.[132] Photolithography and microfabrication techniques were used to form a PDMS microdevice with 2 outer channels for endothelial cells and a central channel for cardiomyocytes encapsulated in a photocrosslinkable hydrogel of gelatin methacrylamide (GelMA). The outer channels served as 1.1 mm wide microvasculature channels separated from the central channel by PDMS posts and supplied nutrients and oxygen to the central channel through media flow. The entire device was fabricated with PDMS and possessed a shallow depth of 160 μm, so diffusion through the top and side walls could deliver oxygen to the cell channels. Using this myocardium-on-chip, Ellis *et al.* revealed that cardiomyocytes and endothelial cells derived from hiPSCs from a single individual could be functionalized inside a microfluidic device for 7 days without losing phenotypic lineage commitments. Endothelial cells formed tube-like networks that infiltrated into the cardiac muscle channel, closely mimicking the microvasculature of human myocardium. Future studies that include longer culture and additional growth factors could reveal functional

networks that transport cytokines from endothelial channels to cardiomyocytes. The myocardium-on-chip could also be enhanced to measure and regulate oxygen diffusion, enabling more in-depth studies of ischemia on cardiac and endothelial cells before and after drug treatment.

Both cardiac MPS described above aim to recapitulate cardiac functions through control of fluid flow and cellular response. To achieve complete cardiac function on the microscale, human cardiomyocytes and endothelial cells must be organized in relevant microarchitecture, form capillary-like networks for fluid exchange, exhibit synchronized beating frequency, and proper stimulation response. Studies of oxygen exchange in a cardiac MPS are only possible after such characterization is achieved in a reproducible, long-term manner. With realized capillary flow and proper diffusion of gas, oxygen can become a single experimental parameter that can be easily manipulated in a cardiac MPS to reveal new relationships and responses on cell-specific functions in the heart.

2.3.6. Brain

With the highest metabolic activity per unit weight of any organ, the brain consumes 20-25% of the oxygen in the entire body.[133, 134] Decreased oxygen concentration in brain tissue can occur with increased depth, but normal brain tissue functions with an oxygen concentration of approximately 4.6% O_2.[12] Although the brain demands high oxygen, its inability to store metabolic products makes it critically dependent on oxygen delivery. Any slight decrease in oxygen can lead to severe brain damage in minutes. Cell-specific responses to post-ischemic brain damage include degradation of the extracellular matrix and astrocyte and endothelial detachment from basal lamina, causing increased brain microvascular permeability and glial and

endothelial apoptosis.[135, 136] A variety of brain MPS have been created to investigate cell-specific responses, but controlled delivery of oxygen in these models is still in its infancy.

One important example of controlled delivery of oxygen in a microdevice was created to study hypoxia in 350 μm thick murine hippocampal brain slices.[137] Mauleon *et al.* altered a standard open bath perfusion chamber by adding a gas inlet and outlet and added this chamber to the top of a 100 μm thick PDMS membrane and 200 μm thick PDMS microfluidic channel atop a glass slide. The permeable PDMS membrane allowed oxygen diffusion from the gas channel to brain slice. Overall, by introducing fluid flow above and below the brain slice, the microdevice achieved more stable and uniform oxygen levels throughout the brain slice than had been previously reported with a perfusion chamber alone. The authors could induce physiologically relevant hypoxic insults at controllable rates and at defined locations on the brain slice. This technology was used to study calcium indicator dyes in brain slices from multiple species, including naked mole rats and mice, and multiple age groups, including postnatal (12 to 30 days old) and adult mice.[138, 139]

A more advanced brain MPS developed by Johnson *et al.* involved 3D printing complex geometry into microfluidic channels and incorporating multiple cells types, including primary rat embryonic sensory and hippocampal neurons.[140] The platform was manufactured using micro-extrusion 3D printing strategies with cell suspensions fed into extruder tips to create 350 μm wide microchannels and 3 adjacent 6 mm chambers directly on protein-coated petri dishes. The 3 adjacent chambers created a compartmentalized neural system with primary rat neurons and axons in the first chamber, self-assembled Schwann cells (S16, CRL-2941, ATCC) in the second chamber, and porcine kidney epithelial cells in the third chamber. The highly functional neural system provided a route for axon termini from the first chamber to interact with both cell types in

the adjacent chambers to create aligned axonal networks. Recreating the glial cell-axon interface inside a biomimetic system could be further expanded upon by introducing relevant fluid flow and oxygen exchange in 3D microchannel networks, as considered in the previous Mauleon *et al.* brain slice platform. Further examination of neural activity in an *in vitro* model of the brain requires more control of relevant brain physiology, including oxygen distribution.

2.3.7. Tumor

Oxygen also plays a significant role in tumor development and metastasis. As a tumor grows, the distance from the tumor center to the surrounding vasculature increases, leading to the generation of a hypoxic core. Tumor cells farther away from native blood vessels receive less oxygen and have limited mass transfer. The tumor stroma develops an altered extracellular matrix with more fibroblasts that synthesize growth factors, chemokines, and adhesion molecules.[141] Tumor cells respond to hypoxia by secreting chemokines that induce neoangiogenesis, or new vascular formation. As the tumor becomes denser and cells form close contacts, therapeutic drugs meant to deliver lethal concentrations of a cytotoxic agent are limited to outer boundaries and heterogonous distribution, thereby targeting only a fraction of tumor cells. Thus, a hypoxic environment can lead to drug resistance and tumor progression.[66, 142] Understanding how hypoxia-induced changes create tumor masses that are more resistant toward chemotherapy and radiotherapy could significantly improve cancer therapies.

Microdevices with controlled oxygen mechanisms provide better experimental conditions for studies of hypoxia-induced changes in cancer cells and the tumor microenvironment.[66, 143-146] One method for creating a hypoxic environment is to place a microdevice in a small metal hypoxic chamber and displace oxygen via nitrogen flow in the chamber.[66] Khanal et al.

showed that even with constant flow of oxygenated medium, a PDMS microdevice inside a hypoxic chamber could be deoxygenated to approximately 1% oxygen within five minutes. The PDMS microdevice then served as an oxygen sink, quickly deoxygenating media perfused through the microdevice. By displacing oxygen rapidly to establish a hypoxic environment, shorter pre-conditioning of cells was necessary to evaluate drug response. Preconditioning human prostate cancer cells to hypoxia lead to significantly different drug responses, including resistance to the cancer drug staurosporine and decreased apoptosis. By quickly preconditioning cells to hypoxic environments using microdevices, more research into drug resistance mechanisms could lead to improved anti-cancer compounds that are more effective against hypoxic tumor cells.

Recently, methods for generating intratumoral hypoxic microenvironments have focused on regulating oxygen diffusion through hydrogels and adjusting cellular oxygen consumption by altering cell-seeding density.[146, 147] In one example, an oxygen gradient was made in a fibrous collagen hydrogel by changing the thickness of the hydrogel. The fibrous collagen hydrogel created had an oxygen gradient increasing from approximately 1% oxygen at the bottom to 21% oxygen at the top.[146] Collagen was chosen as the hydrogel matrix because it has a fibrous structure that can be adjusted and it has a relatively low oxygen diffusion coefficient.[148] By adjusting the pre-incubation period of collagen gel solution (at 4C), but keeping the collagen concentration constant, collagen fibers aggregated without cross-linking to form either high fiber density (2-hour pre-incubation) or low fiber density (30 minute pre-incubation) collagen hydrogels. After fabricating low and high fiber density gels of heights 3 mm tall (gradient from 1 to 15% O_2) and 1.5 mm tall (gradient from 10 to 15% O_2), murine undifferentiated pleomorphic sarcoma cells encapsulated in high fiber density hypoxic gels were

reported to migrated faster and degraded the matrix more rapidly than the low fiber density hypoxic gels (**Fig. 2.2d**). The increased speed of sarcoma cell motility suggests that fiber density, hydrogel size, and stress relaxation of hydrogels cause different cellular responses under hypoxic gradients. These findings are relevant to tumor progression *in vivo* as the tumor microenvironment changes from a lower to a higher density as tumorigenesis progresses. Using oxygen concentration to define the density of a tumor could help determine potential treatment options as increased fiber density may require higher doses of chemotherapy delivered to specific regions of the tumor.

2.3.8. Intestine

Hypoxic and near anoxic environments are also found in normal physiologic regions. One example of a normal or physiologic hypoxic microenvironment *in vivo* is the intestinal lumen, where intestinal epithelial cells and anaerobic microbes co-exist within a steep oxygen gradient. The steep oxygen gradient is formed through layers of tissue, from the oxygenated, highly vascularized lamina propria and submucosa (8% O_2) to the tip of the villi (1.5% O_2).[11] At the tip of the lumen, facultative and anaerobic microbes flourish in a near anoxic environment (<1% O_2).[149] Interestingly, the low oxygen environment necessary to sustain a diverse and enormous population of facultative and anaerobic bacteria, approximately 10^{14} bacteria strong, fluctuates dramatically following digestion and metabolic demand. Within seconds of epithelial contact with nutrients, intestinal blood flow and oxygen extraction locally increase and then, following absorptive hyperemia (accumulation of blood in the underlying vessels), oxygen tension within the villus decreases from approximately 2% to <1% O_2 as the microbial zone expands to break down nutrients.[150] In the rest of the gastrointestinal tract, hypoxia is

associated with poor function, as patients with active inflammatory diseases are often plagued by loss of epithelial barrier function and development of lesions.[151] Any damage to the epithelial barrier increases the possibility of bacteria escaping the lumen and infiltrating the body. This devastating phenotype of a complicated inflammatory pathway requires inflammatory disease studies that include controlled oxygen environments. Typically, *in vitro* cultures of intestinal epithelial cells only include constant oxygen concentrations, in contrast to the cyclic and gradated intestinal oxygen levels.

To study intestinal oxygen, MPS have been designed where precise manipulation of flow and diffusion support co-culture of anaerobic bacteria and mammalian cells.[152-155] One version of a co-culture intestinal MPS was created by Kim *et al.* using a PDMS microdevice with top and bottom cell culture microchannels separated by a porous PDMS membrane.[153] On the left and right sides of the cell culture microchannels, hollow vacuum chambers facilitated peristalsis-like cyclic mechanical strain to promote epithelial cell differentiation and villus formation. The microdevice included human epithelial colorectal cells (Caco-2 cell line) that spontaneously formed intestinal villi on the top microchannel after approximately 100 hours of medium flow and cyclic mechanical stretching. On the bottom microchannel, human capillary endothelial cells were cultured to form a monolayer on the opposite side of the porous PDMS membrane. Probiotic gut microbes *Lactobacillus rhamnosus GG* (LGG) were added to the top cell culture of Caco-2 cells and grew in direct contact with the epithelium for more than two weeks. Kim *et al.* found that microbial cells predominately colonized the intervillus spaces, despite uniform seeding, and that confined intervillus spaces within the densely packed microchannel potentially caused facultative microbes to rapidly consume oxygen, thereby producing a local anoxic microenvironment to support anaerobic microbial growth. Increased

microbial cell colonization in the intervillus spaces could be confirmed by measurements of oxygen in the gut MPS. Further investigation into the oxygen consumption facilitated within the cell culture microchannels would support the use of oxygen controllable systems to study host-microbe interactions in the gut.

Another example of a colon MPS with a co-culture of Caco-2 cells and LGG was fabricated using a polycarbonate (PC) outer enclosure with sandwich silicone rubber gaskets and semi-permeable PC membranes.[154] The device included three microchambers, the bottom for medium perfusion, the middle for the Caco-2 cell chamber, and the top chamber for LGG microbial cells. Separating each chamber were either micro- or nanoporous membranes to permit exchange of biomolecular and oxygen gradients. The microporous membrane (pore diameter, 1 μm) separated the perfusion chamber from the epithelial cell chamber to allow for perfusion-dominant exchange, while the nanoporous membrane (pore diameter, 50 nm) separated the epithelial cell chamber from the microbial chamber to prevent microorganism infiltration. Both normoxic and anoxic culture media were perfused to the respective microchamber, with the concentration of oxygen in the anoxic culture media maintained at 0.1% by bubbling with nitrogen gas. Shah *et al.* used this microdevice system to show that when co-cultured with LGG, Caco-2 cells display transcriptional responses in agreement with host-microbe *in vivo* interactions.

Despite the novelty of co-culture systems, the intestinal MPS described above are limited by the tumorigenic cell line used to generate Caco-2 cells because Caco-2 cells differ from normal human enterocytes in regards to contact inhibition, as they possess tighter cellular junctions than normal epithelial cells.[156] A co-culture model of human-microbial crosstalk with oxygen control could be further enhanced with more representative cell types found in the

human small intestine or colon, such as primary intestinal epithelial cells and multiple anaerobic and aerobic bacteria that occupy the native human lumen.

2.4. Design considerations for engineering physiologically-relevant oxygen gradients in MPS

2.4.1. Materials

To engineer a MPS with an oxygen gradient or hypoxic region, a material impermeable to oxygen must be used and any oxygen introduced into the MPS must be removed quickly. Cellular respiration, deoxygenation and reoxygenation of media, and removal of waste will alter oxygen levels, and the material must allow for rapid adjustment and reestablishment of the desired concentration of oxygen. To measure and control oxygen, the first parameter to optimize is the potential oxygen exchange through each material. Some key materials used for cell culture and microdevice fabrication include polydimethylsiloxane (PDMS), polystyrene (PS), polycarbonate (PC), poly(chloro-p-xylyene) (Parylene-C) and polymethyl methacrylate (PMMA). PDMS and PMMA are chosen for easy and repeatable fabrication that can provide microscale architecture needed for cell attachment and proliferation. Due to limited oxygen diffusivity, PC and Parylene-C provide microenvironments with controlled gas exchange and limited oxygen contamination from the surrounding environment. Collecting data from a MPS should be considered when choosing a material, as studies focused only on endpoint readouts cannot readily benefit from the real-time monitoring offered by optically transparent materials. Deciding on a material to fabricate a MPS involves consideration of critical characteristics, including oxygen diffusivity (**Table 2.2**) and workability, as explored for each material below.

Polydimethylsiloxane (PDMS). Many MPS are constructed from the elastomer, PDMS, in part due to ease of fabrication and optical transparency, but also due to its high gas

permeability, which is often desired to transport oxygen from the incubator into the cell culture device.[157] PDMS allows for microscale features to be designed and molded for prototyping *via* soft lithography.[158] With control of part thickness, semi-permeable membranes of PDMS can facilitate transport of gases through walls or layers. Despite its ubiquity in microfabrication, PDMS may not be the best material for microdevice applications focused on controlling oxygen because oxygen possesses a high diffusivity (3.4×10^{-5} $cm^2 \cdot s^{-1}$) and solubility in PDMS compared to other common materials and thick PDMS is required for mechanical strength (Table 2).[159] PDMS can also negatively impact cell studies because it can absorb small hydrophobic molecules, such as drugs, and leaches un-crosslinked oligomers into solution.[158, 160, 161] The absorption of hydrophobic molecules is especially an issue for MPS that intend to test drugs or rely on perfusion of media; therefore, the use of PDMS may contribute confounding variables in such studies. PDMS is also expensive and could be replaced with polymers more resistant to small molecule absorption, such as polyurethane or polycarbonate.[162] PDMS can be chemically modified using oxygen plasma treatment to enhance hydrophilicity and allow for better cell attachment and viability.[163] PDMS microdevices can also be coated with ECM-components or integrated with hydrogels, but these additions may negatively impact the optical transparency of the microdevice surface, sacrificing visibility needed for monitoring cell morphology *via* real-time microscopy.

Polystyrene (PS) is the most popular cell culture material used to manufacture cell culture flasks and plates. Its optical clarity, ease of molding, and stability during sterilization *via* irradiation make it a gold-standard material for mass production of cell culture platforms. PS has a relatively low oxygen diffusion coefficient (2.3×10^{-7} $cm^2 \cdot s^{-1}$) compared to other plastics and polymers, therefore, it can be used for microdevices which aim to control oxygen permeation

(**Table 2.2**).[164] PS can create 3D oxygen gradients, as it is a semi-impermeable barrier on the sides and bottom of any culture dish and allows for oxygen to only traverse the space between, which can be filled with hydrogel for a cell system.[146] One disadvantage of PS for cell culture is its hydrophobic surface, which limits cell adhesion. Most PS plates are treated using either gas-plasma under vacuum or corona discharge under atmospheric conditions to be more hydrophilic.[165, 166] If an MPS is to be fabricated with PS walls or layers and requires cell attachment, then the surface will require chemical modification. PS is also more difficult and expensive to prototype on the microscale, as it requires expertise in micromilling and thermal bonding, as compared to the soft-lithography techniques used for PDMS prototypes.[167]

Polycarbonate (PC) can be added to microdevices to control oxygen.[85, 87, 154] PC has a very low oxygen diffusion coefficient (8.0×10^{-8} $cm^2 \cdot s^{-1}$) compared to other microdevice materials and PC films have been used to surround PDMS devices and prevent oxygen diffusion from an incubator into a microdevice.[144, 168] PC is also easy to machine and can be sterilized *via* autoclave. In one study, a PDMS device was created with a PC film layered above microchannels composed of a central gel region with media channels and gas channels flanking each side (Figure 2).[144] Normoxia was created using a humidified gas mixture of 21% O_2, 5% CO_2, and 74% N_2, each supplied to the microdevice channels at a flow rate of 18 ml min^{-1}, corresponding to fluid flow dominated by advection. A 10 wt.% sodium sulfite (Na_2SO_3) solution humidified a 0% O_2 gas mixture to remove dissolved oxygen and generate uniform hypoxia in the microdevice. Next, one gas channel was switched from 0% to 21% O_2 to generate an oxygen gradient. The authors of this study found that with the PC film approximately 2% O_2 could be achieved within a microdevice, whereas without the PC film the lowest oxygen tension achieved was 6.5% O_2. Once validated, the microdevice was used in studies comparing how

normoxic and hypoxic environments affect human breast cancer cell migration. Using 3D confocal imaging in real-time, the authors reported that hypoxic conditions promoted directional cancer cell migration and increased migration speed as compared to normoxic conditions.

Poly(chloro-p-xylyene) (Parylene-C) has been used to coat PDMS microdevices and prevent oxygen contamination from ambient air. Using a film as thin as 2.5 μm, a Parylene-C coating has been shown to inhibit oxygen diffusion through a PDMS membrane.[123, 157, 169, 170] In experiments designed to compare the diffusion of oxygen through Parylene-C, PDMS microchannels were fabricated and bonded to PDMS membranes with and without Parylene coatings.[169] Using fluorescent oxygen sensors placed directly below the membranes, researchers found that an infusion of 0% oxygen gas (5% carbon dioxide and balanced nitrogen) through the PDMS gas channel caused an uncoated PDMS membrane to equilibrate to 0% O_2 within a minute. In contrast, a Parylene-coated PDMS membrane sustained an oxygen concentration of approximately 21% O_2, remaining at the same concentration of oxygen as present in the surrounding environment despite the flow of anoxic gas on the opposite side of the coated membrane.[169] Similarly, when challenged with an infusion of pure O_2, the uncoated PDMS membrane reached 100% O_2 within a minute, whereas the Parylene-coated PDMS membrane remained at approximately 21% O_2. These results demonstrated that Parylene-C is a useful coating to add on to any microdevice material to prevent oxygen contamination from ambient air when coated on the outer walls of the microdevice or between different layers when coated on partitioned membranes.

One major disadvantage to coating any surface with Parylene-C is its hydrophobicity, which can lead to extremely low cell adhesion. O_2 plasma treatment can be used to alter a Parylene-coated surface to make it more amenable to cell culture as the treatment alters the

surface from hydrophobic to hydrophilic.[171] O_2 plasma treatment has been shown to increase the adhesion of collagen and cells on Parylene by permanent addition of hydrophilic groups, such as hydroxyl and carboxyl groups that increase adsorption of adhering molecules of the culturing medium.[172, 173] Comparing a plasma-treated Parylene-C surface to a non-treated Parylene-C surface, Hoshino *et al.* found that plasma-treatment increased neural cell adhesiveness more than twenty times.[172] These findings significantly support the use of O_2 plasma treatment to increase cell attachment, because neuronal cells typically have worse cell adhesiveness than any previously tested cells. Another option when using Parylene-C is to only coat the walls and outside of a microdevice, thereby allowing for cells to adhere to an uncoated surface or membrane inside the device and still limiting outside environmental oxygen contamination.[169] Coating a microdevice with Parylene-C can be performed using a commercial chemical deposition system to complete vacuum vapor deposition polymerization.

Polymethyl methacrylate (PMMA) has a very low oxygen permeability (2.7×10^{-8} $cm^2 \cdot s^{-1}$) compared to other common microdevice materials.[174] PMMA, also known as acrylic, is biocompatible and amenable to micromachining, therefore it has been used to create replicate microdevices.[91, 109, 175-178] PMMA is often used as a support layer on the top and/or bottom of microdevices to prevent environmental oxygen contamination. PMMA is mechanically and thermally robust enough to support multiple microfabrication techniques including, laser cutting/engraving, milling, hot embossing, and injection molding, while maintaining high-resolution microscale geometries.[179-182] PMMA is transparent to visible and near infrared (NIR) light, allowing for *in situ* imaging and fluorescence-based characterization.[183] PMMA can be fabricated into porous microfluidic films to transform the material from possessing a very low permeability to one that possess a high permeability

comparable to PDMS.[184] Gas diffusion is possible across the PMMA porous film, which can be used to oxygenate media on the opposing side of the film without disturbing cell aggregates or monolayers beneath the film. With PMMA porous films, multiple layers in a microdevice can be easily stacked, allowing for different functions and morphology across a single microdevice. For MPS, a PMMA porous film could facilitate oxygen diffusion through specific layers and offers an alternative material to bypass the potential leaching of oligomers into solution observed in PDMS.

2.4.2. Methods of controlling oxygen content and distribution in MPS

Hydrogels form 3D extracellular matrix (ECM)-like environments for cells to align within, on top of, and alongside which are much more like native tissue in the body than standard flat tissue culture plates. Hydrogels can also be modifiable, as cells secrete their own ECM proteins and remake a hydrogel matrix. Cellular hydrogels can be made of many biological materials such as agarose, collagen, gelatin, and Matrigel and supplemented with additional ECM-like components such as RGD-binding motifs.[144, 147, 148, 185, 186] One example of an oxygen gradient in a microdevice created with a hydrogel was made with agarose gel and PDMS.[186] The microdevice was made with two perfused microchannels, the bottom channel filled with 0% O_2 gas (in balanced nitrogen and 5% CO_2) and the top channel filled with either 5% or 21% O_2 gas. With continuous perfusion of oxygen, a steady-state oxygen gradient was formed in an agarose hydrogel sandwiched between the two microchannels. A platinum-based fluorescent oxygen sensor was used to confirm the presence of an oxygen gradient across the agarose gel and will be described in more detail below. Generating an oxygen gradient across a hydrogel can be easily realized inside MPS designed with inlet and outlet ports for gas flow. One

consideration when deoxygenated via gas diffusion is that the defined oxygen levels at each step across the oxygen boundaries cannot be measured without multiple oxygen sensors measuring in parallel along the length of the hydrogel.

Transwells can be used for hypoxic studies with an additional insert. A transwell, or Boyden chamber, is a porous membrane-based platform polarized for migration and invasion cell studies. A transwell is composed of a chamber insert with a Polyethylene terephthalate (PET) porous membrane placed inside a PS tissue culture well plate well. Typically, two different cell types are cultured inside the transwell on opposing sides of the porous membrane, facilitating cellular interaction. Using microdevice fabrication techniques, a hypoxic chamber has been made inside a transwell with a Parylene-coated PDMS microfluidic network for gas infusion, as shown in **Figure 2.2f**.[169] By enclosing the entire well within the Parylene-coated insert, a hypoxic environment in the device was achieved, equilibrating to 1% O_2 in just 20 minutes.[169]

Although transwell inserts offer a simple method to studying cell-cell interactions, generating a controlled oxygen environment in a transwell by adding more components is more difficult than creating a controlled oxygen environment with a microdevice alone. Transwells are limited to studies of only two cell types, whereas microdevices have been designed to include as many as four cell types thus far.[116] Microdevices offer higher sensitivity and control over diffusion of soluble factors than transwell derivatives because microdevices can be fabricated with channels and compartments to provide greater spatial organization.[57] Some initial co-culture studies of oxygen can be performed using modified transwell inserts, but the number of cells and medium required will remain limiting factors in Transwells that are typically in volumes of milliliters, whereas microdevices offer an alternative approach to investigate oxygen in cell culture systems while minimizing resources.

Microdevices can rely on rapid diffusion of small molecules to generate an oxygen gradient.[87, 109, 146, 147, 154] Diffusion through liquid medium can be estimated inside a microdevice, assuming steady-state transport in a uniform flow field. With lateral diffusion in a given direction, oxygen concentration at any location is dependent on the channel height and length, as well as oxygen diffusivity and the Peclet number. The Peclet number is the ratio of advection to diffusion, calculated using the average flow velocity in a channel, the width of the channel, and coefficient of diffusion.[87] A Peclet number of 100 characterizes transport of fluid flow dominated by advection. As flow velocity decreases, the Peclet number decreases and diffusive transport dominates convective transport. Dominately diffusive transport at lower flow rates allows for oxygen gradients to form along the length of a microdevice, as shown by Allen *et al.* in 2003.[87] By perfusing media across the length of a 28 mm x 55 mm x 100 μm channel at a rate of 0.35 $mL \cdot min^{-1}$ for 24 hours, Allen *et al.* created a MPS of the liver with appropriate zonation of oxygen, from 21% O_2 at the inlet to <1.5% O_2 at the oulet. Developing an oxygen gradient across a channel with simple Cartesian geometry provides a uniform flow field, but deleterious fluid shear and cell seeding conditions can lead to non-uniformity in the flow field and must be considered in any model predictions.

Oxygen gradients in microdevices have been generated with O_2-N_2 mixtures.[66, 85, 176, 187-189] Using an off-chip multichannel gas mixer, Alder *et al.* fabricated oxygen concentration gradients with linear, exponential, and non-monotonic profiles ranging from 0 to 21% O_2 in a single device. By optimizing the thickness of PDMS between the flow and gas channels (120 μm), a discrete series of oxygen concentrations in the gas channels translated to smooth gradients of oxygen in the flow channels.[187] Oxygen gradients created using O_2-N_2 mixtures are limited by the number of gas channels, the period of the gas channel array, and the thickness of PDMS

between the gas and flow channels. Polinkovsky *et al.* fabricated microdevices that included on-chip gas mixing networks to generate a series of nine different gas mixtures using only two gas inlets, each fed with pure N_2 and O_2.[176] With serpentine channels and three stages of mixing, one microdevice exhibited a linear dependence of oxygen concentration on the channel number. The oxygen concentration increased from 0% to 100% O_2 across the array of microchannels in the device. Another microdevice created by Alder, Polinkovsky and colleagues with serpentine gas-mixing networks but with gas inlets of pure N_2 and 20.9% O_2, produced an exponential dependence of oxygen concentration on channel number, shifting from 0% O_2 in channel one to 20.9% O_2 in channel nine (**Fig. 2.2b**). A feasibility study looking at how an exponential change in oxygen affected *Escherichia coli* (*E. coli*) growth found that cells grew faster at a higher oxygen concentration but colony growth rates displayed the largest increase at near 0% O_2.[188] Although gas mixtures can achieve well-defined oxygen gradients, the disadvantages include intricate system design and setup and potential issues drying out the chamber when gas flow is used.

Liquid oxygen scavengers can remove oxygen chemically to achieve a desired oxygen concentration and bypass some potentially complicated microdevice designs. Chemicals that removed oxygen from solutions, or oxygen scavenging agents, have been used in PDMS microdevices to consume oxygen in culture and create oxygen gradients.[83, 177, 190, 191] One potential drawback to using an oxygen scavenging agent is its potential cytotoxicity at high chemical concentrations, which can lead to unwarranted cell stress and apoptosis.[192] Separating the oxygen scavenging liquid from cultured cells is paramount to limit chemical toxicity, and with microdevice fabrication techniques, separate channels can be manufactured to prevent unwarranted chemical interactions. In the lung model created by Chen *et al.*, pyrogallol,

a powerful organic reducing agent, was combined with sodium hydroxide to create an oxygen scavenging reaction, while hydrogen peroxide and sodium hypochlorite were combined in another chemical channel to generate oxygen.[83] The chemical channels created an oxygen gradient across a microdevice without interfering with the cell culture channel in between them, because each chemical channel was separated by 50 μm thick PDMS walls (**Fig. 2.2c**). The thickness of the walls was significant as it allowed for oxygen to diffuse readily but limited toxic chemical by-products from harming cells.

Using oxygen scavenging liquids with a gas permeable membrane to control oxygen gradients was first proposed by Skolimowski *et al.*[177] The novelty of Skolimowski *et al.* comes from a microfluidic device design that separates channels containing oxygen-scavenging liquid from chambers with media. The complete device includes two PMMA bottom layers for inlets and outlets and the oxygen scavenging liquid is composed of 10 mM sodium citrate. Next, there is a 60 μm thick PDMS oxygen permeable membrane. Lastly, there is a 150 μm thick cell culture chamber and a glass slide covered with oxygen sensing dye. The device was used to culture bacteria *Pseudomonas aeruginosa* (*P. aeruginosa*), which is a pathogenic, recurrent cause of lung infections in patients with cystic fibrosis. During metabolic challenges associated with varying oxygen availability within the mucus layers of the CF respiratory system, *P. aeruginosa* sustains colonization in the human airways by switching from aerobic to anaerobic respiration. Studies of *P. aeruginosa* in different dissolved oxygen environments required a device with controlled oxygen concentrations. The authors of this study reported that *P. aeruginosa* was negatively influenced by reduced oxygen, as a decrease in oxygen availability caused a reduction in the number of attached cells to the surface.

2.4.3. Computational Modeling

When designing MPS, in silico modelling is an invaluable tool for simulating physical parameters. Computational modelling not only saves resources, but also it can inform expected results or potential limitations of a MPS design. In silico models provide a theoretical data set to compare to in vitro results, a necessary engineering process that can simultaneously characterize and validate a model. Important categories to distinguish in an *in silico* model include steady-state versus dynamic, stochastic versus deterministic, continuous versus discrete and local versus distributed. Finite element analysis (FEA) is a form of discrete simulation described by local and deterministic calculations of ordinary or partial differential equations that represent the physical phenomenon at steady-state or dynamically. Other methods include lumped element modelling and Monte Carlo simulation, which can both evaluate and refine the underlying theory of models. The main physical phenomena simulated in in silico modelling include fluid dynamics, mass transfer, and solid mechanics, and, to a lesser extent, electronics, acoustics, and magnetics.

FEA is perhaps the most popular method for simulating fluid dynamics and mass transfer. The typical workflow of running a simulation involves describing the physics, building the model, establishing the boundary conditions, discretizing the model into elements, applying the relevant equations to the elements and boundaries, calculating the numerical solutions to the equations and, finally, visualizing the simulated model solutions. With known material properties and reasonable assumptions, thorough mathematical models have been used to predict experimental outcomes for various MPS.[110, 147, 177, 187, 193, 194]

Inside MPS, dynamic fluid flow is finely tuned and controlled in ways not possible on the macroscale due to inertial forces. Fluid dynamics of MPS are described by the Navier-Stokes equations and the fluid continuity equation, which maintain local conservation of momentum and

mass, respectively. Cell media is considered incompressible, Newtonian, and fully developed, with no-slip boundary conditions. This simplifies the Navier-Stokes equations and continuity equations, which can be further simplified if the model is simulated at steady-state and the fluid is in the laminar flow regime. In microchannels, fluid flows are generally considered laminar, because viscous forces far exceed inertial forces resulting in laminar flow.[75, 195]

Steady-state versus time-dependent is a parameter that can be changed based on the model and the experiment. At steady state, an oxygen transport model uses fluid dynamics equations to calculate flow profiles and mass transfer equations to calculate the oxygen concentration.[110] Navier-Stokes and fluid continuity are equations of fluid dynamics, while convection-diffusion, Brownian motion, Fick's Laws, and the mass continuity equation, are equations of mass transfer. Fluid dynamics equations are used to calculate the velocities and momentum of liquid and gaseous fluids, while mass transfer equations are used to calculate chemical concentrations and diffusion in those fluids. In order to accurately model oxygen levels in microfluidic devices both fluid dynamics and mass transport should be coupled. Typically, the solution to the fluid dynamics simulation is calculated and used as a variable in the mass transfer equations to solve for the concentration profile of dissolved oxygen due to convection and diffusion. On the microscale, there is no turbulent flow to enhance mixing, but laminar flow can be significant when dealing with gradients, therefore the convection-diffusion equation is used to define the concentration of oxygen species throughout a microchannel. The change in concentration over time can be solved for by calculating the flux of oxygen due to diffusion and convection then adjusting for any flux sources or sinks. Flux is the amount of a chemical species, oxygen, moving through an area over time. Cellular consumption rate, a value dependent on both cell type and cell density, is an example of an oxygen sink. Concentration profiles are generated

across the geometric space. With known values for parameters including density, viscosity, and diffusivity of oxygen in media, gas, and microdevice materials, the optimal oxygen tension for a respective cell culture can be simulated before experimental validation. Varying degrees of shear stress in a channel can be predicted with a simulation, but, experimentally, shear stress should be minimized to ensure long-term cell survival in any MPS.

Experimental cellular respiration values are important to consider for models that are meant to study cell mechanics *in vitro* compared to *in vivo*.[110, 147] Many different gases are generated as by-products of cellular respiration and metabolism; therefore, anaerobic microdevices must be able to evacuate gaseous products to sustain low oxygen levels. Oxygen consumption values for bacteria and mammalian cells are often reported in units of millimoles (mmol) per hour per number of cells and must be converted to oxygen flux for use in most computational models. Using Henry's Law and a known cellular respiration, the oxygen flux necessary to sustain a tightly packed monolayer of cells can be calculated. Henry's Law states that the concentration of a dissolved gas is equal to the partial pressure times the solubility coefficient of that gas.[196] At a constant temperature, the oxygen flux of cells in a microdevice can be calculated by multiplying a known concentration of oxygen by Henry's constant. The oxygen flux can represent a flux discontinuity at the individual cell boundary or entire monolayer surface. The cell density can then be altered to achieve a limited change in oxygen concentration across a material.[176] Analytical solutions to computational models of cellular respiration typically overestimate oxygen consumption in low oxygen environments because constant oxygen uptake is assumed, although many cell types report oxygen uptake decline following isolation.[193, 197, 198] An explicit approximation of Michaelis-Menten oxygen consumption kinetics offers numerical solutions that more closely correlate with measured values.

An *in silico* model of a physiological phenomenon, such as oxygen exchange in cells, can have its shortcomings, including assumptions such as constant influx of nutrients or constant cellular uptake. Such shortcomings can be bypassed with in-depth cellular experiments beforehand and knowledge of the differences between a given cell type *in vivo* versus *in vitro* culture. To better predict and control oxygen in a MPS, *in silico* models should account for fluctuations in oxygen levels due to cellular respiration and proliferation and be experimentally validated. Vertical oxygen gradients generated by highly active cells, such as hepatocytes that deplete oxygen at the media-cell surface interface faster than it is replenished by media oxygen diffusion, must be considered when comparing computations to experimental measurements.[199] Computational modelling of physiologic systems using the appropriate equations and assumptions can offer insight into complicated processes experienced by cells at the microscale level.

2D numerical simulations of oxygen profiles in microdevices have been created to simplify geometry and allow for quick computations.*[187]* Some negligible differences in peak oxygen concentration have been observed when comparing experimental results to 2D numerical simulations of non-monotonic oxygen concentrations in a microdevice with 9 gas channels containing various oxygen-nitrogen gas mixtures.*[187]* 3D numerical simulations of oxygen transport offer more defined oxygen profiles at the expense of computation time and simulation complexity, as an extra dimension necessitates more input parameters, detailed geometry, and boundary conditions to generate an accurate simulation that can be experimentally validated. One example of a 3D computational model of oxygen profiles in a liver MPS was created by Domansky *et al.*[110] The liver model, described above, included a reactor well and a reservoir well, fitted together inside a larger well where cell culture medium circulates between an open channel. Oxygen concentration varied with position and oxygen was replenished *via* the air-liquid interface

on top. The control volume region within the larger well extended from the air-liquid interface down to the scaffold in the reactor well and across the filter in the reservoir well. Fluid moved from the reservoir well to the reactor well with cells. It was assumed that fluid was completely mixed from the underlying pump and fluid entering the lower scaffold where cells were seeded had a uniform concentration. Fluid exiting the scaffold was assumed constant as no significant differences were observed experimentally at different regions of the scaffold due to uniform cell distributions. As fluid moved upward from the scaffold, oxygen concentration profiles were altered by the boundary conditions at the walls and convection and diffusion from the gas-liquid interface. Fluid moved back across an open channel into the reservoir well, creating a non-uniform oxygen concentration profile in the reservoir well. The control volume region within the larger well extended from the air-liquid interface down to the scaffold in the reactor well and across the filter in the reservoir well. Oxygen probes placed inside the reactor and reservoir wells confirmed the concentration of oxygen with an estimated error of less than 5%.

2.5. Measuring oxygen in microdevices

Although simulations of gas and fluid exchange offer insight into design parameters, real-time oxygen measurements are necessary to adjust and maintain desired oxygen levels in a MPS, as oxygen fluctuates continuously during cellular respiration and metabolism.[11] Measuring oxygen in MPS can be challenging due to the microscale features, complex flow profiles, need for sterility, and need for minimal oxygen consumption such that the oxygen concentration in the microenvironment does not change significantly.

Fortunately, there is a considerable body of literature on oxygen sensing. Much attention has been paid to gas-phase oxygen sensing[200, 201]; nevertheless, there are multiple reports

options for dissolved oxygen sensing in MPS. Oxygen can be measured in MPS by integrating either electrochemical or optical sensors, which are the most commonly reported technologies for dissolved oxygen measurement.[202-212] For further detail on the specific operation and performance of recent oxygen sensors, we suggest reading the focused review on microscale oxygen sensors which has been published by Oomen *et al.*[82] Herein, we will briefly define the most common oxygen sensors, which have been adapted to *in vitro* models—(1) amperometric oxygen sensors and (2) fluorescence or phosphorescence quenching oxygen sensors.

2.5.1. Electrochemical oxygen measurement

Electrochemical oxygen sensors can be categorized by their principle of operation: amperometric or potentiometric. Amperometric sensors are the most reported electrochemical technology for quantification of gaseous and dissolved oxygen.[213, 214] While potentiometric measurement of gaseous oxygen, potentiometric measurement of dissolved oxygen is emerging as a potential alternative.[215, 216]

For this review, we will focus on the more common amperometric measurement techniques, but we will briefly discuss the principles and emerging benefits of potentiometric measurement of dissolved oxygen. Equilibrium potential measurements enable oxygen measurement via the Nernst Equation (**Equation 1**), where E (Volts) is the potential difference of the electrochemical cell, E_0, is the potential of the reduction or oxidation reaction or the standard potential, R is the gas constant ($mol^{-1} \cdot K^{-1}$), F is Faraday's constant ($C \cdot mol^{-1}$), T is temperature (K), n is the number of electrons active in the reaction, and $[O_2]$ is the dissolved oxygen concentration ($mol \cdot L^{-1}$). The sensor output varies logarithmically with oxygen concentration, and if the solid electrolyte is an ionic conductor, the sensitivity of the equilibrium

potentiometric sensors is given by RT/nF and depends only on temperature, as the number of active electrons is fixed for the specific reaction at the electrode.

$$E = E_0 + 2.3\frac{\mathrm{R}T}{n\mathrm{F}}\log_{10}[\mathrm{O}_2] \qquad (1)$$

Potentiometric measurement have long been employed for the measurement of oxygen in the gas phase.[207, 217, 218] There have been few demonstrations of potentiometric dissolved oxygen sensors, using working electrodes that range from heavy metal alloys and ceramics to polymer films.[219-222] Potentiometric sensors for dissolved oxygen at physiologically-relevant oxygen concentrations have been most recently demonstrated by Zimmermann et al., but they do not demonstrate any operation in a cell culture system.[216] It should be noted, oxygen concentrations were measured from 0.1-228 μM, but their measurements significantly deviated from the classical Nernstian logarithmic transfer function (Eq. 1); therefore, potentiometry measurements in liquid phase systems may have to consider alternative models during operation. Ultimately, this demonstration may pave the way for future application of potentiometric sensors in MPS.

A vast majority of reported and prospective electrochemical oxygen sensors integrated into MPS operate via amperometry. Amperometric measurement of correlates the concentration of dissolved oxygen to the electrical current produced by an electrochemical reaction. A concentration gradient of oxygen, caused by its depletion at the electrode surface during the electrochemical reaction, leads to mass transport by diffusion, and the flux of oxygen is directly proportional to the reduction current according to Faraday's Law (**Equation 2**), where $i_{reduction}$ is the electrical current, F is Faraday's constant ($C \cdot mol^{-1}$), n is the number of electrons active in the reaction, A is the area of the electrode (m^2), and J_{O2} is the flux of oxygen ($mol \cdot m^{-2} \cdot s^{-1}$). Accordingly, by measuring the reduction current, the flux of oxygen can be related to the moles

of oxygen per unit volume, *i.e.* oxygen concentration, *via* Fick's Law. This conversion requires that the diffusion constant of oxygen in the selected medium is known and assumes the concentration of oxygen at the electrode surface is zero.

$$i_{reduction} = -n\mathrm{F}AJ_{O_2} \qquad (2)$$

In general, for amperometric systems the sensor performance (*e.g.,* magnitude of current, sensitivity, response time) depends on the electrode material (*e.g.,* gold or platinum)[223], surface area of the electrode (*i.e.,* improved sensitivity and response time result with larger electrode areas)[224, 225], temperature[225, 226], solubility of the oxygen in electrolyte[226], and oxygen diffusion rate through the electrolyte and any incorporated gas-permeable membrane.[225, 226] Due to these parameters, it is most common for electrochemical oxygen sensors to be operated via comparison to a calibration standard, rather than a Coulometric manner.

The most established of the amperometric oxygen sensors was developed by Clark *et al*.[227] The Clark-type (CT) electrode consists of a silver-silver chloride anode, a platinum cathode, an electrolyte, and a gas-permeable membrane (*e.g.,* cellophane or Teflon®).

The gas-permeable membrane covers all electrodes in the system, as illustrated in yellow in **Figure 2.3a**. Oxygen diffuses through the selective, gas-permeable membrane to the internal electrolyte covering the electrodes. The addition of a selective, gas-permeable membrane separates the medium under test from the electrolyte solution at the surface of the electrodes (typically potassium chloride). In addition, the gas-permeable membrane creates a diffusion profile where the response of the sensor is controlled by the oxygen diffusion instead of reaction kinetics on the electrode surface, *i.e.* the steady-state current is proportional to the concentration of dissolved oxygen.

During operation, oxygen is reduced to water at the cathode, and metallic silver is oxidized to silver chloride at the anode. Current is generated by reduction of oxygen at the cathode surface according to the reaction presented in **Equation 3**.[228] The current generated at the necessary overpotential for the electrochemical cell is proportional to the concentration of dissolved oxygen in the system. CT electrodes in microfluidic systems have been shown to operate in arrange of -0.6 V to -0.8 V.[227, 229] The applied potential is set such that all oxygen molecules are consumed at the cathode and the generated current is directly proportional to the oxygen diffusion from medium, across the membrane, and to the cathode.[230]

$$O_2 + 2H_2O + 4e^- \rightarrow 4OH^- \qquad (3)$$

It should be noted that the consumption of oxygen in CT electrodes is not trivial, and stable signals can be difficult to generate in small, microscale volumes. To overcome this challenge, there have been efforts for miniaturization of CT electrodes[231-235], but there are limited examples of CT electrodes being miniaturized and integrated into microfluidic devices.[236] Early attempts exhibited operational stability problems due to dissolution of the reference electrode material when operating in two-electrode configuration (*i.e.* no counter electrode). This deleterious effect could be limited by using three-electrode configurations, which drive most of the current through a counter electrode and little current flows through the reference electrode.[237] Park *et al.* created a miniaturized Clark electrode with a three electrode configuration for measuring cellular oxygen consumption, and it was reported that membrane type and working electrode area were the two dominant factors in determining both the stability and sensitivity of the oxygen sensor.[238]

As an alternative to CT-electrodes, direct amperometric oxygen sensors have been reported, including two electrode (working and reference/counter)[224, 228, 239] or three electrode (working, reference, and counter)[226, 240] configurations. **Figure 2.3b** illustrates an example MPS containing bare, thin-film platinum electrodes used as oxygen sensors. In this example, Weltin *et al.* incorporated amperometric oxygen sensors with small-molecule biosensors to achieve dynamic monitoring of human glioblastoma multiform T98G cells (**Fig. 2.3b**).[178] In direct amperometric oxygen sensors, oxygen is reduced at the working electrode without a selective membrane. The system is designed for diffusion-limited operation, such that the oxygen concentration is linearly proportional to the current. These direct amperometric oxygen sensors are typically operated as chronoamperometric measurements, in which a potential step is applied to the working electrode with respect to the reference electrode and the resulting current response is measured. The generated current density is linearly proportional to the concentration of dissolved oxygen.

As demonstrated in many examples, amperometric detection is advantageous for fast and sensitive detection of oxygen in the microchannels of MPS and many other bioreactors.[228, 241-244] Challenges to facile adoption and integration of oxygen sensing electrodes into MPS include: electrode fouling due to biological-electrode interactions, resultant signal drift, local oxygen consumption and depletion of internal electrolyte, material instability and dissolution, susceptibility to electrical interference, and signal fluctuation under flow.[157, 189]

While many of these challenges can be overcome by utilizing alternatives to CT electrodes or employing alternative electrochemical modalities, like potentiometry, there are also material and engineering design considerations that can improve the operation of integrated oxygen sensors.

Selective, gas-permeable and electrolyte-permeable membranes may also be considered for application as protective barriers in non-CT electrochemical oxygen sensors. Selective membranes or coatings of the sensor electrodes can be employed to reduce fouling and biological-electrode interactions. Bare metal electrodes are vulnerable to contamination from cell adhesion, protein adsorption and interaction with other electroactive species.[245] Many oxygen selective membranes are made from oxygen permeable polymers such as silicone[224, 246], polyethylene[247], polypropylene[225], and PDMS.[225, 229] However, the slower diffusional characteristic of such materials, as previously described (**Table 2.2**), may limit the dynamic sensing of oxygen in a rapidly evolving system. It should also be noted, that these gas-permeable coatings do not permit electrolyte transmission, and therefore are only suitable in solid-state gas oxygen sensors.[248-250] Select membrane materials, such as Nafion^{TM}, polyelectrolytes, and hydrogels, may better serve as electrode protectants, while enabling rapid diffusion of oxygen to and from the electrode surface and also behave as electrolyte and ionic conductors in aqueous media.[251-254]

The method of sensor fabrication and integration may also play a critical design role for instrumented MPS. Planar amperometric oxygen sensing electrodes on glass[224, 239] and flexible Kapton® [255] have been integrated in-line with microfluidic channels and are the most common. Bare metal electrodes can be fabricated *via* myriad vapor deposition processes. Rodrigues *et al.* designed planar amperometric oxygen and glucose sensors at the inlet and outlet of a PDMS chamber for cell culture analysis of hepatocytes; this approach provided real-time monitoring of the composition and consumption of nutrients in the cell culture medium before and after its contact with cells.[256] Weltin *et al.* also utilize a distributed sensing design in which the system included two oxygen sensors in the inlet, one electrode in the cell culture area,

and two electrodes in the outlet channel to investigate the oxygen concentration inside and outside of the cell culture and provide some spatial resolution of oxygen concentration. More complex microelectrode architectures have also been explored for oxygen sensing "on-chip." Lee *et al.* created amperometric gold oxygen sensing microneedles for evaluation of dissolved oxygen microprofiles. The fabricated microneedles were used to penetrate into the microfluidic channel for vertical measurement of dissolved oxygen levels in the microchannel, and as a pre-conditioning step, the electrodes were polarized before calibration.[228]

Lastly, preconditioning of electrodes is carried out when a dry sensor is first introduced to the solution for measurement. In bare metal electrodes, near-zero oxygen levels at the electrode surface can be achieved in less than one second; whereas, the introduction of high-surface area electrodes, hydrogel coatings, solid polyelectrolytes, or other membranes, may require increased preconditioning to achieve a stable baseline and accurate measurement of oxygen. Numerous strategies have been employed to reduce preconditioning times for planar amperometric oxygen sensors[257], and various materials have been used as a gas permeable membrane to control the time to and stability of the internal electrolyte for fabricating planar type oxygen sensors.[258-261]

2.5.2. Fluorescence/phosphorescence-based oxygen measurements

Luminescence is the cold-body radiation of light. Photoluminescence, which is luminescence due to the absorption of photons, is a property exploited for the quantification of oxygen concentration in the local microenvironment of the selected light-emitting substances, *i.e.* luminophores. Specifically, fluorescence and phosphorescence quenching are the predominant forms of luminescence-based optical sensors that can be integrated into both *in vitro* tissue

cultures and microfluidic devices for oxygen quantification. Fluorescence and phosphorescence are forms of photoluminescence that result from singlet-singlet electronic relaxation with nanosecond lifetimes and triplet-singlet electronic relaxation with microsecond or greater lifetimes, respectively.

Popular fluorescence and phosphorescence-based oxygen sensors operate by quenching of the excited states of luminophores by molecular oxygen.[262] Fluorescent and phosphorescent radiative emissions are generated when the excited molecule returns to the ground state from its singlet and triplet electronic states, respectively. If oxygen is present in the environment, it acts as an energy acceptor and non-radiatively quenches the excited singlet or triplet states of the molecule prior to relaxation and emission of photons. This energy transfer, *i.e.* quenching, leads to a decrease of the intensity and lifetime of the fluorescence and phosphorescence of the luminophore. The degree of quenching is determined by the probability of an encounter between an oxygen molecule and an indicator dye in its excited state.[263] Therefore, the change in fluorescence and phosphoresce intensity or lifetime is proportional to the molecular oxygen concentration. The quenching of the indicator dye can be modelled according to Stern-Volmer equation **(Equation 4)**:[264]

$$\frac{\tau_0}{\tau} = \frac{I_0}{I} = 1 + k_Q \tau_0 \, [\mathrm{O_2}] \qquad (4)$$

where τ_0 and I_0 are excited-state lifetime and luminescence intensity in the absence of O_2, $[\mathrm{O_2}]$ is the oxygen concentration, τ and I are the lifetime and intensity, respectively, at a given oxygen pressure, and k_Q is the quenching rate constant. According to the Stern-Volmer equation, the quenching of luminescence intensity by oxygen is non-linear. In practice, the quenching of luminescence intensity is non-linear due to inhomogeneity of the system's optical properties.

Compared to amperometric sensors, oxygen sensing by luminescence quenching is well suited for small fluid volumes and offers fast and stable detection of oxygen with minimal signal drift.[189] Optical sensing *via* luminescence quenching enables oxygen sensing without disturbing the microfluidic setup and provides spatiotemporal imaging of cell cultures during long-term studies.[265]

Luminophores for quantification of oxygen in microfluidic devices are affected by various factors such as efficiency of the quenching process, lifetime of the indicator dye, stability of the luminophore (*i.e.,* photobleaching and leaching), absorption and emission of spectra of the indicator dye, availability of optical components (*i.e.,* excitation and detection devices), and background interference (*i.e.,* autofluorescence from plasma and cells).[210]

There are two main groups of oxygen-sensitive indicators: ruthenium-based complexes and metalloporphyrin complexes (**Fig. 2.4, Table 2.3**). Tris(4,7-diphenyl-1,10-phenanthroline) ruthenium(II) dichloride ($[Ru(dpp)_3]Cl_2$) [85, 266-270] and ruthenium tris(2,2′-dipyridyl) dichloride ($[Ru(bpy)_3]Cl_2$) [83, 157, 187, 265, 271, 272] are commonly used ruthenium-based compounds for microfluidic devices. $[Ru(dpp)_3]Cl_2$ has longer excited state lifetimes (5.34 μs vs. 0.6 μs) and higher quantum yield of luminescence (Φ_L: 0.3 vs. 0.0042) than $[Ru(bpy)_3]Cl_2$.[273] Ruthenium-based dyes are photo-stable and have short excited state lifetimes (<10 μs) as compared to the excited state lifetimes of metalloporphyrin dyes.[273, 274] The ability of oxygen to quench a luminophore increases if the luminescent probe has long lived excited states (*i.e.*, natural lifetime of the excited state, τ_o, in the absence of oxygen), which in turn results in more sensitive oxygen sensors. Platinum (II)-5,10,15,20-tetrakis-(2,3,4,5,6-pentafluorphenyl)-porphyrin (PtTFPP) [275-278], palladium(II) or platinum(II) meso-tetra(4-fluorophenyl) tetrabenzoporphyrin (PdTPTBPF and PtTPTBPF) [279], palladium-meso-tetra (4-

carboxyphenyl) porphyrin (Pd-TCPP) [280], platinum octaethylporphyrin (PtOEP) [191], platinum octaethylporphine-ketone (Pt-OEPK) [189, 281], and Pt(II) meso-di(pentafuorophenyl)diphenyl porphyrin [282] are some of the commonly used metal porphyrin based oxygen sensors in microfluidic devices. Therefore, the oxygen sensors made by metal porphyrins are more sensitive to oxygen than ruthenium-based sensors popularized in earlier studies.

Indicator dyes are usually immobilized in polymeric or sol-gel matrices to protect the dyes from degradation and to reduce dye leaching. Several polymers are commonly used for immobilization of dyes in microfluidic devices. Indicator dyes such as PtTFPP and Pt-OEPK were embedded in polystyrene.[189, 275, 281] PtOEP, PdTCPP, PtTFPP and $[Ru(dpp)_3]Cl_2$ were incorporated into PDMS. [191, 268, 277, 280] Other matrices such as silica gels [266, 283], poly(sodium styrenesulfonate) (PSS) [271], and polyfluorenes [282] were also utilized as immobilization medium.

Properties of the luminescent dyes (*i.e.,* sensitivity, response time and Stern-Volmer calibration graph) are strongly dependent on the type of polymer used as it controls the oxygen diffusion through the polymer matrix.[284] Permeation of oxygen through a polymeric matrix is dependent on diffusion constant and solubility of oxygen within that matrix ($P = \mathrm{D}S$, where P: permeation rate, D: diffusion constant ($cm^2\ s^{-1}$), S: solubility of oxygen (cm^3 (STP) cm^{-3} $(cmHg)^{-1}$)). According to Amao *et al.*, PDMS has higher permeation rate than organic glassy polymers such as polystyrene (PS), poly(methyl methacrylate), and poly(vinly chloride) (PVC). Fluoropolymers exhibit high permeability to oxygen due to the high electronegativity of fluorine.[285] Andrew *et al.* studied the sensitivity, response and recovery times of Pt-OEP and Pd-OEP immobilized in cellulose acetate butyrate (CAB) and PMMA.[273] Pt-OEP and Pd-OEP

embedded in CAB polymer had higher oxygen sensitivities and smaller response and recovery times than similar luminophores embedded in PMMA polymer, which was attributed to higher permeability of oxygen in CAB. It was reported that incorporation of plasticizers, such as tributyl phosphate, increased the oxygen sensitivity of the sensors due to localization of the luminophores in plasticizer rich areas within the polymer. Moreover, substitution of Pt-OEP with Pd-OEP in CAB or PMMA film produced much more sensitive films because of a long lifetime of Pd-OEP than Pt-OEP (0.99 vs 0.0091 ms). Hartmann *et al.* investigated sensitivity of Pt-OEPK and Pd-OEPK in PVC and PS films and reported that Pd-OEPK had the highest oxygen sensitivity among other combinations of the Pt and Pd metal complexes in PVC and PS matrices.

There have been various methods for integration of luminescent oxygen sensors into microfluidic devices. Regardless of the integration technique, several criteria should be met for successful oxygen sensor integration. First, the oxygen sensitive dyes should not detach from the surface of the microchannel. Second, the indicator dye must withstand repeated cleaning steps (*i.e.,* solvent stability), and should not present any toxicological effects to cell cultures.[210] Lastly, the distribution of the indicator dye in the matrix and within the microfluidic channel should be homogenous as it changes the light intensity and spatial resolution of the intensity-based readout techniques.[286] Measuring oxygen inside microfluidic devices has been done using a commercial handheld oxygen probe (*e.g.,* Neofox, Ocean Optics^{TM}), which includes oxygen sensitive dyes at the tip of the probe.[137, 287-290] This method of measurement lacks the integration of oxygen sensors with microfluidics.

An alternative method for measuring oxygen inside a microchannel involves perfusing oxygen sensitive dye with media, where the fluorescent luminophore (*e.g.,* $[Ru(bpy)_3]Cl_2$) is injected into channels for oxygen monitoring.[83, 265, 272] This method may require

replenishment of the medium and does not provide an integrated sensing approach. An integrated oxygen sensing approach was reported by Ochs *et al.*, where a microfluidic chip was fabricated by spin coating PDMS polymer on a commercially available oxygen sensor foil. The PDMS surface was then treated with an oxygen plasma for bonding it to a complementary pre-molded PDMS piece for oxygen level measurement during cell culturing.[291] Sato *et al.* mixed an oxygen sensitive phosphorescent Pd-TCPP dye with PDMS polymer to create a thin oxygen sensing membrane by spin coating on a glass slide. Afterwards, the membrane was attached to the sealed O_2 and N_2 PDMS microchannels for detection of oxygen gradients in a microfluidic device.[280, 281] Wang *et al.* and Thomas *et al.* used a similar spin coating technique to spin coat phosphorescent PtOEP and PtTFPP embedded PDMS polymers on glass slides, respectively.[191, 277] Subsequently, the pre-molded PDMS pieces were combined with the spin coated O_2 sensing layers *via* plasma bonding to measure oxygen gradients in the microchannels. This way of luminescent dye integration into polymeric matrices yields more mechanically durable sensing layers as compared to physical adhesion. Lasave *et al.* and Chang-Yen *et al.* studied physical adsorption of the luminophore on glass substrates.[83, 282] Lasave *et al.* filled the microfluidic channel with oxygen sensitive conjugated polymer nanoparticles. Due to the positively charged quaternary ammonium groups, the oxygen sensitive sensor was adhered to the negatively charged glass surface. Similarly, Chang-Yen *et al.* used a layer-by-layer deposition technique for physical adsorption of the indicator dye on a glass substrate. The glass slides were dipped into a mixture of interpolyelectrolyte complex ($[Ru(bpy)_3]Cl_2$ with PS polymer) to form a negatively charged surface. The slides were subsequently dipped into a poly(diallyl dimethylammonium) chloride (PDDA) solution to form a positively charged surface. Repeated dipping formed alternating layers of a desired thickness. Other integration techniques such as

airbrush spraying of indicator dyes [279], wet etching of glass substrate and subsequent luminophore pipetting [189], knife-coating of luminophore solution onto glass slides [278], and recess-filling with an indicator dye, where the recesses were created *via* reactive ion etching of a silicon wafer or micro molding of a PDMS polymer have been reported.[267, 268]

Quenching of a luminophore dye results in a decrease in luminescence intensity and excited-state lifetime. Therefore, two main readout techniques (*e.g.*, intensity and lifetime) have been developed for measurement of oxygen concentration. The first readout technique, intensity-based oxygen sensing, is based on detection of luminescence intensity, which can be easily implemented compared to the lifetime-based readout techniques. In this technique, the luminophore is excited with an excitation light source and the emitted light intensity is measured with a detector. Intensity-based oxygen sensing has been implemented for quantification of oxygen in microfluidic devices.[83, 85, 187, 266, 267, 271] However, intensity-based oxygen measurement is dependent on concentration of luminophore, photobleaching, optoelectronic properties of excitation source and detector.[292] Therefore, ratiometric sensing has been proposed to overcome the disadvantages of the intensity-based measurement. In this technique, an oxygen-sensitive dye and an oxygen-insensitive dye were incorporated into the sensing film. The emission spectra of the dyes differ from each other and only the oxygen-sensitive dye is quenched by oxygen. The quantification of oxygen is made by taking the ratio of the luminescence intensity of the oxygen-sensitive dye to that of the oxygen-insensitive dye (**Fig. 2.3d**). This method reduces the effects of factors that are common to both dyes, such as sample inhomogeneity and variations in excitation light and detector sensitivity.[212] John *et al.* used ratiometric sensing based on fluorescent $[Ru(dpp)_3]Cl_2$ and safranin dyes for measurement of oxygen concentration in microtiter plates. The ratio of the luminescence intensities of both dyes

in the presence and absence of oxygen was related to the oxygen concentration by using the Stern-Volmer equation.[283] In another study, Ungerbock *et al.* used red emitting phosphorescent PtTFPP and green emitting Macrolex Fluorescent Yellow (MFY) dyes for measurement of the respiratory activity of HeLa carcinoma cells and human dermal fibroblasts *via* ratiometric sensing. MFY dye acts as an antenna dye for collection of blue light and transfers part of its energy to the Q-bands of the oxygen sensitive PtTFPP indicator dye, thus, eliminating the need for two different excitation sources.[278]

The second type of readout technique, lifetime-based oxygen sensing, measures the lifetime of the luminophore. The lifetime is defined as the average amount of time a fluorophore remains in the excited state following excitation.[293] Frequency [189, 279, 282] and time-domain [280, 292] lifetime measurements have been studied to measure oxygen concentration in microfluidics. Lasave *et al.* used phase fluorometer for measurement of enzyme activity of glucose oxidase.[282] The frequency domain technique applied a modulating excitation light to the luminophore with an LED and measured the emission of the light with a photodiode. The phase lag between the excitation light and the emitted light was measured using a reference LED for phase correction. The lifetime of the luminophore was calculated from the luminescent phase shifts according to **Equation 5**.

$$\tau = \frac{\tan\emptyset}{2\pi f}, \qquad (5)$$

where f is the modulation frequency and $\emptyset$ is the phase shift. The frequency-domain lifetime measurement is advantageous over the time-domain method for measurement of lifetimes of dyes with close emission wavelengths. In contrast to the frequency-domain lifetime measurement, the time-domain technique is based on "pulse and gate" method (*i.e.*, rapid

lifetime detection). The measurement starts with switching on the modulated excitation source (*i.e.*, square wave) for a short period of time. Then, the light source is turned off and the detector is turned on to allow measurement of the luminescent light at two different times (t_1 and t_2). The lifetime of the luminophore is calculated from the emission intensity decay curve according to **Equation 6**.[294]

$$\tau = \frac{t_2 - t_1}{\ln \frac{A_1}{A_2}}, \qquad (6)$$

where A_1 and A_2 are the photon counts at two different times. Sato *et al.* designed a microdevice for measurement of oxygen consumption rate of hepatocytes. The device used a pulsed laser at 532 nm and a photomultiplier for irradiation of the sensor and detection of the emitted phosphorescence, respectively.[280] Similarly, Sud *et al.* designed a microfluidic bioreactor for continuous O_2 monitoring of mouse myoblasts using fluorescence lifetime imaging microscopy (FLIM). The FLIM system included an excitation source (337 nm to 960 nm) and a gated CCD camera for image recording.[265] Overall, lifetime-based measurement is advantageous over intensity-based measurements because it is independent of concentration of luminophore, photobleaching, drifts in source intensity and detector sensitivity.[209]

2.6. Conclusion

Measuring and regulating oxygen levels in microdevices is paramount to develop the next generation of *in vitro* tools for studying human physiology and pathophysiology. Often microdevices used to study cell biology, tissue or organ function, or drug response studies are criticized for their simplicity. By using primary human cells and accurately recapitulating the *in vivo* environment inside a microdevice, basic scientific questions can be answered, and the design of more complex experiments can be better informed. Before designing a MPS, a desired

oxygen gradient or constant concentration must be defined using previous knowledge attained from *in vivo* measurements of oxygen in a human organ or hypothesized oxygen concentrations extrapolated from reported animal models. Materials should be chosen to generate cells-specific microenvironments and *in silico* models can help determine appropriate seeding densities and expected oxygen concentrations at material interfaces. Overall, the most important factors determining the success of a MPS are the ability to measure oxygen in real-time and adjust oxygen concentration easily. Microdevice architecture should inform the best oxygen sensor integration.

With more knowledge of the intricate and critical role of oxygen in physiologic and pathophysiologic phenomenon, microdevices can be fabricated that are more representative of true human organ and cell-level responses to damage or repair and lead to better predictions of drugs and cell therapies. It is important to consider how organ systems respond to oxygen fluctuations based on function. MPS should incorporate fluctuating oxygen, but this will only be realized with continuous, real-time oxygen sensing.

Table 2.1. Physiologic oxygen concentrations in selected normal tissues[12]

Organ	pO_2 (mmHg)	% O_2
Alveoli	110	14.5
Lung	43	5.6
Arterial blood	100	13.2
Kidney	72	9.5
Liver	41	5.4
Skin (superficial region)	9	1.3
Skin (sub-papillary plexus)	38	4.6
Brain	35	4.4
Intestinal tissue	58	7.6

Table 2.2. Oxygen diffusivity of common plastics

Material	O_2 diffusivity ($cm^2 \cdot s^{-1}$)	Ref.
Polydimethylsiloxane (PDMS)	$3.4 \pm 1 \times 10^{-5}$	[159]
Polyetheretherketone (PEEK)	1.38×10^{-6}	[295]
Polytetrafluoroethylene (PTFE)	2.83×10^{-7}	[296]
Polypropylene (PP)	$2.33 \pm 0.4 \times 10^{-7}$	[297]
Polystyrene (PS)	$2.3 \pm 0.2 \times 10^{-7}$	[164]
Polyurethane	1.16×10^{-7}	[298]
Polycarbonate (PC)	8.0×10^{-8}	[168]
Polyethylene terephthalate (PET)	2.89×10^{-8}	[299]
Polymethyl methacrylate (PMMA)	$2.7 \pm 0.2 \times 10^{-8}$	[174]

Table 2.3. Microfluidic devices with Ruthenium or Metalloporphyrin-based oxygen sensors

Probe	Detection Scheme	Culture or reaction	O_2 Range	Reference
Oxygen Sensitive Foil	Fluorescence (Intensity)	hepatocytes; endothelial cells; *Escherichia coli*	<20%	[291], [300]
$[Ru(bpy)_3]Cl_2$	Fluorescence (Intensity)	HepG2 cells, C2C12 cells (mouse myoblasts); MC3T3-E1 cells (mouse preosteoblast); human dermal microvascular endothelial cells; human lung adenocarcinoma (A549); porcine cardiomyocytes; b-TC-6 (transgenic insulin-secreting murine cells)	1-6%; 0-15%; 0-11 $mg \cdot L^{-1}$	[83], [85], [187], [266], [267], [272], [271]
	Fluorescence (Lifetime)	C2C12 cells; L2 and H4IIE cells (lung and liver)	1-8 $mg \cdot L^{-1}$	[157], [265], [301]
Ruthenium + Secondary Compound	Fluorescence (Ratiometric Intensity)	pancreatic islets; Neuronal tissue; HepG2 human hepatocellular carcinoma cells; NIH/3T3 fibroblasts; neonatal rat cardiomyocytes; *Corynebacterium glutamicum*	0-21%	[302], [137], [283], [303]
Pt or Pd porphyrins	Phosphorescence (Intensity)	oxidation of sulphite to sulphate human lung adenocarcinoma (A549); human cervical carcinoma (HeLa); *Escherichia coli*	<20% ; 0-100%; 0-40 $mg \cdot L^{-1}$; 0.03-0.2 atm	[191], [277], [281], [304]
	Phosphorescence (Lifetime)	enzymatic reactions; hepatocytes	0-21 kPa; 0-150 mmHg; < ~125 hPa; 0-42.5 ppm	[189], [279], [280], [282]
PtTFPP + MFY	Phosphorescence (Ratiometric Intensity)	human cervical carcinoma (HeLa); human dermal fibroblasts	0-21%; 0-200 hPa	[276], [278]

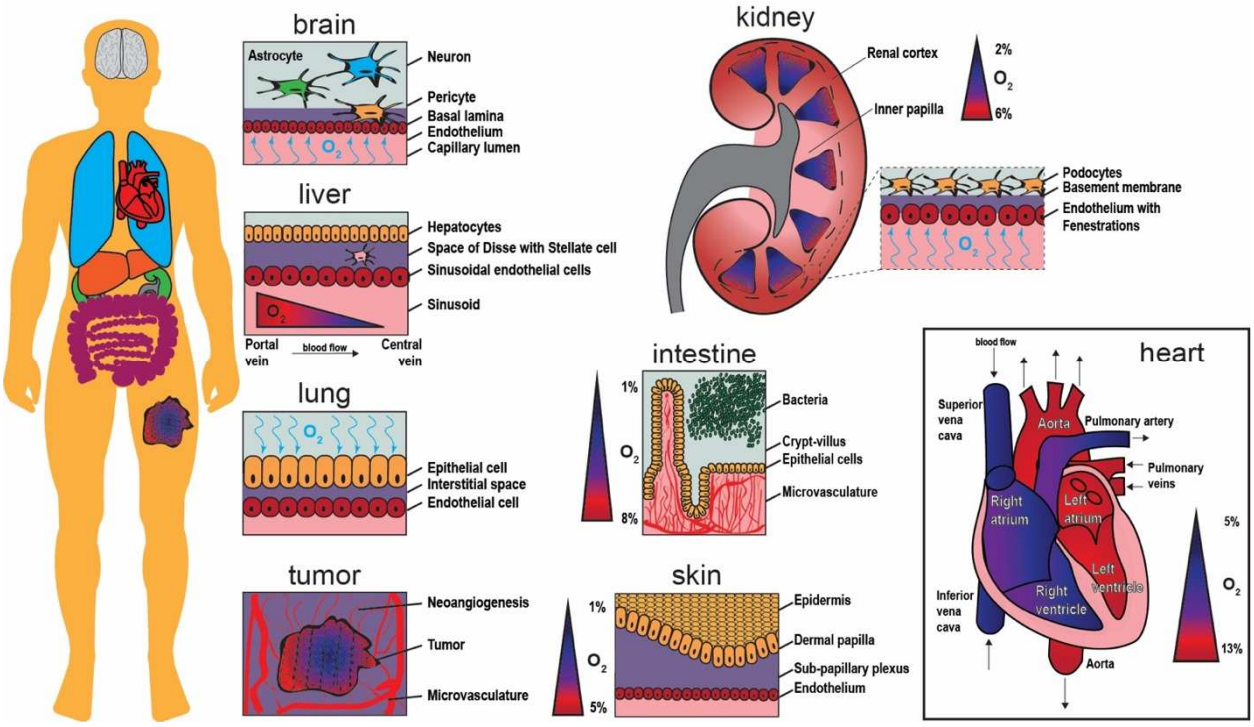

Figure 2.1. Schematic representations of oxygen content inside organs. The human body is composed of numerous oxygen gradients and organ-specific microenvironments that require microphysiological systems to study oxygen exchange in a tunable and controllable manner. The brain contains neurons, astrocytes, and pericytes situated above and within the basal lamina. Oxygen crosses the endothelium to reach brain cells *via* the capillary lumen. A tumor creates new vasculature as it grows (neoangiogenesis), while the core of the tumor continues to become more hypoxic. The lung receives oxygen in air, which then binds to hemoglobin molecules after crossing through the epithelium and interstitial space. For the liver, oxygen rich blood travels from the portal vein toward the central vein, providing nutrients to sinusoidal endothelial cells, stellate cells in the perisinusoidal space, and hepatocytes. The kidney contains oxygen gradients within each renal medulla and from the inner papilla to the renal cortex. The intestine has a steep oxygen gradient from the microvasculature underneath the crypt-villus axis to the bacteria populated lumen. The skin is an oxygen barrier with the epidermis at very low oxygen. The heart contains

numerous levels of oxygen as oxygen-poor blood flows into the vena cava and oxygen-rich blood exits *via* the aorta.

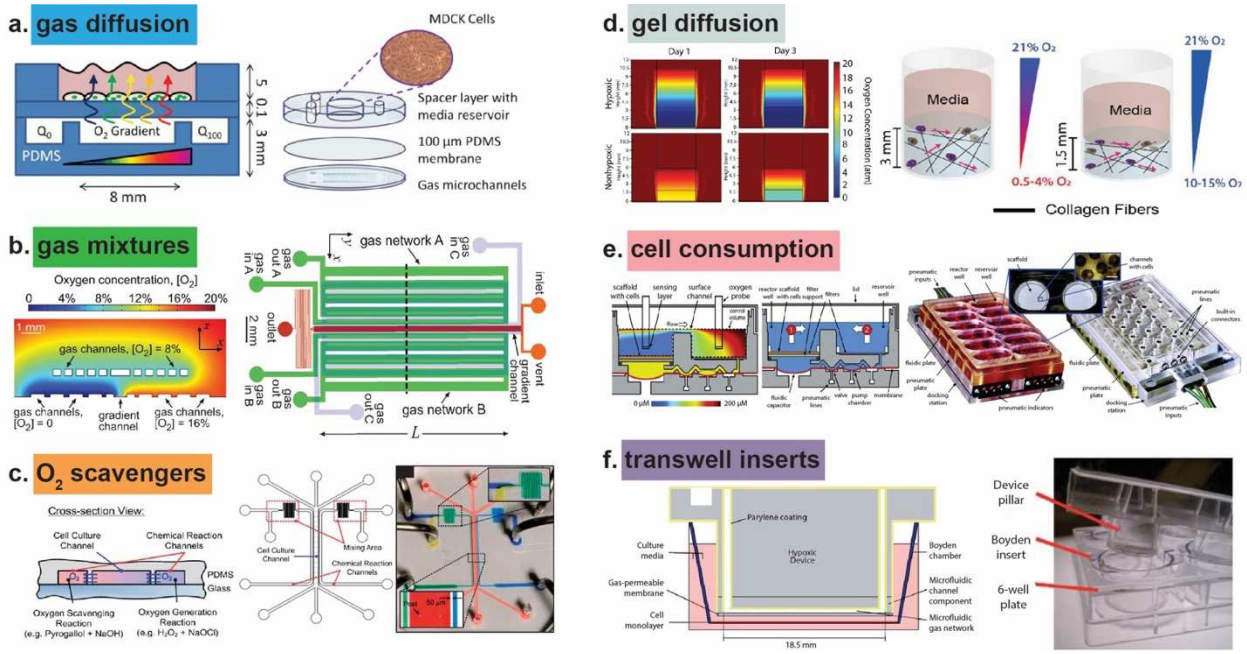

Figure 2.2. Methods for controlling oxygen in microphysiological systems (MPS) to study cellular responses. (a) Gas diffusion used to generate an oxygen gradient across a layer of Madin-Darby Canine Kidney (MDCK) cells. Reproduced from Ref.[88] with permission from The Royal Society of Chemistry. (b) Gas filled channels create an oxygen gradient from 0% to 20% oxygen. Reproduced from Ref. [188] with permission from The Royal Society of Chemistry. (c) Oxygen scavengers in leftmost chemical reaction channel remove oxygen, while oxygen generators in the rightmost channel create a gradient of oxygen between the chemical reaction channels, inside the cell culture channel. Reproduced from Ref. [83] with permission from The Royal Society of Chemistry. (d) Oxygen diffused through collagen hydrogels of various height and fiber density to create oxygen gradients. Reproduced from Ref. [146] with permission from The Royal Society of Chemistry. (e) Cells consume oxygen inside the liver MPS to create oxygen-limited environment. Reproduced from Ref. [110] with permission from The Royal Society of Chemistry. (f) Transwell insert contains Parylene coating to prevent

environmental oxygen from contaminating inner hypoxic device. Reproduced from Ref. [169] with permission from The Royal Society of Chemistry.

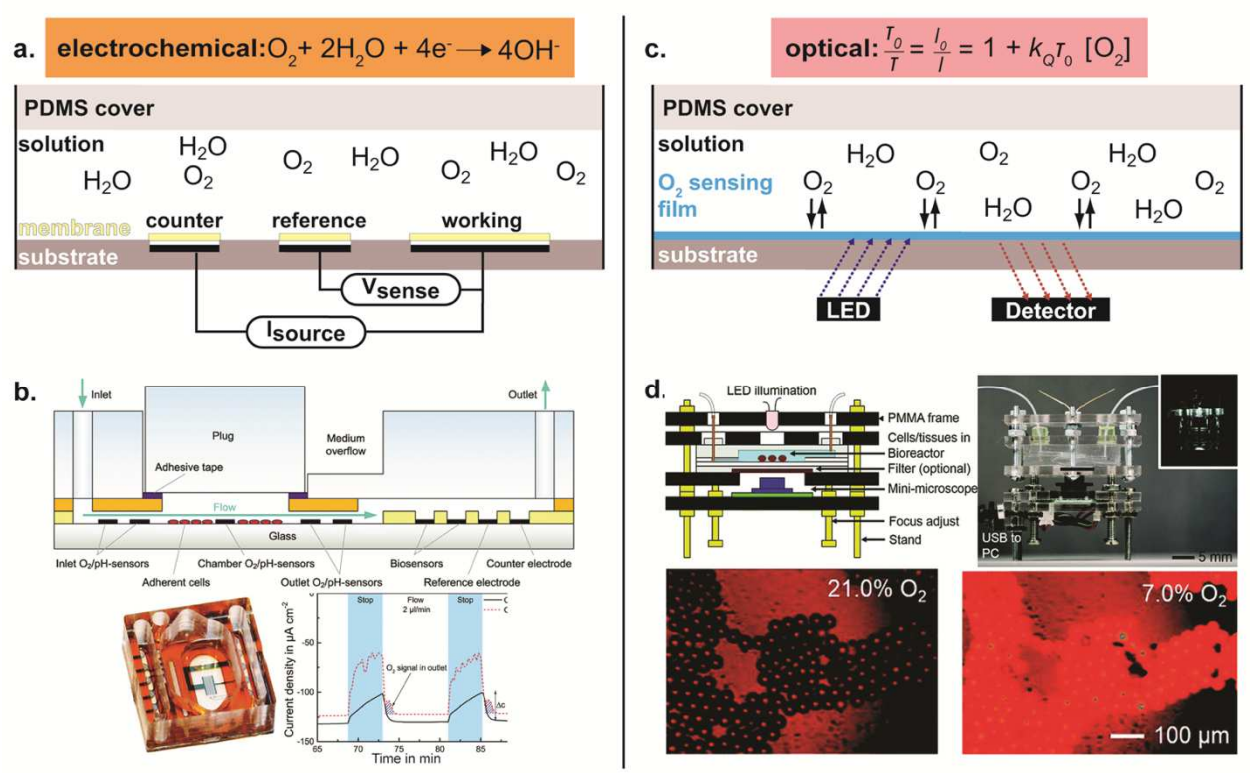

Figure 2.3. Measuring oxygen in microdevices. (a) Schematic of non-Clark type amperometric oxygen sensing. An optional membrane or coating can be applied over the electrodes to limit fouling or cell-electrode interactions. An oxygen-selective membrane can also be integrated to achieve a Clark-type system, *i.e.* using only an anode and cathode. (b) An example of amperometric oxygen sensing. (Top) Schematic of the fabricated microfluidic device. (Bottom, left) Fabricated microfluidic device with integrated electrochemical O_2 sensors. (Bottom, right) Amperometric continuous oxygen measurement. Reproduced from Ref. [178] with permission from The Royal Society of Chemistry. (c) Schematic of optical oxygen sensing. (d) An example of optical oxygen sensing. (Top, left) Schematic of the fabricated microfluidic device. (Top, right) Fabricated microfluidic device with integrated optical O_2 sensors. (Bottom) Fluorescent images of the microbeads doped with two dyes, oxygen sensitive ruthenium dye and oxygen-irresponsive

Nile blue, to 21% and 7% oxygen concentrations. Reproduced from Ref. [302] with permission from The Royal Society of Chemistry.

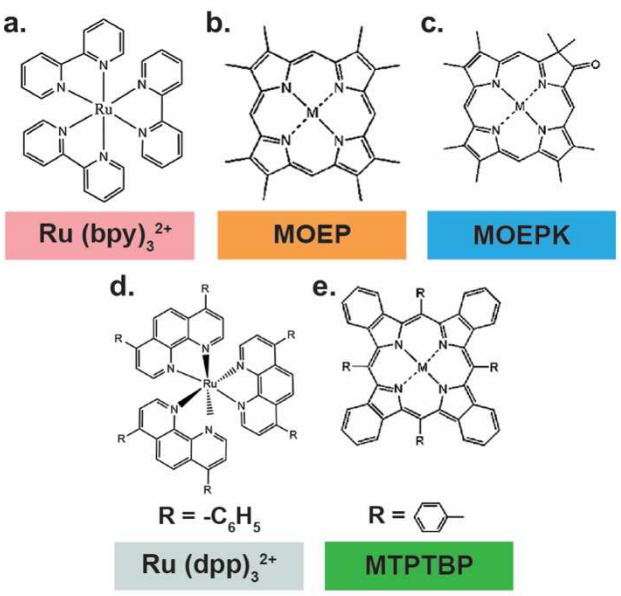

Figure 2.4. Common oxygen sensing via luminescent optical dyes. (a-d) Chemical structures of Ru(II) complexes and metalloporphyrins. M stands for Pt(II) or Pd(II) metal ions. Reproduced from Ref. [209] with permission from The Royal Society of Chemistry.

CHAPTER 3: INTEGRATED PHOSPHORESCENCE-BASED PHOTONIC BIOSENSOR (IPOB) FOR MONITORING OXYGEN LEVELS IN 3D CELL CULTURE SYSTEMS[2]

3.1. Overview

Physiological processes, such as respiration, circulation, digestion, and many pathologies alter oxygen concentration in the blood and tissue. When designing culture systems to recapitulate the *in vivo* oxygen environment, it is important to integrate systems for monitoring and controlling oxygen concentration. Herein, we report the design and engineering of a system to remotely monitor and control oxygen concentration inside a device for 3D cell culture. We integrate a photonic oxygen biosensor into the 3D tissue scaffold and regulate oxygen concentration *via* the control of purging gas flow. The integrated phosphorescence-based oxygen biosensor employs the quenching of palladium-benzoporphyrin by molecular oxygen to transduce the local oxygen concentration in the 3D tissue scaffold. The system is validated by testing the effects of normoxic and hypoxic culture conditions on healthy and tumorigenic breast epithelial cells, MCF-10A cells and BT474 cells, respectively. Under hypoxic conditions, both cell types exhibited upregulation of downstream target genes for the hypoxia marker gene, hypoxia-inducible factor 1α (HIF1A). Lastly, by monitoring the real-time fluctuation of oxygen concentration, we illustrated the formation of hypoxic culture conditions due to limited diffusion of oxygen through 3D tissue scaffolds.

[2] Chapter previously appeared in Biosensors and Bioelectronics. The original citation is as follows: Kristina R. Rivera, Patrick D. Erb, Ashlyn T. Young, Natalie A. Wisniewski, Scott T. Magness, Michael A. Daniele. Integrated phosphorescence-based photonic biosensor (iPOB) for monitoring oxygen levels in 3D cell culture systems. Biosensors and Bioelectronics, 123: 131-140, 2019.

3.2. Introduction

The measurement and control of oxygen concentration in cell culture has been a topic of intense discussion for more than 60 years.[305] Oxygen levels are dynamic in the human body, varying from less than 2% in the rectal lumen to 15% in the pulmonary alveoli.[12, 306] The terms normoxia, hypoxia and anoxia are relevant to discussions of cell environments, but they are often broadly defined across different research fields in terms of ranges and units, leading to misunderstandings concerning physiologic oxygen levels and oxygen levels outside the human body. Common descriptions of oxygen include partial pressure of oxygen (pO_2) or oxygen tension, with units of kilopascal (kPa)[307, 308], millimeters of mercury (mmHg)[269, 309, 310], dissolved oxygen concentration ($\mu mol \cdot L^{-1}$)[110, 311] and percent oxygen concentration (%)[312, 313]. Such terminology does not capture the physiological description of oxygen tension or oxygen concentration in the human body; thus, it is difficult to accurately replicate physiological oxygen levels in experimental conditions. Nonetheless, there are standard methods to convert between the relevant oxygen measurements. For example, using Henry's Law to convert from a dissolved oxygen concentration of 100 μM to a percent oxygen concentration of ≈ 7.5%, the temperature (here, 21°C) and pressure (atmospheric, 101.3 kPa) must be defined. Accordingly, at physiological temperature (37°C) and atmospheric pressure, the conversion to percent oxygen can be roughly estimated by dividing the dissolved oxygen by a factor of 10. This estimate can be used to estimate physiological oxygen conditions *in vitro.*

The physiological oxygen conditions affecting healthy physiology and pathologies vary widely across the tissues of the human body. During respiration, humans breathe air containing percent oxygen concentration of 20.9%, *i.e.* the partial pressure of oxygen in the environment (P_eO_2) is ≈ 21 kPa. The percent oxygen concentration is immediately reduced to ≈ 15% in the

pulmonary alveoli, where hemoglobin binds oxygen and transports it throughout the body inside blood.[12] Although oxygen is uniformly transported to the edge of the circulatory system through arterioles and capillaries, some parts of the body consume oxygen at higher rates. For example, the brain, with the highest metabolic activity per unit weight of any organ, consumes 20-25% of all the oxygen in the entire body [133, 134], while gut and muscle tissue demand variant oxygen levels depending on rest or contraction status.[314, 315] Consequently, a range of physiological oxygen levels exists throughout the body, including percent oxygen concentration of ≈ 10% in the kidneys, 7% in the intestines and less than 5% in the sub-papillary plexus region of the skin and brain tissues.[12] Apart from the entrance of the respiratory tract, tissue in the human body does not contain more than a percent oxygen concentration of ≈ 15%, and this should be considered to be the maximum oxygen concentration for *in vitro* normoxic tissue culture.

However, the standard tissue culture incubator is held at hyperoxic conditions. The standard tissue culture incubator, which most *in vitro* systems utilize, maintains a temperature of 37°C, recapitulating human body temperature at 100% relative humidity to ensure medium does not evaporate and cell metabolism is not compromised by changes in osmolarity. The gaseous mixture contained within the tissue culture incubator is composed of nitrogen gas (N_2), gaseous water (H_2O_g) and carbon dioxide (CO_2). When 20.9% oxygen gas (O_2) is added to the incubator containing 70.2% N_2, 6.2% H_2O_g and 5.0% CO_2, the resulting O_2 is 18.6% at sea level.[74] The oxygen concentration inside a normobaric incubator (18.6%) is hyperoxic in physiological terms, because no body tissue exists at a higher oxygen environment than the 15%.[316-318]

Ultimately, environmental oxygen differences between tissue culture and *in vivo* physiology can hinder translating research findings from benchtop to bedside. Studying cells in

inaccurate environments makes predicting appropriate drug dosages for *in vivo* models difficult, leading to drug failure during clinical trials.[319] For example, complex *in vitro* systems are often developed to investigate pathologies and novel therapies, especially tumorigenesis and metastases [320-322]; however, these systems do not accurately recapitulate the oxygen environment of *in vivo* tumors.[323] This is a particularly notable shortcoming because oxygen concentration has been implicated in tumor metastasis [67, 324, 325]. *In vivo* tumors create a low oxygen environment, *i.e.* average percent oxygen concentration of ≈ 1.5%, which becomes more hypoxic from outer edge to inner core region, where vasculature is leaky or absent.[142, 326]

To translate *in vitro* results and better predict the outcome of *in vivo* testing, the physiological oxygen environment surrounding a cell or tissue of interest must be accurately recapitulated. For example, hypoxia is implicated in a myriad of developmental and pathological functions.[37, 73, 149, 327] Hypoxia can be any physiologic environment in which a cell or tissue is responding to a reduced oxygen availability, regardless of the quantitative value assigned to the concentration of oxygen present. Creating a desired oxygen concentration and controlling it in a cell culture system is currently limited by the cost and feasibility of available techniques. Large hypoxic incubators can generate stable low oxygen environments, but they require high operating costs.[328, 329] Alternatively, a smaller hypoxic chamber with microtiter plates can be deoxygenated and placed inside a normobaric tissue culture incubator.[330] Microdevices that recapitulate the hypoxic environment of a tumor have been created using a variety of methods and materials, such as oxygen scavenging chemicals, gas supply channels and oxygen impermeable materials, as reviewed by Byrne et al.[331] These small hypoxic chambers are expensive to maintain, as they require significant gas exchange, and cannot be opened or manipulated easily to change media or collect samples during an experiment. With microdevice

technology, even smaller hypoxic chambers, on the scale of a single well in a microtiter plate, can be created in parallel to allow for multiple oxygen environments to be tested simultaneously.[187] Furthermore, with connections and ports, sampling of fluids can be performed to measure cellular responses while maintaining a hypoxic environment.[109]

In the aforementioned systems, an integrated monitoring systems and control loop is necessary to maintain the hypoxic environment as cells respond to oxygen deficient environments or injury by increasing cellular respiration. Real-time oxygen biosensors can be integrated into a cell culture system to create the first step in the control loop required to sustain a desired oxygen environment. Next, oxygen must be depleted or quickly expelled from the cell culture device, while maintaining appropriate nutrients and other molecules for cell culture. Hydrogels can be used to maintain a nutrient rich environment for cells, while N_2 can be used to expel free O_2 from the air above the hydrogel and medium.[66] By closely tracking and adjusting the level of oxygen in a microfluidic culture system, gas flow and medium can be simultaneously introduced and exchanged with minimal reagent usage or waste accumulation.

Herein, we present a method and system for real-time, remote monitoring and control of oxygen concentration in 3D cell cultures. The 3D culture and oxygen monitoring system is composed of (1) a microfluidic cell culture-gas exchange chamber and (2) an integrated phosphorescence-based oxygen biosensor (iPOB). The system was validated in a study to control hypoxic conditions and evaluate the effect of oxygen concentration on benign and tumorigenic breast epithelial cells, MCF-10A cells and BT474 cells, respectively.

3.3. Materials and methods

Fabrication of 3D culture and oxygen monitoring system

The 3D culture and oxygen monitoring system was fabricated using polymethyl methacrylate (PMMA) and photopolymer resin (Formlabs, Inc.). PMMA was chosen to fabricate the microfluidic cell culture chamber and gas exchange channels because it possesses a very low oxygen diffusion coefficient (2.7×10^{-8} $cm^2 \cdot s^{-1}$), as compared to polydimethylsiloxane and polycarbonate. [174, 331] PMMA was also selected because it can be easily laser cut or machined without significant variation between replicates. The photopolymer resin was 3D printed to form a bottom frame to support the 3D culture device and simultaneously house the optical reader for the iPOB (**Fig. 3.1a**). A Computer-Aided Design file for 3D printing is provided in the Online Supplementary Material.

The microfluidic cell culture chamber and gas exchange channels were fabricated from 5.8 mm and 3 mm polymethyl methacrylate (PMMA) sheets (44352, 44292; US Plastics). The microfluidic culture chamber was composed of a circular chamber with a diameter of 11 mm and rectangular gas channels of 8.3 mm by 1.0 mm by 3.0 mm for length, width and height of, respectively. Three PMMA layers were laser cut and annealed with acetone. The bottom and top pieces of PMMA were laser cut from a 3.0 mm-thick PMMA sheet, while the middle piece, where the circular cell culture chamber was located, was laser cut from a 5.8 mm-thick PMMA sheet. Briefly, to remove dust and burr material with minimal cracking, each PMMA surface was quickly wiped with 100% IPA solution and air dried. Acetone was added to each PMMA piece and pieces were stacked and bonded together between two sheets of stainless steel using a compression clamp. Annealing was performed inside a convection oven set at 80°C for 2 hours, then the device was cooled for 1 hour at 60°C. A rubber gasket was laser cut and placed on top

of the PMMA layer to seal the cell culture chamber and gas channels, prior to bolting together. The device was tested for leaks using water and cracks were sealed by application of dichloromethane to the seams (**Fig. 3.1b**).

Integrated phosphorescence-based oxygen biosensor (iPOB)

Oxygen concentration in the system was continuously measured with an iPOB by NIR phosphorescence lifetime fluorimetry (**Fig. 3.1c**). Briefly, the iPOB is composed of porous poly(2-hydroxyethyl methacrylate) (pHEMA) gel functionalized with palladium-benzoporphyrin derivatives (Pd-BPD) that respond to local oxygen concentrations via phosphorescence quenching, resulting in an oxygen dependent variation in phosphorescent lifetime (**Fig. 3.1d**).[332] The iPOB has been manufactured in a variety of sizes, but for all experiments presented here a disk-shaped iPOB with dimensions of 5 mm diameter and 0.5 mm thickness was used. The optical front-end of the NIR phosphorescence lifetime fluoroscope was inserted into the support frame below the 3D culture chamber. The iPOB and NIR phosphorescence lifetime fluoroscopes were provided by Profusa, Inc.

Breast epithelial cell culture

Immortalized benign human breast epithelial cells (MCF-10A, CRL-10317; ATCC) [333] and non-metastatic tumorigenic human breast epithelial cells (BT474, HTB-20; ATCC) [334] were cultured. 3D tissue constructs were composed of cells seeded inside 8.2 $mg \cdot mL^{-1}$ of High Concentration (HC) Matrigel Basement Membrane Matrix (354248; Corning). Detailed culture conditions and protocols for conversion from 2D adherent monolayers to 3D embedded cultures are provided in the Supplemental Material (**Appendix A**).

Computational model of gas flow in device

COMSOL Multiphysics® (Burlington, MA) was used to simulate the oxygen concentration inside the cell culture-gas exchange chamber. The oxygen transport was simulated for chambers operating under constant flow of N_2 at various flow rates to determine the amount of time necessary to create a hypoxic environment, which we have defined as <2% O_2 (**Table 3.1**). The geometry of the device was modeled in 3D to represent the cell culture-gas exchange chamber, comprised of medium, with a depth of 5.8 mm and surface area of 0.95 cm^2. Inlet and outlet gas channels, comprised of air, were modeled as ports feeding into the cell culture. A video of the simulation is provided in the Online Supplemental Material.

Characterization of iPOB and 3D culture system

For experiments requiring gas flow, metal barb adapters screwed into the top of the 3D culture device were connected to tubing and an N_2 tank. Gas flow was regulated using a pin valve and monitored with a mass flow meter with digital output (GFMS-010061; Aalborg GFM). The device included an input adapter for N_2 inflow and an output adapter for O_2 outflow (**Fig. 3.1a**). To characterize the iPOB and compare to the results of the computational models, initial experiments were performed inside a standard tissue culture incubator at 37°C. The iPOB was suspended in 1X PBS in the cell culture chamber. Oxygen concentration data was collected without N_2 flow for 15 minutes. Following a stabilization period, N_2 flow was introduced into the culture chamber at a constant rate (3, 5, or 7 $mL \cdot min^{-1}$) for 2 hours. The device was also tested with alternating N_2 flow at a high rate (8 $mL \cdot min^{-1}$) over a period of 6 hours to measure the time required to deoxygenate and reoxygenate the cell culture chamber. Lastly, the iPOB was

either embedded inside Matrigel® or placed in medium on top of Matrigel® inside the cell culture chamber and oxygen concentration was measured for 20 hours.

Real-time monitoring and control of oxygen concentration in 3D culture

To determine cellular response to sustained hypoxia, breast epithelial cells were grown to confluency 75 cm^2 culture flasks then trypsinized, counted and re-suspended in Matrigel® inside the cell culture chamber. MCF-10A cells were seeded at a concentration of 0.85 x 10^6 cells·ml^{-1} inside Matrigel® with the iPOB in the cell culture chamber. Following a Matrigel® polymerization period of 30 minutes at 37°C, the rubber gasket and lid were sealed onto the device. The optical reader was attached to the bottom of the device and lifetime, temperature and oxygen measurements were recorded for the duration of each experiment. The device was placed inside an incubator maintaining a temperature of 37°C, 5% CO_2 and 100% humidity and N_2 was introduced into the device at a rate of 6.0 mL·min^{-1}. The N_2 flow rate of 6.0 mL·min^{-1} was chosen to expel oxygen without evaporating liquid medium overlaid on the hydrogel. Within 2 hours, the iPOB reported the amount of oxygen inside the cell culture chamber had reached a hypoxic environment. The hypoxic condition was maintained for 24 hours with continuous N_2 flow. BT474 cell experiments were performed following the same procedure as explained above for MCF-10A cells, except BT474 cells were seeded in Matrigel® at a concentration of 0.6 x 10^6 cells·ml^{-1}, as previously reported. [335]

Immunohistochemistry and gene expression

After 24 hours under hypoxic conditions, cells were characterized for hypoxia induced responses by immunohistochemical (IHC) and quantitative real-time polymerase chain reaction

analyses (qRT-PCR). Samples were stained for cellular apoptosis marker active cleaved Caspase-3 Alexa Fluor 488 conjugate (rabbit, 1:50 dilution in protein block, Cat. No. 96035S; Cell Signaling) for 2 hours and nuclei counterstain bisbenzamide (1:1000 dilution in 1X PBS, Cat. No. 1155; Millipore Sigma) for 5 minutes at room temperature. BT474 cell samples were also stained for Laminin alpha V, beta II Tubulin and bisbenzamide. All samples were imaged using a laser scanning confocal microscope (Zeiss LSM 710) and image analysis was performed using ImageJ [336] to quantify Caspase-3 positive cells (dead cells) and DAPI positive cells (total cell number). From this analysis, we compared % cell death across BT474 and MCF-10A cells culture in either normoxic or hypoxic environments after 24 hours. To assess the expression of genes that are responsive to hypoxia, a portion of breast epithelial cells encapsulated in Matrigel® was collected for qRT-PCR analysis. For each sample and experiment, triplicates were made and normalized to 16S mRNA levels. Fold change was expressed relative to normoxic controls using ΔΔCT analysis.[337] All statistics for IHC quantification and gene expression were generated using a Student's t-test. In all statistical analysis, $p < 0.05$ was considered significant. Detailed materials and methods for the immunohistochemical and gene expression analysis are provided in the Supplemental Material (**Appendix A**).

3.4. Results and discussion

A system was designed and engineered for real-time monitoring and control of oxygen concentration in 3D cell culture (**Fig. 3.1**). For findings presented in this paper, an oxygen concentration will be considered hypoxic if it is less than 2% oxygen or ≈ 20 μM, and a normoxic oxygen concentration will be 18.6% oxygen or ≈ 186 μM (**Table 3.1**).

By using continuous gas exchange of N_2 and O_2 in the medium above the 3D tissue scaffold, oxygen concentration was precisely controlled to generate a range of normoxic and hypoxic conditions. N_2 displaces O_2 quickly inside the 3D culture-gas exchange chamber, similar to a tri-gas incubator. Tri-gas incubators create hypoxia by controlling CO_2 and O_2 using N_2 to purge ambient air during incubation.[338-340] On a much a smaller scale, the 3D culture-gas exchange chamber replaced O_2 with N_2 in the medium above the 3D tissue scaffold to create a hypoxic environment for culturing cells. An intermediate oxygen concentration, such as 5% oxygen, could be maintained for 24-hour culture with continuous N_2 flow rate lower than 3 $mL \cdot min^{-1}$.

Inside the 3D tissue scaffold, an iPOB was embedded and *via* NIR phosphorescence lifetime fluorimetry the oxygen concentration inside the culture was monitored (**Fig. 3.1c, d**). The operation of the iPOB is based on the principle of phosphorescence quenching of metalloporphyrins by molecular oxygen.[341, 342] The phosphorescent chromophore (porphyrin) of the probe molecule can be converted to the triplet state by light absorption, followed by return to the ground state either with light emission (phosphorescence and/or delayed fluorescence) or by energy transfer to molecular oxygen.[343] pHEMA is a biocompatible hydrogel and the porosity of the hydrogel facilitates liquid and gas exchange, along with penetration of the resident cell population. A portable phosphorescence lifetime fluoroscope was utilized to record the signal from the iPOB (Profusa, Inc.). Use of phosphorescence has been demonstrated as a viable method for measuring oxygen distribution in tissue in animals and humans.[341, 342, 344-346] The phosphorescence lifetime of the metalloporphyrins is inversely related to oxygenation and can be measured within 2 μs, providing an oxygen detection range from 2 to 70 μM.[332] For *in vitro* oxygen measurements

requiring phosphorescence lifetime detection in seconds, the detection range can be extended to 150 μM.

Computational model of gas flow and comparison to the experimental performance of the iPOB in the 3D culture and oxygen monitoring system

The computational model developed to recapitulate the geometry and fluid dynamics of the device predicted the amount of time a given N_2 flow rate would take to deoxygenate the entire 3D culture-gas exchange chamber. Representative results of the simulation are shown in **Fig. 3.2a**. The results of the simulations at various N_2 flow rates show that a N_2 flow rate of 7.0 $mL \cdot min^{-1}$ creates a hypoxic environment inside the cell culture chamber of P_{O2} = 1 kPa or ≈ 1% O_2 within 45 minutes (**Fig. 3.2b**).

To experimentally validate the computational models, the iPOB was suspended in PBS solution and N_2 flow was introduced into the 3D culture-gas exchange chamber. The phosphorescence intensity output of the iPOB was processed to calculate the phosphorescence lifetime decay (τ), as previously reported.[341] Phosphorescent lifetime decay of Pd-BPD correlates directly to the oxygen concentration of its surrounding environment.[347, 348]

Repeated cycling of N_2 flow for 6 hours at a flow rate of 8.0 $mL \cdot min^{-1}$ showed that the oxygen concentration equilibrated to normoxic conditions within one hour after N_2 inflow ceased, as shown in **Fig. 3.2c**. Based on the Einstein-Smoluchowski equation for diffusion of gases in solution ($t = 0.5 \cdot r^2 \cdot D^{-1}$)[349-353], where r equals the height of 500 μL of PBS inside the device (5.26 mm) and D is the diffusion coefficient of O_2 (2.46×10^{-9} $m^2 \cdot s^{-1}$[354]), the expected time required for O_2 to diffuse through PBS was calculated as ≈ 90 minutes. Because the oxygen concentration returned to normoxia in less than 1.5 hours once N_2 inflow ceased, the calculated

O_2 equilibration period through PBS agreed with the experimental cycling of N_2 for lifetime decay and oxygen concentration. Although an N_2 flow rate of 8.0 mL·min^{-1} was experimentally tested inside the device containing the iPOB suspended in PBS, when this high gas flow rate was used with the device containing a hydrogel and medium, we noticed the high N_2 flow rate caused evaporation of the liquid medium overlaid on the hydrogel. Previously reported values for gas flow rates used in hypoxic cell culture devices include a range from 5 mL·min^{-1} to as high as 20 mL·min^{-1}.[143, 144, 187, 188] Further optimization of N_2 flow with the hydrogel revealed that a flow rate of 6 mL·min^{-1} expelled oxygen rapidly while maintaining medium on top of the hydrogel (data not shown).

Experimentally tested flow rates of 3, 5 and 7 mL·min^{-1} reveal similar trends of deoxygenation as predicted by the computational simulations. At 3 mL·min^{-1}, the lowest N_2 flow rate tested, an oxygen concentration less than 27 μM (≈ 2.7% O_2) was achieved in less than 2 hours (**Fig. 3.2d**). Compared to the computation simulation at an N_2 flow rate of 3 mL·min^{-1}, which found an oxygen concentration less than 27 μM in 36 minutes, it took more time than predicted to achieved this oxygen concentration experimentally. At an N_2 flow rate of 5 mL·min^{-1}, an oxygen concentration less than 20 μM (≈ 2% O_2) was achieved in less than 40 minutes (**Fig. 3.2d**). The simulation found at this flow rate that an oxygen concentration less than 20 μM was achieved in 30 minutes, which agrees well with experimentally measured time. Finally, at 7 mL·min^{-1} N_2 flow rate, within 23 minutes an oxygen concentration less than 10 μM (≈ 1% O_2) was achieved (**Fig. 3.2d**) experimentally, which was approximately 25 minutes faster than the simulation predicted. Humidity and temperature change inside the incubator could account for slight differences between simulation and experimental results. The 3D culture-gas exchange

chamber and iPOB sustained repeated experimental testing at 37°C with no signs of damage or degradation.

In addition to testing the iPOB embedded inside the tissue scaffold, we tested the response of the iPOB in the medium above the tissue scaffold. We found that there was on average a 20 μM (≈ 2% O_2) decrease in oxygen concentration between the medium and inside the Matrigel® (**Fig. 3.3d**). When the iPOB was embedded inside Matrigel® the oxygen concentration was on average 119 μM (≈ 12% O_2). When the iPOB was placed in medium on top of the Matrigel® the oxygen concentration was on average 139 μM (≈ 14% O_2). A similar trend was recorded when the iPOB was inserted in "cell-free" tissue scaffolds and exposed to N_2 flow rate of 7.0 mL·min^{-1} (**Fig. 3.3e**). A higher oxygen level was measured on top of the tissue scaffold as compared to inside the tissue scaffold, until both conditions dropped below the hypoxic level (20 μM). These results illustrate the spatial resolution of the iPOB and the capability to identify the effects of the tissue scaffold on the oxygen transport; moreover, this demonstrates a method to monitor oxygen concentrations in thicker (> 2 mm) 3D tissue cultures.

Monitoring of oxygen concentration in 3D culture of healthy and tumorigenic breast epithelial cells

The variation of native oxygen environments and tumorigenic status of the two breast epithelial cell lines derived from the same native tissue make them optimal candidates to monitor and compare cellular responses to hypoxia for validation of the reported 3D cell culture and oxygen monitoring system. Benign human breast epithelial cells, MCF-10A cells, and tumorigenic human breast epithelial cells, BT474 cells, have been shown to respond to the same duration and magnitude of hypoxia with unique mRNA and protein expression levels.[355-357]

MCF-10A cells were derived from benign human breast tissue, where the concentration of oxygen has been reported to be greater than 9%; BT474 cells were derived from solid, invasive ductal breast carcinomas, where the concentration of oxygen has been reported to be as low as 0.3% oxygen.[358] The native oxygen environments from which the MCF-10A and BT474 cells are derived represent normoxia and hypoxia in breast tissue, respectively.

To compare MCF-10A and BT474 cellular response in the system after 24 hours of hypoxia, we fixed hydrogels containing cells and performed immunohistochemical (IHC) analysis for cleaved Caspase-3. Both MCF-10A and BT474 cells responded to hypoxic conditions by exhibiting significant cellular apoptosis, quantified as the ratio of apoptotic marker cleaved Caspase-3 positive cells to nuclei marker bisbenzamide positive cells (**Fig. 3.3a,b)**. Most importantly, MCF-10A cells exhibited a significantly higher percentage of cell death than BT474 cells. The increased cell death of MCF-10A cells in response to hypoxia, as compared to the tumorigenic BT474 cells, was not unexpected as MCF-10A cells typically occupy a higher oxygen environment and may experience hypoxic stress more quickly than tumorigenic breast epithelial cells. IHC analysis of cellular apoptosis showed that the hypoxic environment induced inside the system instigated the expected apoptotic responses in both MCF-10A and BT474 cells with an exacerbated response in the benign MCF-10A cells.

To investigate 3D cell morphology following hypoxic culture, we examined the cellular basement membrane and microtubules of BT474 cells by staining for Laminin, alpha V and beta II Tubulin, respectively. In BT474 cells cultured for 24 hours under hypoxic conditions, there was a noticeable absence of Laminin, alpha V, representing a lack of intact basement membrane, as compared to BT474 cells cultured under normoxic conditions for 24 hours (**Fig. 3.3c**). BT474 cells also exhibited lower levels of beta II Tubulin, as compared to BT474 cells cultured under

normoxic conditions. Confocal images collected from samples of normoxic and hypoxic cultured BT474 cells collectively suggest that the hypoxic environment imposed inside the device imparted morphological changes on the BT474 cells. Although the cell morphology of BT474 cells cultured under hypoxic conditions was qualitatively different than that of normoxic BT474 cells, a quantitative comparison was not made due to increased non-specific staining of the scaffold and hypoxia-induced cellular debris.

When culturing MCF-10A cells under both normoxic and hypoxic conditions, oxygen concentrations were measured below standard culture conditions, *i.e.* less than the conventional hypoxia (2% ≈ 20 μM) or normoxia (18.6% O_2 or ≈ 186 μM) conditions. Representative data from one culture period (20 hrs.) is displayed in **Figure 3.3f**. Under hypoxic conditions, an average oxygen concentration of 12 μM (≈ 1.2% O_2) was measured. Under normoxic conditions, an average oxygen concentration of 127 μM (≈ 13% O_2) was measured. When culturing BT474 cells in our system, even lower oxygen concentrations were measured in both the hypoxic and normoxic conditions (**Fig. 3.3g**). During the normoxic experiments, an average oxygen concentration of 95 μM (≈ 9.5% O_2) was measured, while during the hypoxic experiments the oxygen concentration was 6.4 μM (≈ 0.6% O_2). These results confirm the 18.6% O_2 contained within the normobaric incubator is significantly limited by diffusion through the thickness of the cell-laden tissue scaffold and medium (4.21 mm), which is corroborated by oxygen concentration measurements made in the "cell free" experiments. The type of cell, either non-tumorigenic (MCF10A cells) or tumorigenic (BT474 cells), had an impact on the amount of oxygen measured under each condition.

To determine whether known genetic responders to hypoxia were upregulated following hypoxic conditioning in our device, we evaluated the expression of selected downstream target

genes of HIF1 (Hypoxia inducible factor-1) using mRNA collected from BT474 and MCF-10A cells. The HIF protein is a transcription factor composed of two subunits: the oxygen-dependent α subunit and the ubiquitously expressed ß subunit.[359] During hypoxia, the HIF-1α subunit is rescued from oxygen-dependent degradation in the proteasome and activates a complement of downstream target genes.[32, 360] The stabilized HIF-1 transcriptional activator binds genetic enhancer sequences in the promoter of HIF-1 target genes.[361] A subset of these target genes include the following: vascular endothelial growth factor (VEGF)[362], solute carrier family 2 member 1 (SLC2A1)[363] and BCL2 (B-cell lymphoma 2) interacting protein 3 (BNIP3)[364], which are important for angiogenesis, glucose metabolism and apoptosis, respectively.

Since the oxygen-dependent HIF1A is primarily regulated at the post-transcriptional level by nuclear localization and protein stabilization [365, 366], we did not expect substantial changes in HIF1A mRNA following 24-hour hypoxia. While HIF1A slightly increased in both BT474 and MCF-10A cells, there was a significant and substantial increase in HIF1 target genes VEGFA, SLC2A1 and BNIP3. Interestingly, the tumorigenic BT474 cells had the most significant upregulation of BNIP3 when compared to normoxic controls (**Fig. 3.4a**, purple bars, $p < 0.05$, Student's *t*-test). These results contrast greatly with non-tumorigenic MCF-10A cells, which displayed little change in BNIP3 expression. Although BNIP3 upregulation has been previously reported following similar durations of hypoxic conditioning [367], cells encapsulated in a hydrogel 3D tissue construct differ from previous culture methods in which MCF-10A cells were adherent to tissue culture plates. The 3D tissue scaffold could provide a barrier to protect MCF-10A cells from apoptotic injury, leading to less mRNA expression of BNIP3. Another study comparing durations of hypoxia reported BNIP3 expression peaks after 72 hours, suggesting BNIP3 expression is a later hypoxic response than downstream targets VEGFA and

SLC2A1.[364] Overall, the difference in BNIP3 expression between MCF-10A cells and BT474 cells suggests tumorigenic BT474 cells are more susceptible to hypoxia-induced apoptosis, as evident from 12-fold increase in BNIP3 expression. MCF-10A cells cultured under hypoxic conditions showed a significant 5.0-fold increase in VEGFA and 7.0-fold increase in SLC2A1 expression, as compared to normoxic controls (**Fig. 3.4b**, purple bars, $p < 0.05$, Student's *t*-test). These results support that non-tumorigenic MCF-10A cells initially respond to hypoxia by primarily upregulating the angiogenic (VEGFA) and glycolytic (SLC2A1) pathways. The upregulation of VEGFA mRNA present in both BT474 and MCF-10A cells agrees with previous findings, which showed an increase in endogenous secreted VEGF protein levels via ELISA and VEGF mRNA levels via RT-PCR for the same cell types under similar 24-hour hypoxic (defined as 0.5% O_2) conditions.[355]

While there were consistent increases in VEGFA and SLC2A1 gene expression between the two cell types, in BT474 cells HIF1A expression showed a slight but significant increase, with little change in MCF-10A cells. Because activation of HIF-1 depends in part on post-transcriptional stabilization of HIF-1α [368], its near-absence in mRNA cell samples after 24 hours of hypoxic conditioning is unsurprising [369], and the upregulation of downstream reporter genes VEGFA, SLC2A1 and BNIP3 further supports this interpretation. Overall, the 24-hour restrictive oxygen conditioning revealed key hypoxia-dependent genes were upregulated within the hypoxia device. These changes were consistent with low oxygen levels that were measured by the iPOB embedded within the Matrigel® containing either BT474 or MCF-10A cells.

3.5. Conclusion

Microdevices built for *in vitro* cell culture with iPOBs provide a route to study cells and tissues in more physiologically-relevant oxygen environments. By quickly and accurately monitoring local oxygen concentration in 3D tissue cultures, the oxygen concentration can be manipulated to recapitulate healthy and pathological environments. The reported 3D culture and oxygen monitoring system demonstrated a simple design to remotely monitor oxygen concentration during tissue culture. We recorded fluctuations in the local tissue environment due to external controls (N_2 inflow). We demonstrate *in situ* controllable and reversible oxygen conditions over a relatively short period of time and large oxygen concentration range. As more knowledge concerning the micro-environments surrounding cells is discovered, *in vitro* cell, tissue and organ models must sustain relevant oxygen levels to generate more "translatable" results.

During the reported validation testing, MCF-10A and BT474 breast epithelial cells revealed distinct differences in response to the same magnitude and duration of hypoxia. IHC analysis showed a significant increase in apoptotic marker cleaved Caspase-3 for both cell types. Genetic analysis differentiated the response of the cell types to hypoxic culture conditions by revealing sizable and significant upregulation of only apoptotic marker BNIP3 for tumorigenic BT474 cells and significant upregulation of both VEGFA and SLC2A1 for MCF-10A cells. The additional upregulation of hypoxia-associated genes VEGFA and SLC2A1 in MCF-10A cells demonstrates that non-tumorigenic breast epithelial cells are more effected by hypoxia, as compared to BT474 cells. Intrinsic markers of hypoxia and their downstream targets, provide a mechanistic basis for interpreting cellular response to different oxygen levels. The distinct hypoxic pathways responsible for benign and tumorigenic breast epithelial cell differences could

be further investigated using the device and iPOB. With fine control over the oxygen microenvironment, questions concerning the mechanisms influencing cell fate through hypoxic pathways can be answered. When combined with in-line analytical techniques, such as media sampling and imaging, the iPOBs provide a powerful method to remotely measure the interstitial oxygen environment, monitor cell culture performance and study complex phenomena in 3D tissue models.

3.6. Acknowledgements

This work was done in collaboration with the National Science Foundation (EEC1160483) through a NSF Nanosystems Engineering Research Center (NERC) for Advanced Self-Powered Systems of Integrated Sensors and Technologies (ASSIST). ATY is supported through the NIH Integrative Vascular Biology Traineeship (NIH T32HL069768). The authors would also like to acknowledge Drs. Scott Nichols and Erin Sproul, and Sierra Guidry from Profusa, Inc. for useful training with Profusa software and helpful discussions.

Table 3.1. ***Definitions of Relevant Oxygen Environments at 37℃***

Environment	O_2 (%)	pO_2 (kPa)	cO_2 (μM)
"Normoxia"	21.0	19.9	210
Normoxia (incubator)	18.6	17.7	186
Low Oxygen	5.0	4.75	50.2
Hypoxia	2.0	1.90	20.1
Near Anoxia	0.5	0.48	5.02
Anoxia	0.0	0.0	0.0

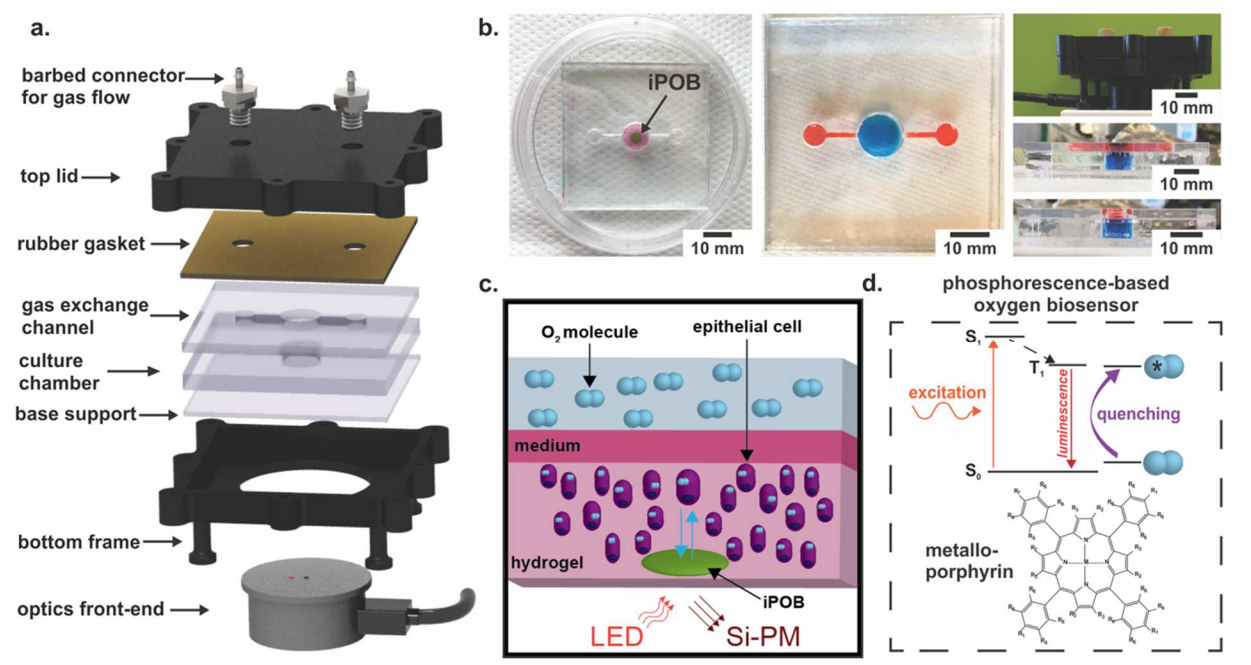

Figure 3.1. 3D Culture and oxygen monitoring system. (a) A schematic of device compartments. A photopolymer resin bottom frame supports PMMA cell culture chamber and gas exchange channel. Rubber gasket seals gas flow into and out of the culture chamber and gas exchange channel. Barbed connectors screwed into the top lid provide gas flow into and out of the device. The optical connects to a phosophorescence-lifetime fluorimeter and interrogates the culture chamber, where the 5 mm diameter, 0.5 mm thick integrated phosphorescence-based oxygen biosensor (iPOB) is located. (b) Photographs of device. *Left:* Image of device with iPOB (black arrow) embedded in hydrogel. *Middle and Bottom Right:* Images of the assembled device with red and blue dyes to differentiate the gas channels and cell culture chamber, respectively. *Top Right:* Device enclosed inside frame with optical reader underneath (c) Schematic of oxygen sensing via hydrogel iPOB inside hydrogel containing cells. The iPOB is composed of poly(2-hydroxyethyl methacrylate) gels functionalized with palladium-benzoporphyrin derivatives (Pd-BPD). The photoluminescence excitation and detection wavelengths are 630 nm and 800 nm, respectively. (d)

Modified Jablonski diagram demonstrating the scheme of oxygen concentration detection from porphyrin luminescence. Luminescence from the triplet state in porphyrin is quenched by energy transfer to molecular oxygen, resulting in a correlated decrease in phosphorescence lifetime.

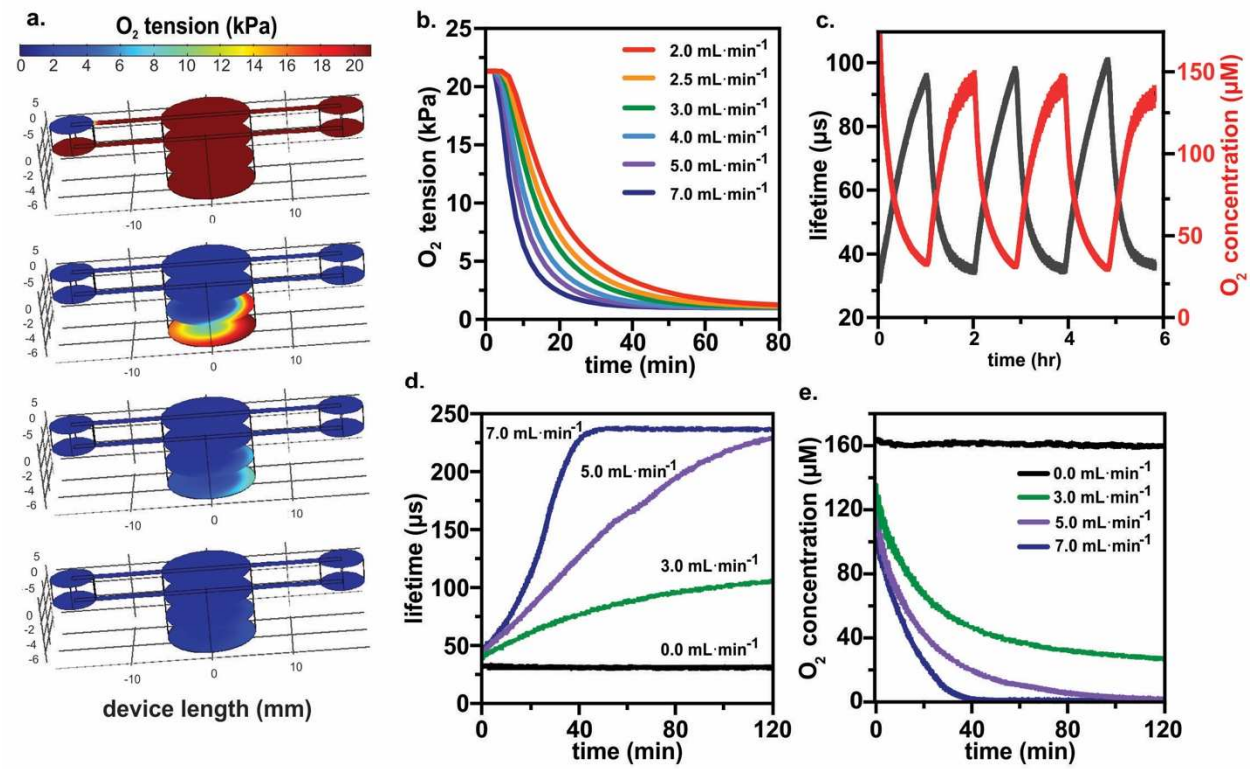

Figure 3.2. Computational Model of oxygen concentration in 3D culture and monitoring with Integrated Phosphorescence-based Oxygen Biosensor (iPOB). (a) Results from COMSOL Multiphysics® computational model of the 3D culture-gas exchange chamber showing N_2 flow at 5.0 mL·min^{-1} used to purge O_2 from the left inlet to the right outlet over a 50-minute interval, with four color maps displaying oxygen tension after 0, 10, 30 and 50 minutes. The color maps display the oxygen tension from 0 to 21 kPa. (b) COMSOL Multiphysics® simulation results of N_2 flow at various flow rates show the amount of oxygen inside the bottom of the cell culture chamber decreases more rapidly with increased N_2 flow rates. (c) Experimental results of purging and re-oxygenating the culture chamber by turning on and off N_2 at a flow rate of 8.0 mL·min^{-1} over 6 hrs and allowing for passive diffusion of oxygen from the atmosphere into the cell culture chamber. (d) Experimental results illustrating the operation of the iPOB in PBS measuring changes in phosphorescence lifetime at different N_2 flow rates. (e) Conversion of phosphorescent lifetime to

oxygen concentration for iPOB in PBS at different N_2 flow rates. Note the hypoxic environment (O_2 concentration < 20 μM) created in < 1 hr at N_2 flow rate of 7.0 $mL \cdot min^{-1}$.

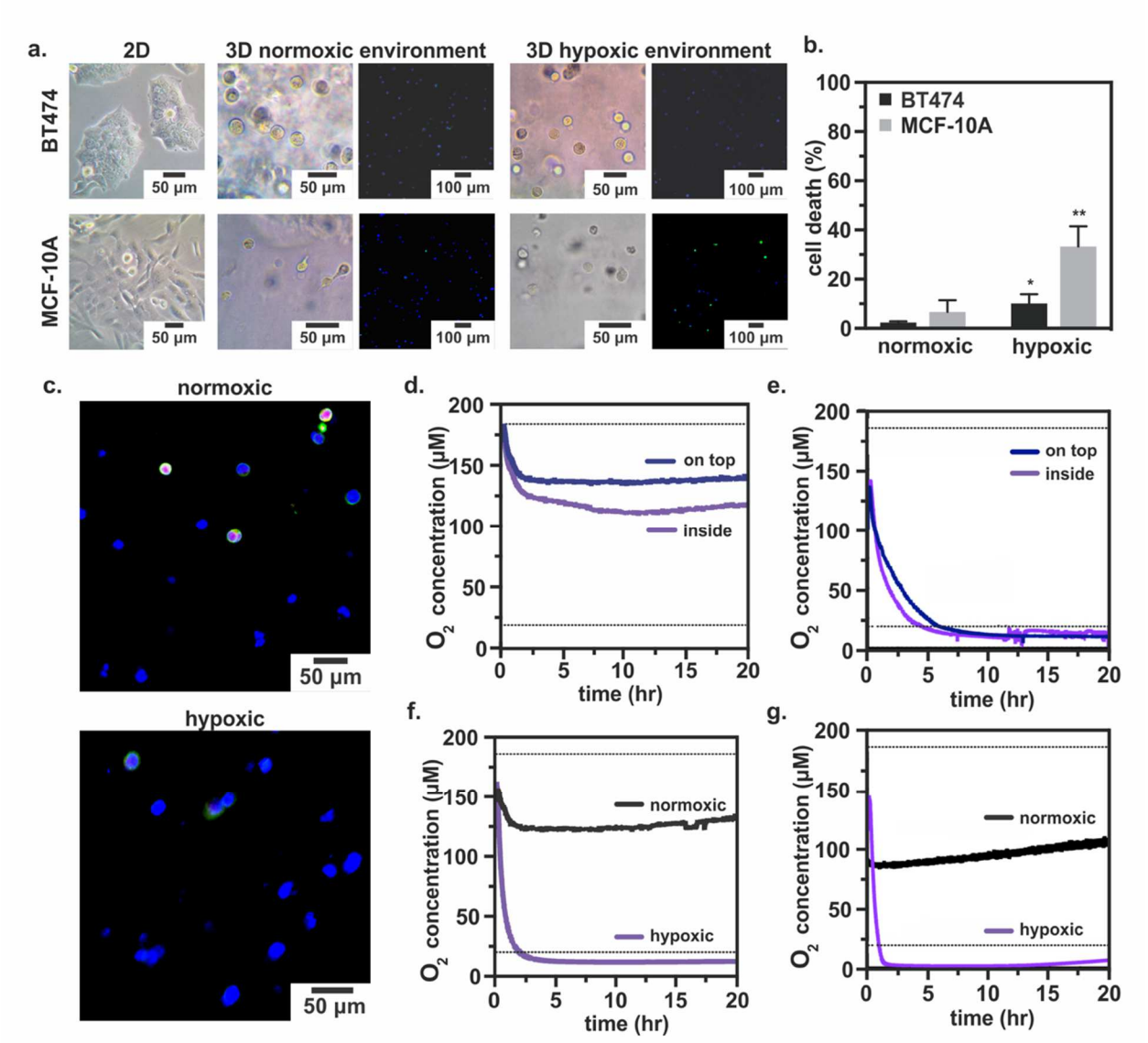

Figure 3.3. Monitoring and controlling oxygen concentration in 3D cell culture. (a) *Left:* Breast epithelial cells grown in T-75 flasks for 6 days. *Middle:* Breast epithelial cells embedded in Matrigel® and cultured in a normoxic environment for 24 hours. Fluorescent images: Caspase-3 (green), DAPI (blue). *Right:* Breast epithelial cells embedded in Matrigel® and cultured in a hypoxic environment for 24 hours. Fluorescent images: Caspase-3 (green), DAPI (blue). (b) Quantification of cell death from confocal images using ratio of Caspase-3 positive cells to DAPI positive cells. n = 3; *p<0.05, **p<0.01. (c) Fluorescent micrographs of BT474 cells showing

basement membrane (Laminin alpha V, red), microtubules (Beta II tubulin, green) and nuclei (Bisbenzimide, blue) after 24 hours of normoxic or hypoxic culture inside the device. (d) Integrated Phosphorescence-based Oxygen Biosensor (iPOB) measurements of oxygen concentration in "cell-free" tissue scaffolds over 20 hours. There is less oxygen inside the tissue scaffold (shown in purple) than on top of the tissue scaffold (shown in blue). (e) iPOB measurements of oxygen concentration in "cell-free" tissue scaffolds exposed to an N_2 flow rate of 7.0 $mL \cdot min^{-1}$ over 20 hours. (f) iPOB measurements from inside the tissue scaffold for MCF-10A cells cultured under hypoxic and normoxic conditions (shown in purple and black, respectively) for 20 hours. Under hypoxic conditions, average oxygen concentration of 12 μM (≈ 1.2% O_2) was measured. Under normoxic conditions, an average oxygen concentration of 127 μM (≈ 13% O_2) was measured. (g) iPOB measurements from inside the tissue scaffold for BT474 cells cultured under hypoxic and normoxic conditions (shown in purple and black, respectively) for 20 hours. Under hypoxic conditions, average oxygen concentration of 6.4 μM (≈ 0.6% O_2) was measured. Under normoxic conditions, an average oxygen concentration of 95 μM (≈ 9.5% O_2) was measured. Horizontal dashed lines are the normoxic oxygen concentration (186 μM) and hypoxic oxygen concentration (20 μM).

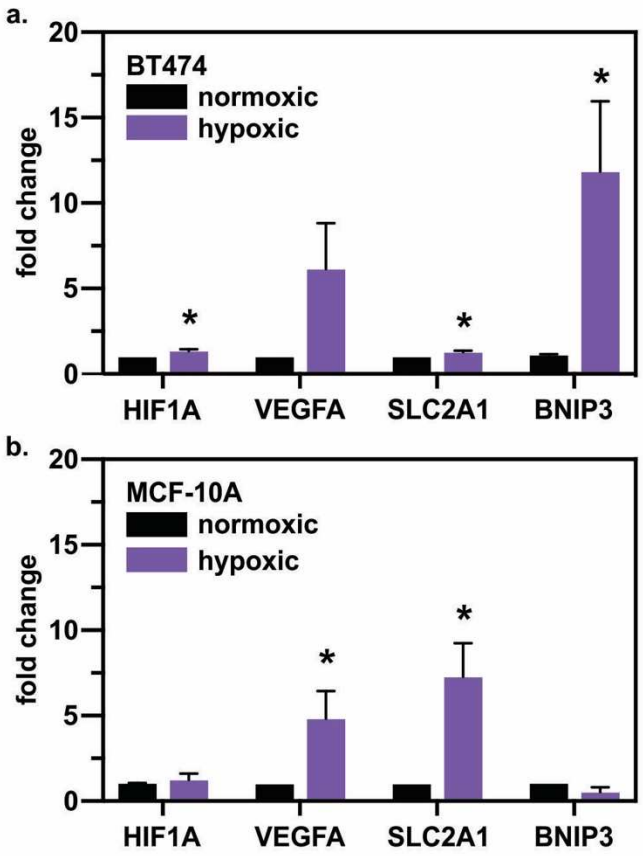

Figure 3.4. Response of breast epithelial cells to hypoxic culture conditions. (a) Gene expression analysis of BT474 cells after 24 hours of hypoxic or normoxic conditioning (purple and black bars, respectively). Hypoxia-associated genes including HIF1A, VEGFA, SLC2A1 and BNIP3 mRNA measured by qRT-PCR relative to the average expression in normoxic (21% oxygen) controls. n = 4; *$p<0.05$. (b) Gene expression analysis of MCF-10A cells after 24 hours of hypoxic or normoxic conditioning (purple and black bars, respectively). Hypoxia-associated genes including HIF1A, VEGFA, SLC2A1 and BNIP3 mRNA measured by qRT-PCR relative to the average expression in normoxic (21% oxygen) controls. n = 4; *$p<0.05$.

CHAPTER 4: SEVERE HYPOXIA PREPARES HUMAN INTESTINAL STEM CELLS FOR SURVIVAL AND PRIMES RESPONSE TO INFLAMMATORY MEDIATORS[3]

4.1. Overview

Oxygenated blood flow throughout the small intestine is vital to homeostatic regulation of epithelial cell function. Ischemia/Reperfusion injury is marked by a blockage of blood flow and the initiation of an inadequate oxygen, or hypoxic, microenvironment. Many intestinal diseases, including chronic inflammation and ulcerative colitis, are also coupled with tissue hypoxia. A novel microphysiological system (MPS) has been developed to deliver various durations and magnitudes of oxygen to primary human intestinal epithelial stem cells (ISCs). The MPS allows for precise remote monitoring and control of oxygen concentrations in real-time at the cell surface interface. Using the MPS, dynamic changes in gene expression in populations of human small intestinal ISCs, along with single cell transcriptomics, reveal key hypoxia-dependent responses. ISCs isolated and reintroduced to an oxygen environment show increased organoid survival with increasing duration of hypoxia. A set of hypoxia-dependent cytokine receptors, including interleukin 6 (IL6), interleukin 10 (IL10), and interleukin 22 (IL22), are found to be upregulated in human ISCs following hypoxia.

[3] Full list of contributing authors: Kristina R. Rivera, Michael J. Czerwinski, Vladimir A. Pozdin, Ming Yao, Michael A. Daniele, and Scott T. Magness.

4.2. Introduction

Cellular respiration in complex multi-layered tissues relies on a constant supply of oxygen to maintain healthy physiologic states. The majority of cells in a tissue are perfused by a vast network of vessels that terminate in capillary beds where oxygen is released to adjacent cells in a local microenvironment.[12] Cells that comprise a tissue can experience marked differences in physiologic oxygen concentrations, such as in the intestinal microarchitectural framework of the crypt-villus axis where crypt-based cells experience higher oxygen levels compared with the cells at the tips of the villi.[11] Here a steep gradient is set-up within oxygen microenvironments that are ~10-fold different within just ~100 cell distances.[370] While these differences are tolerated as normal, sudden or dramatic changes in the magnitude and duration of oxygen loss, known as hypoxia, triggers a rapid transcriptional response mediated by hypoxia-inducible factors (HIFs) in an attempt to spare cellular functions. HIF response appears to be a universal property of cells across various tissues and is likely an adaptation that enables cells facing injury or disease to modify functions to preserve cell viability when oxygen levels fall below physiologic ranges with disrupted blood flow.[149, 371]

Clinical presentation of larger mesenteric vasculature occlusion brought on by bowel strangulation, aneurysm, organ harvest for small bowel transplantation, and neonatal necrotizing enterocolitis can produce an ischemic event, or loss of oxygenated blood flow to the intestine.[18] Less appreciable are conditions like chronic inflammation or ulcerated bowel that cause vasoconstriction and disrupt the capillary beds, leading to localized hypoxic events.[21, 50] While ischemic hypoxia is harmful, counterintuitively, reperfusion with oxygenated blood can promote further tissue injury as reintroduction of oxygen produces highly toxic reactive oxygen species (ROS). Ischemia-reperfusion (IR) injury has been nicely characterized in porcine and human

translational models.[50, 372] Collectively, the findings indicate that short term (30 minute) ischemia followed by reperfusion is well tolerated and recoverable, however, longer ischemic times (>45 minutes) followed by reperfusion produces profound loss of barrier function, increased translocation of endotoxin, and substantial inflammatory response characterized by release of inflammatory cytokine mediators and immune cell infiltration.[16] These studies indicated that the human differentiated intestinal epithelium is exquisitely sensitive to hypoxia and that the subsequent immune response is a feature of epithelial repair dynamics.

What remains unclear is how the duration and magnitude of hypoxia specifically impact the human intestinal stem cell (ISC) population, which must be spared for epithelial replacement and healing. Porcine models of prolonged IR-injury (1-4 hours) demonstrate a reduction of active ISC (aISC) markers, *Lgr5* and *Sox9,* and enrichment of the reserve ISC (rISC) marker, Hopx, suggesting Hopx+ cells are more tolerant to I/R-injury and might contribute to epithelial recovery.[373] The human translational model suggests only long-term IR-injury of 2 hours produces appreciable apoptosis in the crypt zone, however, it is unclear what cell types are sensitive to IR-induced cell death. In culture, monolayers of primary mouse epithelium reenact a hypoxia-associated 'injury-regeneration' cycle where oxygen tension appears to be a functional switch between injury and epithelial regeneration in the colonic epithelium.[374] Also in mice, ischemic preconditioning of intestinal tissue has been shown to improve tissue repair[375] and reduce cell death during ischemia by activating ISCs.[376] Interestingly, in humans the colonic epithelium is less susceptible to IR-induced injury demonstrated by increased apoptosis in the small intestinal crypts and villi, immune cell infiltration, and expression of injury-related cytokines.[377] These studies suggest variable and perhaps divergent hypoxia-dependent responses of ISCs in different species and across different regions of the small intestine and colon.

They also reveal gaps in knowledge related to important mechanisms human ISCs engage in during short and long-term hypoxic events.

Investigating the impact of hypoxia on human ISCs has been historically challenging due to the limited physiologically relevant models, ethical considerations of human research, and lack of high-resolution *in vitro* platforms that are required to recreate hypoxic environments where oxygen levels can be exquisitely tailored and monitored in real time. In this study we developed a microphysiological system (MPS) to deliver various durations and magnitudes of hypoxia to primary human ISCs. The MPS allows for precise remote monitoring and control of oxygen concentrations in real-time at the cell surface interface. We use the MPS to explore the dynamic changes in gene expression in populations of human small intestinal ISCs and at cell-resolution using single cell transcriptomics to reveal key hypoxia-dependent responses. Our analysis concentrates on a set of hypoxia-dependent cytokine receptors that are regulated in human ISCs, and we extend these findings to test immune-related cytokine mechanisms that impact ISC survival and function after experimental reoxygenation. Aside from a new high-resolution picture of dynamic transcriptomic changes and functional consequence that occur in ISCs from the onset of a hypoxic event until reperfusion, our study underscores important immune related influences that directly impact ISCs post-IR-injury. Our study has important implications for better understanding ISC behavior in gross clinical presentation of IR-injury to focal ischemic events that occur in IBD-related hypoxia.

4.3. Results

A new microphysiological system (MPS) enables precise regulation and real-time monitoring of oxygen levels at the cell-media interface

Existing platforms were incapable of supporting ISC expansion and providing direct measurements of oxygen levels in real-time at the cell-media interface, therefore, we developed a novel microphysiological system (MPS) the size of a standard microscope slide where oxygen levels could be tailored to precise levels in five independent wells, each containing a hydrogel scaffold that facilitates ISC expansion (**Fig. 4.1A, B**). The MPS was designed as a closed system in which ambient air was sparged over each well via continuous delivery of mixed gases. A biocompatible integrated phosphorescent oxygen sensor (iPOB) was placed on the hydrogel scaffold surface to provide real-time oxygen measurements specifically at the media-cell interface (**Fig. 4.1B**). Oxygen levels were quantified by the iPOB using Near Infrared (NIR) phosphorescence lifetime fluorimetry, as local oxygen quenches phosphorescence, resulting in detectable change in lifetime using a commercially available optical system (**Fig. 4.1A, C**).[332] The iPOBs are highly sensitive and validate that different oxygen levels can be generated with integration of an off-chip gas mixer (**Fig. B.1**).[378] Oxygen levels achieve equilibrium inside the intestinal MPS within less than an hour and can be stably and indefinitely maintained in the presence of constant gas flow (**Fig. 4.1D**). The MPS represents a small, highly sensitive, scalable and portable system that can accurately quantify the magnitude of hypoxia inside culture wells. The MPS is fabricated from relatively inexpensive commercially available materials and can be sterilized and reused many times. While the MPS is enclosed in a 3D-printed light-tight container required for phosphorescence detection during each study, the wells can be easily accessed to

refresh media, add compounds, and perform a variety of downstream assays including microscopy, transcriptomic analysis, and immunostaining.

The MPS supports culture of human ISC monolayers that respond to an induced hypoxic environment

We recently developed methods that support indefinite expansion of human ISCs isolated from intestinal organ transplant donors[60], and we integrated the ISC monolayer culture into the MPS. Human jejunal ISCs were cultured inside each well of the MPS, and once confluent, an iPOB was added to the cell surface during a media exchange, and the iPOB remained in place on the epithelial cell surface for the full duration of each experiment. We performed an initial characterization of ISCs cultured in the MPS under normoxic conditions by microscopy and immunofluorescence staining. ISCs were cultured to confluence using conditioned expansion media (EM) that supports Wnt-signaling and ISC maintenance.[379, 380] ISCs reached confluence within 4 days as monitored by brightfield microscopy and cells expressed the epithelial cell tight junction protein, occludin (**Fig. 4.2A**). ISC monolayers demonstrated pervasive expression of SOX9, which primarily marks ISCs and progenitor cells *in vivo[381, 382]*, and a 6-hour pulse with S-phase marker, EdU, indicated cells in the monolayer were proliferating (**Fig. 4.2A**). These results indicate the MPS is biocompatible with primary human cell culture and supports a monolayer composed of cells consistent with ISCs.

Since reliable antibodies against human ISCs are not available, we performed single-cell RNA-sequencing (scRNAseq) to understand the extent to which cells cultured in the MPS under ISC expansion conditions possessed gene expression patterns consistent with ISCs (**Fig 4.2B**). Human jejunal ISCs were cultured on expansion scaffolds in EM under normoxic conditions,

which represents the starting conditions for all experiments. Cells were dissociated to single cells, and scRNAseq libraries were generated from ~2000 cells. After computational filtering, dimensional reduction using UMAP was performed on the remaining 1640 cells for data visualization (**Fig. 4.2B**). Although a transcriptomic signature for freshly isolated human ISCs has not been described, we interrogated each cell for the expression of LGR5, OLFM4, and ASCL2, three biomarkers that exhibit restricted expression to the active ISC crypt-based columnar cells in mouse small intestine.[383-385] The data demonstrate ~68% of the cells express the general proliferation markers mKI67 or PCNA, and while all three mouse-associated biomarkers are expressed, OLFM4 was the most broadly expressed in ~67% of cells cultured in ISC expansion conditions. Differentiated lineage biomarkers alkaline phosphatase (ALPI; absorptive enterocytes), and Mucin2 (MUC2; goblet cells) were not appreciably expressed, and no expression for Defensin 5A (DEFA5A; Paneth cells), Chromogranin A (CHGA; enteroendocrine cells), and Doublecortin Like Kinase 1 (DCLK1; tuft cells) was detected (**Fig. 4.2B**). It is important to note that while scRNAseq is a powerful high-resolution technique, low expressed genes can sometimes be undetected in the analysis, and thus, biomarker expression at the single-cell level can be underrepresented. Sequencing depth per cell is on the order of 100-fold lower than that from bulk sequencing, which decreases the sensitivity of gene detection accordingly. However, these data, together with more extensive analyses (**Fig. B.2**), indicate that most cells in the monolayer cultures are proliferative cells expressing biomarkers consistent with murine ISCs and suggest the vast majority of cells have not engaged terminal differentiation programs (**Fig. B.2**).

To better understand the extent to which human ISC expansion cultures demonstrated functional ISC activity, cells were dissociated to single cells and applied to conventional 3-dimensional (3D) cultures to assess organoid forming efficiency (OFE), a proxy for *in vivo* ISC

activity.[386] Micro-Cell Raft Arrays (CRAs) were used as a highly accurate method to quantify thousands of putative ISCs that have organoid forming potential.[198, 387] Single cells plated in CRA micro wells were identified, quantified, and each candidate ISC was followed over a 6 day culture period. The data demonstrate ~4% of cells cultured in the MPS under ISC expansion conditions generated an organoid (**Fig. 4.2C**). While this is a relatively low incidence, it is consistent with OFE of FACS-isolated murine Lgr5-EGFP expressing single cells cultured under similar conditions [198, 388] and human ISCs cultured for the same period of time in synthetic matrices [388], suggesting the full extent of ISC activity of cells cultured in the MPS is captured by the 3D culture conditions. The ability to form organoids from single cells isolated from the normoxic MPS shows that the human ISCs maintained stem cell function, providing a platform to investigate stem cell potential following hypoxia.

To determine if ISC monolayer cultures exposed to hypoxia would respond in a baseline predictable way, ISC monolayers were exposed to hypoxia and expression of known HIF-target genes was assessed. Off-chip gas mixtures were adjusted to achieve an oxygen concentration of <1% (below 10 μM), which is considered severely hypoxic but not anoxic.[389] Real-time oxygen levels at the cell-media interface were measured inside each device for the duration of the 24-hour experiment (**Fig. 4.2D inset**). The data show the MPS produced a rapid hypoxic environment of 0.3% Oxygen (3 μM) within ~30 minutes, which was maintained during the 24-hour experiment (**Fig. 4.2D**). Interestingly, when ISC monolayers were cultured in normoxic conditions as a control, cellular respiration reduced oxygen levels from 18% (180 μM) to 3.5% (35 μM) in the MPS indicating physiologic oxygen levels for ISCs in culture is 5-fold less that atmospheric oxygen levels. Total mRNA was collected after 24-hours of hypoxia and expression of HIF1A and HIF-target genes; vascular endothelial growth factor (VEGF)[362], solute carrier family 2 member

1 (SLC2A1 or GLUT1)[363] and BCL2 (B-cell lymphoma 2) interacting protein 3 (BNIP3)[364] were quantified. As expected HIF1A demonstrated little transcriptional change since its activity is mediated by post-transcriptional stabilization[365, 366], however, HIF1A target genes were significantly upregulated compared to normoxic controls (**Fig. 4.2E**). Overall, our results show the MPS produces reproducible ISC culture replicates, generates a rapid and sustained hypoxic environment for prolonged periods, and demonstrates that an oxygen tension of 0.3% (3 μM) is sufficient to activate a canonical hypoxia response inside primary human ISCs.

24hrs of hypoxia causes increased proliferation and reduced ISC activity that recovers at 48hrs of hypoxia

A pressing question is whether human ISCs can tolerate hypoxic events for long periods of ischemia, which may be a feature of chronic inflammation in ISC microenvironments or organ harvest and pre-transplantation storage.[149, 204] We addressed this question by first exposing ISC monolayers in the MPS to 24 hours of hypoxia (<1% oxygen), and then quantified ISC proliferation and functional properties by single-cell organoid forming potential. Following 24 hours of culture in either a normoxic or a hypoxic MPS, qualitatively, there was little appreciable difference in the number of proliferating cells in the hypoxic MPS (**Fig. 4.3A**), however, a more careful quantitative analysis by flow cytometry demonstrated a slight but significant increase in proliferating cells after 24-hours of hypoxia (**Fig. 4.3B, C**).

To determine how longer hypoxia would impact ISC function, monolayers were exposed to 24-hours or 48-hours of hypoxia or normoxia as a control in the MPS; then monolayers were dissociated to single cells and applied to Cell Raft Arrays (CRAs) for high-throughput and accurate quantification of organoid forming potential (**Fig. 4.3D, E**). CRAs enable up to ~10,000 ISCs to

be plated in microwells on a small device and each ISC can be evaluated for organoid forming potential over time.[198] Here, we quantified the number of viable single cells and organoids derived from them by scanning the CRAs every 2 days for 6 days (**Fig. 4.3F, G**). Quantifying Organoid Forming Efficiency (OFE) at each timepoint demonstrated a significant decrease (~2.5-fold) in OFE when cells were exposed to 24-hours of hypoxia (**Fig. 4.3H**). When we performed a longer 48-hour hypoxia exposure, surprisingly there was initially a significant increase in the number of surviving early organoids at day 2, and also unexpectedly, the OFE at later timepoints was indistinguishable from normoxia controls (**Fig. 4.3I**). These data indicate that ISC proliferation after 24-hours of severe hypoxia (<1% oxygen) is not substantially impaired and suggest there are hypoxia-regulated mechanisms that are enhancing ISC survival and preserving ISC function in a time-dependent manner.

Hypoxia duration reveals early, mid, and late transcriptional responses

To further explore the extent to which ISCs can tolerate severe hypoxia, we exposed ISCs in the MPS to short, intermediate, and long-term hypoxia and evaluated the first onset of apoptosis by Annexin V single cell immunocytofluorescence (**Fig. 4.4A**).[390] Flow cytometric quantification of single cells demonstrates ~90% of the cells survive through 48 hours of severe hypoxia without a statistical difference of normoxic controls. However, after 72 hours of severe hypoxia, there was a significant loss of viability, which was reduced to about half that of normoxic controls cultured for the same duration. These data indicate the ISC viability is highly refractory to severe hypoxia through 48 hours, and these results also define boundaries where ISCs in MPS can be investigated for transcriptomic changes in live cells during short and long-term hypoxia.

Organoid forming assays indicated intermediate hypoxia durations reduced ISC function that rebounded after 48 hours of hypoxia suggesting ISCs were engaging transcriptomic programs to enhance survival and preserve ISC function during a hypoxic event. Consistent with OFE assays, which demonstrated ISC rebound at later hypoxia time points, ISC biomarker, OLFM4, demonstrated a marked decrease in expression after 6-hours of hypoxia that rebounded to nearly normoxic control levels after 48 hours (**Fig. 4.4B**). In contrast, VEGFA, a hallmark target gene of HIF1□, demonstrated an early (6-hour) increase in expression over normoxic controls followed by down-regulation, as compared to the 6-hour hypoxic condition, at both 24- and 48-hours of hypoxia. VEGFA remained significantly higher in hypoxic samples at each time point than normoxic samples, as expected by the known influence of hypoxia on increasing the angiogenic pathway. Together, with results from functional stem cell assays, these data indicate ISCs experience dynamic gene expression changes from the onset of hypoxia through extended hypoxic states and suggest hypoxia-dependent transcription factors initiate early gene expression programs that re-establish a functional physiologic ISC state.

To more comprehensively investigate these time-dependent gene expression changes, we performed whole transcriptomic analysis on ISC cultured on the MPS under severe hypoxia for 6-, 24-, and 48-hours. One challenging feature of microdevices is the small number of cells inherent to the micro-platform. To address this, we employed a new automated microfluidic platform that generates RNAseq libraries from as low as 1.0 ng of total RNA (Fluidigm Juno^{TM} System). The data demonstrate robust depth and high reproducibility between technical replicates (n = 3) for each timepoint and also reveal global transcriptomic changes in ISCs between normoxic and hypoxic samples (**Fig. 4.4C**). Bulk RNA-sequencing samples were sequenced from an incredible range of between 39 to 93 million reads. Interestingly, gene expression analysis shows an increase

in the number of differentially regulated genes over time (**Fig. 4.4D**), and many of these genes are uniquely regulated during early, intermediate, and long-term hypoxia (**Fig. 4.4E**). Pathway Analysis of genes uniquely regulated at each timepoint indicates a predicted early (6-hour) transcriptional response to hypoxia and oxygen levels (**Fig. B.3**). Interestingly, mid (24-hour) and late (48-hour) transcriptional responses shift to pathways that regulate cell death and apoptosis (**Fig. B.3**). These data are consistent with empirical evidence demonstrating no increase in numbers of apoptotic cells through 48-hours of severe hypoxia and suggest global genetic responses are engaged to preserve viability.

K-means clustering was then performed on the data to identify key genes activated or repressed by hypoxia during early, mid, and late transcriptional responses in ISCs. To minimize the influence of experimental noise on our interpretation, gene read counts were normalized to a z-score, then 20 clusters of genes were identified with different patterns. This was accomplished by identifying gene clusters in which expression did not change across all 3 normoxic time points, and by contrast, did change during different lengths of hypoxia exposure. These analyses revealed the identification of 4 different gene patterns that were either induced or reduced by hypoxia relative to normoxic conditions (**Fig. 4.4F**). Three of these categories are characterized by gene cohorts that were uniquely upregulated at different timepoints we termed Early, Mid, and Late responders. Early responders were significantly upregulated after 6 hours, 24 hours, and 48 hours of hypoxia. Late responders were upregulated only after long-term hypoxia. Interestingly, Mid responders showed both upregulated and downregulated expression patterns following 24- and 48-hours of hypoxia. The downregulated gene set of Mid responders exists without subsequent regulation in the normoxic, time-matched controls, showing that hypoxia duration was indeed the

cause of significant gene downregulation. Moreover, Pathway Analysis of genes shows distinct downregulation of pathways that regulate DNA replication and rRNA process (**Fig. B.3**).

Hypoxia primes transcriptional state to respond to inflammatory mediators

Interestingly, within this subset of 4 gene expression patterns there was noticeable enrichment of the interleukin (IL) receptors, particularly in the gene groups that demonstrated hypoxia-dependent upregulation. Following early, intermediate, and long-term hypoxia, expression patterns of differentially expressed IL receptors were significant upregulated, as compared to time-matched normoxia expression (**Fig. 4.4G-O**). Firstly, IL17RB could be categorized as a hypoxia non-responder as it demonstrated control level-expression throughout all hypoxic durations and only increased expression at late-stage normoxia (**Fig. 4.4G**). Of particular note, IL6R, IL10RB, IL11RA and IL22RA1 demonstrated profound and consistent hypoxia-dependent upregulation in MPS that persisted from early- to late-stage hypoxia exposure (**Fig. 4.4H-K**). Other interleukin receptors demonstrated transient temporal upregulation unique to one of the three hypoxic durations. IL1R2 could be classified as an early-transient responder as it increased early during hypoxia exposure but normalized to control levels during mid- to late-hypoxia durations (**Fig. 4.4L**). IL2G was a transient Mid responder, and IL17RA and IL17RC were unique in that they demonstrated mid-responder characteristics but exhibited over-all downregulation through late-term hypoxia (**Fig. 4.4M-O**). These results highlight key temporal changes in intestinal MPS during a hypoxic event, and interestingly point to the potential priming of ISCs to respond to interleukins secreted into the microenvironment during different times of hypoxia or later from blood circulation post-reperfusion, as previously reported in a human intestinal IR model.[53]

4.4. Discussion

For a discussion of hypoxia in the small intestine, it is important to state that physiologic *in vivo* pO_2 levels inside the small intestine have been reported to be between 30 and 77 mmHg (3.9 to 10% O_2).[204, 205, 391] There is a steep oxygen gradient inside the intestinal lumen, from the vascularized submucosa to the anaerobic zone.[11] Moreover, ingestion of nutrients (glucose) causes the intestinal submucosa to undergo absorptive hyperemia, metabolically demanding more than 200% of the total cardiac output to supply blood to the superior mesenteric artery for intestinal oxygen extraction.[314, 392] Although capillary recruitment increases as chyme passes through each region the intestine, absorptive hyperemia cannot prevent a drop of at least 10 mmHg (1.32% O_2) in oxygen tension during digestion.[150] Keeping all this variation in physiologic oxygen in mind, a pathophysiologic intestinal oxygen (hypoxic) concentration can be defined for any magnitude of oxygen below 3% that activates cellular hypoxic response. For the purpose of *in vitro* human intestinal epithelial studies, we defined severe hypoxia as local oxygen tension below 10 μM (1% O_2).

Certain durations and magnitudes of hypoxia in *in vitro* culture systems have been shown to either promote or repress pluripotency and self-renewal of other stem cell populations. 'Physiologic hypoxia' is a state where cells in an anatomical niche experience lower oxygen than other regions but persist in a tissue. Stem cells isolated from other organs have shown distinct responses to different magnitudes of hypoxia. For example, human cardiac stem cells display increased proliferation when cultured inside specialized physiologic hypoxia (5% oxygen) incubators for 24 hours but increased quiescence, as evident from reduced β-galactosidase activity, p16 protein expression, and mitochondrial content when cultured in severe hypoxic (0.5% oxygen) chambers.[393] In another study of hepatic stem cells, stemness was promoted in liver physiologic

hypoxia (10% oxygen), as evident from increased expression of specific liver stem cell markers CK19, Sox9, EpCAM, and Lgr5 via immunofluorescence and Western blot analysis and single-cell colony-forming assay, but repressed by severe hypoxia when cultured in a 1% oxygen environment.[394] Both studies show that physiologic hypoxia cultures, specific to each organ system, support stemness in stem cells.

Most recently, colonic epithelial stem cells cultured (in an air-liquid interface) on Transwell membranes inside a hypoxic (2%) incubator for 21 days remained undifferentiated, with more CD44+ (undifferentiated) cells and less $UEA1^+$ (goblet) cells than colonic epithelial cells cultured in a normobaric incubator.[374] Although it is known that a hyperoxic environment (21% oxygen) often disrupts stem cell culture[395, 396], the lower limit of oxygen necessary to maintain stemness has not been defined for human intestinal epithelial stem cells. We found that ISC cultured in severe hypoxia for at least 24 hours were still able to differentiate into mature enterocytes.

In addition to demonstrating how physiologic hypoxia and severe hypoxic cultures impact ISC function, there findings are also relevant to clinical situations where low oxygen is presented in an intestinal injury. Specific windows of time in which ischemic tissue is under low oxygen tension, or more likely severely hypoxic, are necessary to determine whether or not to explant tissues and isolate ISCs for further expansion and later repair. Our results indicate that ISC function can be sustained following up to 48 hours of severe hypoxia, but 72 hours of hypoxia reduces ISC viability. Jejunal segments of tissue cannot be collected during routine biopsies or elective surgeries due to their location in the middle region of the small intestine. Moreover, ischemic injury cannot be decoupled from reperfusion injury following the removal of mesenteric surgical clamps, as blood flow returns oxygen back to the injury site and damaging reactive oxygen species

initiate a cascade of inflammation.[50] Although inaccessible, the jejunum represents the segment of the small bowel most susceptible to vascular injuries, as it contains longer villi, where large networks of capillaries reside, than either the duodenum or the ileum. Using primary ISCs isolated from human jejunal tissue, we were able to investigate the impact of hypoxia, a consequence of ischemic injury, on ISC function in isolation.

We found that human ISCs cultured under severe hypoxia upregulate downstream targets of HIF1A, as compared to human ISCs cultured in normoxia. This means the intestinal MPS could facilitate HIF1A activation in primary intestinal epithelium and provide a microenvironment to sustain severe hypoxia for at least 72 hours. Following 24 hours of hypoxia, the intestinal epithelium presented a slight but significant increase in cell proliferation. Once removed from MPS, dissociated to single cells, and reintroduced to normoxia in 3D Matrigel culture, ISCs displayed a subsequent decrease in organoid formation, as compared to normoxic ISCs. Therefore, reoxygenation decreased ISC survival, as compared to normoxic ISCs that had higher organoid formation. In contrast, after 48 hours of hypoxia, ISCs created more organoids than normoxic ISCs. This finding shows an extended period of hypoxia may be required for ISCs to adapt and perhaps better survive reoxygenation. This is supported by the bulk RNA sequencing and pathway analysis, which shows at 48 hours of hypoxia the top pathways are related to metabolism and responses to hypoxia and oxygen levels, whereas at 24 hours the top two pathways are for regulation of cell death and apoptosis.

Apart from pathway analysis, bulk sequencing provided identification of specific upregulated genes following 3 different periods of hypoxia. Interestingly, interleukin receptors were among the top upregulated genes following hypoxia, as compared to normoxic time-matched controls. Of note, IL22RA1 was significantly upregulated at all 3 hypoxic periods, with the highest

fold change after the early 6-hour period. IL10RB and IL6R were among the genes significantly upregulated after 6-hour hypoxia and 24-hour hypoxia, respectively. IL6 has been shown to inhibit enterocyte cell death in vivo following ischemia reperfusion injury in the murine small bowel.[397] In a mouse crypt organoid model, exogenous IL6 was shown to promote crypt organoid proliferation and increase stem cell numbers.[398] In a more recent mouse model, endogenous IL6 was shown to be needed to mitigate epithelial injury following focal irradiation.[399] These studies suggest IL6 can rescue enterocytes following ischemic and irradiation injuries, but the impact of IL6 on hypoxic ISCs remains to be seen. Future studies using the intestinal MPS in combination with IL6 treatment and hypoxia exposure could show both ISC proliferation and organoid survival.

MPS built to study cellular responses to controlled environmental factors offer many advantages over standard tissue culture plates and bulky incubators. Our intestinal MPS with integrated oxygen sensors provides real-time tracking of oxygen levels at the cell-media interface. As we learn more about how oxygen impacts stem cell fate, the potential to change culture conditions to meet the needs of a stem cell in the particular cell cycle or differentiation phase can be realized. Here, we provide a novel system to measure and adjust oxygen concentrations at the 3D cell-scaffold interface. We found that primary human intestinal epithelial stem cells respond to low levels of oxygen by increasing proliferation and some important markers of stemness, but there were also signs of increased inflammatory cytokine markers which should be further investigated. *In vitro*, hypoxia initiates a cascade of interleukin receptor activation in human ISC, potentially influencing epithelial responses to immune cell signals during hypoxia and future immune responses after reperfusion. The addition of important immune cell types, such as leukocytes and innate lymphoid cells, into our intestinal MPS would be beneficial to discovering

the mechanisms underlying the cascade of inflammation following intestinal ischemia. Moreover, we aim to develop similar platforms to investigate other primary stem cells and optimize oxygen culture conditions across many organ tissues.

4.5. Materials and methods

Primary human crypt isolation and intestinal epithelial stem cell culture. A surgical specimen of human small intestine (jejunum) was obtained from a donor at UNC Hospitals with consent of the patient (under the approved protocol UNC IRB #14- 2013). Villi and crypts were detached from the specimen by incubation in a chelating buffer for 75 min at 20°C followed by vigorous shaking in a 50 mL conical tube. The chelating buffer was composed of EDTA (2 mM), dithiothreitol (DTT, 0.5 mM, freshly added), Na_2HPO_4 (5.6 mM), KH_2PO_4 (8.0 mM), NaCl (96.2 mM), KCl (1.6 mM), sucrose (43.4 mM), D-sorbitol (54.9 mM), pH 1⁄4 7.4.[400] Released crypts were expanded as a monolayer on a neutralized collagen hydrogel as described previously.[60] Briefly, crypts were placed on the top of 1.0 mg/mL collagen hydrogels (1 ml into each well of 6-well plate (T1006; Denville, Holliston, MA)) at a density of 5,000 crypts/ well and overlaid with 4 ml of Expansion Media (EM) containing 10 mmol/L Y-27632 (S1049; SelleckChem). EM contains a mixture of advanced Dulbecco's modified Eagle medium/F12 medium (12634010; ThermoFisher) and Wnt-3A, R-spondin 3, noggin (WRN) conditioned medium (WRN medium prepared in lab from L-WRN cells (CRL- 3276; ATCC) following a published protocol[401] at a volumetric ratio of 1:1, and supplemented with GlutaMAX (35050061; ThermoFisher), B27 supplement without vitamin A (12587010; ThermoFisher), 10 mM HEPES (15630-080; ThermoFisher), 1.25 mM N-acetyl cysteine (194603; MP Bio, Santa Ana, CA), 10 mM nicotinamide (N0636; Sigma-Aldrich), 50 ng/mL epidermal growth factor (315-09; Peprotech),

2.0 nM gastrin (AS-64149; Anaspec), 10 nM prostaglandin E2 (14010; Cayman Chemicals), 3.0 μM SB202190 (S1077; Selleckchem), 100 U/mL penicillin-streptomycin (15140122; ThermoFisher), and 50 mg/mL primocin (ant-pm-1; InvivoGen, San Diego, CA). EM was used to expand the epithelial cell numbers as monolayers or organoids. Y-27632 was present only in the first 48 hours of cell culture and was not added to subsequent media changes. The medium was changed every 48 hours. When the cell coverage was greater than 80% (typically 5 to 7 days), the epithelium was dissociated to fragments to seed onto the intestinal MPS.

Fabrication of primary human intestinal microphysiological system (MPS). The human intestinal MPS was fabricated from materials polymethyl methacrylate (PMMA) and photopolymer resin (Formlabs, Inc.). PMMA provided an optically transparent material with a low oxygen diffusion coefficient that could be sterilized and reused.[402] The photopolymer resin provided a 3D printable bottom frame to support the PMMA device and simultaneously house the optical reader oxygen measurements. The cell culture chamber and gas exchange channels were fabricated from 5.8 mm and 1.5 mm-thick polymethyl methacrylate (PMMA) sheets (44352, 44292; US Plastics). The microfluidic culture region was composed of 5 rectangular wells, with dimensions of 11.6 mm by 7.0 mm each. The rectangular gas channel on top of the wells was 70 mm by 45 mm by 1.5 mm. The bottom and top pieces of PMMA were laser cut from a 1.5 mm-thick PMMA sheet, while the middle piece, for the cell culture wells, was laser cut from a 5.8 mm-thick PMMA sheet. Briefly, to remove dust and burr material with minimal cracking, each PMMA surface was quickly wiped with 100% IPA solution and air-dried. All 3 pieces were pressed together between two sheets of brass using a pneumatic heat press (SwingPress 10-0403; Across International). Annealing was performed with the heat press set at 100°C and 300 psi for 2 hours,

then the bonded device was cooled for 3 hours at room temperature. A rubber gasket was laser cut and placed on top of the PMMA layer to seal the device, prior to bolting together. The device was tested for leaks using red and blue dyed water and cracks were sealed by application of dichloromethane to the seams. A neutralized collagen hydrogel (2.0 mg/ml) was cast into each well of a prefabricated PMMA device and allowed to polymerize at 37°C for 1 hour. 250 μL of 1X DPBS was overlaid on the polymerized hydrogel and allowed to pre-swell for at least 5 hours at room temperature. DPBS was removed and the hydrogel was rinsed three times before overlaying with 250 μL of EM containing ISCs that had been mechanically dissociated by pipetting 10 times until cells were ~1-10 cell-clumps. Once the ISCs formed a confluent monolayer, an integrated phosphorescent oxygen sensor (iPOB) was added to the epithelium to measure oxygen.

Real-time monitoring and control of oxygen concentration in 3D culture. Oxygen concentration in the system was continuously measured with an integrated phosphorescent oxygen sensor (iPOB) using Near Infrared (NIR) phosphorescence lifetime fluorimetry. The iPOB is composed of porous poly(2-hydroxyethyl methacrylate) (pHEMA) gel functionalized with palladium-benzoporphyrin derivatives (Pd-BPD) that respond to local oxygen concentrations via phosphorescence quenching.[332] The iPOB (Profusa, Inc., San Francisco, CA) has been manufactured in a variety of sizes, but for all experiments a disk-shaped, 5 mm diameter and 0.5 mm thickness, iPOB was used. The optics front-end of the NIR phosphorescence lifetime fluoroscope (Profusa, Inc., San Francisco, CA) was inserted into the support frame below the MPS. The oxygen concentration was controlled via a PMMA gas-mixing microfluidic chip with tubing connecting outlets from the gas-mixing chip to the inlets of each MPS. The gas-mixing chip was

previously used to generate 8 concentrations of mixed gas, ranging from less than 3 μM of oxygen to 180 μM.(**Fig. B.1**)[378] Gas flow to the gas-mixing chip was regulated using an air flow control valve (62005K313; McMaster-Carr) and monitored with a mass flow meter with digital output (GFMS-010061; Aalborg GFM). Hydrated mixed gas exiting the gas-mixing chip was introduced into individual MPS at a rate of 5 mL/min to prevent media evaporation. Within 30 minutes, the gas mixture equilibrated with the local MPS environment to generate the desired oxygen concentration at the hydrogel surface-media interface where oxygen was measured using the iPOB (**Fig. 1D**). The intestinal epithelium inside MPS was cultured in environments made from mixed gases and compared to intestinal epithelium statically cultured in a normobaric incubator with an oxygen environment of 186 μM.

Immunocytochemistry. To assess the impact of various durations and magnitudes of hypoxia on ISC proliferation, primary human intestinal epithelium and single cells isolated from each MPS chamber were stained for Ki-67. For Ki-67 staining of intestinal epithelium following hypoxia, the intestinal MPS was opened and media was removed from each chamber. Intestinal epithelium on top of the collagen hydrogels were fixed with 4% PFA for 15 minutes. After fixation, samples were rinsed once with 1X PBS and overlaid with PBS. Samples were permeabilized for 15 minutes with 0.5% Triton-X 100 in 1X PBS. Samples were blocked for 30 minutes with a 3% BSA solution. After blocking, samples were stained for proliferation marker Ki-67 Alexa Fluor 647 (1:250 dilution in 3% BSA, Cat. No. 652407; BioLegend) for 1 hour and nuclei counterstain bisbenzimide (1:1000 dilution in 1X PBS, Cat. No. 1155; Millipore Sigma) for 5 minutes at room temperature. To look at cell-cell contacts, tight junction protein occludin (Cat. No. 13409-1-AP; Proteintech) was added for 1 hour, followed by incubator with the secondary antibody Cy3 (Cat.

No. C2306; Sigma) for 2 hours. After staining, the gels were overlaid with 1X PBS and stored at 4°C until imaging. All samples were imaged with an Olympus (Waltham, MA) IX81 microscope, using Metamorph Basic (Molecular Devices, San Jose, CA) software, and image analysis was performed with ImageJ.[336]

Organoid forming efficiency (OFE) assay and Fluorescence-activated cell sorting (FACS) of live cells. Following MPS culture, human intestinal epithelium was dissociated into single cells, sorted using a flow cytometer, and suspended in Matrigel® on a quad Cell Raft Array (CRA) platform (Cell Microsystems, Durham, NC).[198] Briefly, each sample was retrieved and placed in a separate conical. 500 U/mL Collagenase IV (17104019; Gibco) was added to breakdown the scaffold and incubated for 10 minutes at 37ºC. After centrifugation, the cell pellet was rinsed twice in DPBS and re-suspended in 150 µL of 0.5 mmol/L EDTA in DPBS with 10 mmol/L Y-27632 and incubated for 5 minutes at 37ºC. The fragments were further dispersed by triturating 30 times using a 200 µL pipet tip. After centrifugation, the cell pellet was re-suspended in 500 µL TrypLE Express (12605-036; Gibco) with 10 mmol/L Y-27632 and incubated for 5 minutes at 37°C. The cell suspension was gently triturated 7 times using a 28.5-gauge insulin needle to further dissociate. 500 µL of EM was added to quench the reaction, and cells were pelleted and rinsed once in EM. After pelleting again, cells were re-suspended in 200 µL of EM containing 1% FBS. Immediately before FACS, APC Annexin V (1:200, 640941; Biolegend) was added to cells for live/dead discrimination. After staining, cells were rinsed in EM and filtered through 0.4 µm FACS tube top filter (352235; Corning). 5,000 Annexin V- live cells were isolated via FACS and re-suspended in 250 µL of Growth Factor Reduced Matrigel® (354230; Corning). Cell-gel suspensions were plated in each chamber of the quad CRA. To cover the CRA, each array

was centrifuged at 200 x g for 5 minutes. CRAs were polymerized for 20 minutes at 37°C in an incubator and then overlaid with EM containing 10 mmol/L Y-27632. Media was replaced every 2 days. To determine OFE, the CRA was scanned, and the total number of organoids was counted on day 2, day 4, and day 6. The OFE (%) was calculated as the total number of organoids created in one CRA chamber, divided by 5,000 cells and multiplied by 100. FACS and flow cytometry were performed using a SH800Z Cell Sorter (Sony Biotechnology, San Jose, CA).

Flow cytometry. Cells collected from normoxic and hypoxic MPS were dissociated following the protocol above up to the step of addition of TrypLE Express. Following trituration with the insulin needle and quenching with the EM, cells were pelleted and re-suspended in 100 µL of 1X DPBS. Approximately 50,000 cells from each chamber were fixed by adding 400 µL of 4% PFA solution while being constantly vortexed to prevent cell aggregation. After fixation, single cells were pelleted and re-suspended in 0.3% Triton-X for 15 minutes to permeabilize the cell membrane. Single cells were pelleted and re-suspended in a staining solution of DMEM containing 1% FBS and anti-Ki-67 Alex Fluor 647 (1:250 dilution in 3% BSA, Cat. No. 652407; BioLegend) for 1 hour on ice. After staining, cells were rinsed in PBS and filtered through 0.4 µm FACS tube top filter (352235; Corning). Ki-67-positive single cells were quantified by flow cytometry.

qRT-PCR. To assess the expression of genes that are responsive to hypoxia, human intestinal epithelial samples from each MPS were collected for qRT-PCR analysis. Briefly, cells attached to collagen hydrogels were lysed in 200 µL of RNA Lysis buffer (AM1931; ThermoFisher). Total RNA was extracted using RNAqueous-Micro Total RNA Isolation Kit (AM1931; ThermoFisher) according to manufacturer's protocols. cDNA was generated from ~2

ng of total RNA from each sample using iScript Reverse Transcription Supermix for qRT-PCR (170-8891; BioRad) according to manufacturer's protocols. cDNA was diluted 1:20 and 1 μL was used for qRT-PCR using Taqman probes (Applied Biosystems) (**Table 4.1**) and SsoAdvanced Universal Probes Supermix (1725281; BioRad) according to manufacturer's protocols. qRT-PCR was carried out in a StepOnePlus Real Time PCR System (Applied Biosystems). For each sample and experiment, triplicates were made and normalized to 18S mRNA levels. Fold change was expressed relative to normoxic controls using ΔΔCT analysis.[337] All statistics for gene expression were generated using a Student's t-test. In all statistical analysis, $p < 0.05$ was considered significant.

RNA-sequencing. To investigate the dynamic response of ISC to hypoxia at the whole transcriptomic level, we performed RNA-seq on human intestinal epithelium exposed to 6 hr, 24 hr or 48 hr of hypoxia inside intestinal MPS, along with normoxic control intestinal MPS which were cultured for each respective time point with no hypoxia exposure. RNA samples were collected from each intestinal MPS and Total RNA was extracted using RNAqueous-Micro Total RNA Isolation Kit (AM1931; ThermoFisher) according to manufacturer's protocols and stored at −80°C. To assess RNA quality prior to submission for sequencing, an RNA integrity number (RIN) was measured using the Agilent 2100 Bioanalyzer. After confirmation that each sample had a RIN of at least 8, integrated fluidic circuits (IFCs) for gene expression and genotyping analysis were prepared using the Advanta™ RNA-Seq NGS Library Prep Kit for the Fluidigm Juno™ and sequenced with the Fluidigm Biomark™ HD system.

Gene level expression was obtained through pseudo alignment of reads to human genome GRCh38 using Kallisto.[403] Principal component and sample correlation analysis were done with

Bioconductor packages Biobase, cluster and qvalue.[404] Expression values for plotting were obtained by TMM normalization across all samples using EdgeR package and differential expression between groups was calculated from raw pseudo counts with DESeq2.[405, 406] AmiGO[407] was used to initially visualize the ontologies for each time point and the Database for Annotation, Visualization and Integrated Discovery (DAVID)[408, 409] provided gene ontology enrichment analysis for bioprocess pathway analyses on the 2000 most significantly upregulated genes for each time point, where an adjusted *P* value was computed using the Benjamini-Hochberg method (**Table 4.2**).

4.6. Author Contributions

K.R.R. designed the study and conducted the experiments, analyzed data, and wrote the manuscript. M.J.C. conducted experiments and analyzed RNA sequencing results. V.A.P. worked with K.R.R. to build and integrate all components of the microphysiological systems. M.Y. designed, fabricated, and validated the gas mixing chip using COMSOL Multiphysics and experimental methods. M.D. and S.T.M. conceived the study and wrote the manuscript.

4.7. Acknowledgements

The authors would like to thank all the members of the Magness Laboratory and the Biointerface Laboratory, along with Drs. Michael Gamcsik and Bailey Zwarycz for helpful discussions. The authors thank the Center for Gastrointestinal Biology and Disease (CGIBD) and the CGIBD's Advanced Analytics Core under NIH grant P30 DK034987. This work was done in collaboration with the National Science Foundation (EEC1160483) through a NSF Nanosystems Engineering Research Center (NERC) for Advanced Self-Powered Systems of Integrated Sensors and Technologies (ASSIST). K.R.R. was supported by the National Institutes

of Health under award number F31DK118859-02, the 2019 Howard Hughes Medical Institute Gilliam Fellowship Award, R01DK109559 (S.T.M.), and CGIBD Pilot & Feasibility Award P30 DK034987 (M.D./S.T.M.).

Conflict of Interest: S.T.M. has a financial interest in Altis Biosystems, Inc., Chapel Hill, NC. The remaining authors declare no competing related financial interests or conflict of interest at the time of the conduct of this study.

Table 4.1 List of TaqMan probes for quantitative reverse-transcription polymerase chain reaction (qRT-PCR)

Gene symbol	Gene name	Life Technologies assay ID
18S	Eukaryotic 18S ribosomal RNA	Hs99999901_s1
HIF1A	Hypoxia inducible factor 1 alpha subunit	Hs00153153_m1
BNIP3	BCL2 interacting protein 3	Hs00969289_m1
SLC2A1 (GLUT1)	Solute carrier family 2 member 1	Hs00892681_m1
VEGFA	Vascular endothelial growth factor A	Hs00900055_m1
OLFM4	Olfactomedin 4	Hs00197437_m1
IL6R	Interleukin 6 Receptor	Hs01075664_m1
IL10RB	Interleukin 10 Receptor Beta	Hs00175123_m1
IL17RB	Interleukin 17 Receptor Beta	Hs00218889_m1
IL22RA1	Interleukin 22 Receptor Alpha 1	Hs00222035_m1

Table 4.2 List of Top Gene Ontology (GO) Upregulated Pathways

Full name	GO ID
steroid metabolic process	GO: 0008202
cholesterol metabolic process	GO: 0008203
response to oxygen levels	GO: 0070482
response to hypoxia	GO: 0001666
sterol metabolic process	GO: 0016125
cholesterol biosynthetic process	GO: 0006695
lipid biosynthetic process	GO: 0008610
sterol biosynthetic process	GO: 0016126
regulation of cell death	GO: 0010941
regulation of apoptotic process	GO: 0042981
regulation of programmed cell death	GO: 0043067
regulation of cell motion	GO: 0051270
intracellular signal transduction	GO: 0035556
small GTPase mediated signal transduction	GO: 0007264
regulation of cell proliferation	GO: 0042127
negative regulation of apoptotic process	GO: 0043066
negative regulation of cell death	GO: 0060548
negative regulation of programmed cell death	GO: 0043069
regulation of phosphorylation	GO: 0042325
regulation of phosphorus metabolic process	GO: 0051174
regulation of phosphate metabolic process	GO: 0019220

response to extracellular stimulus	GO: 0009991
regulation of organelle organization	GO: 0033043

Table 4.3 List of Top Gene Ontology (GO) Downregulated Pathways

Full name	GO ID
rRNA processing	GO: 0006364
cell division	GO: 0051301
mitotic nuclear division	GO: 0007067
DNA replication	GO: 0006260
sister chromatid cohesion	GO: 0007062
mitochondrial translational elongation	GO: 0070125
maturation of SSU-rRNA from tricistronic rRNA transcript (SSU-rRNA, 5.8S rRNA, LSU-rRNA)	GO: 0000462
protein localization to kinetochore	GO: 0034501
tRNA methylation	GO: 0030488
mitochondrial translational termination	GO: 0070126
DNA replication initiation	GO: 0006270
ribosomal large subunit biogenesis	GO: 0042273
mitochondrial respiratory chain complex I assembly	GO: 0032981
RNA processing	GO: 0006396
mRNA splicing, via spliceosome	GO: 0000398
cellular response to DNA damage stimulus	GO: 0006974
transcription, DNA-templated	GO: 0006351
snRNA transcription by RNA polymerase II	GO: 0042795
DNA repair	GO: 0006281

RNA methylation	GO: 0001510
doxorubicin metabolic process	GO: 0044598
daunorubicin metabolic process	GO: 0044597
cell cycle	GO: 0007049
spliceosomal tri-snRNP complex assembly	GO: 0000244

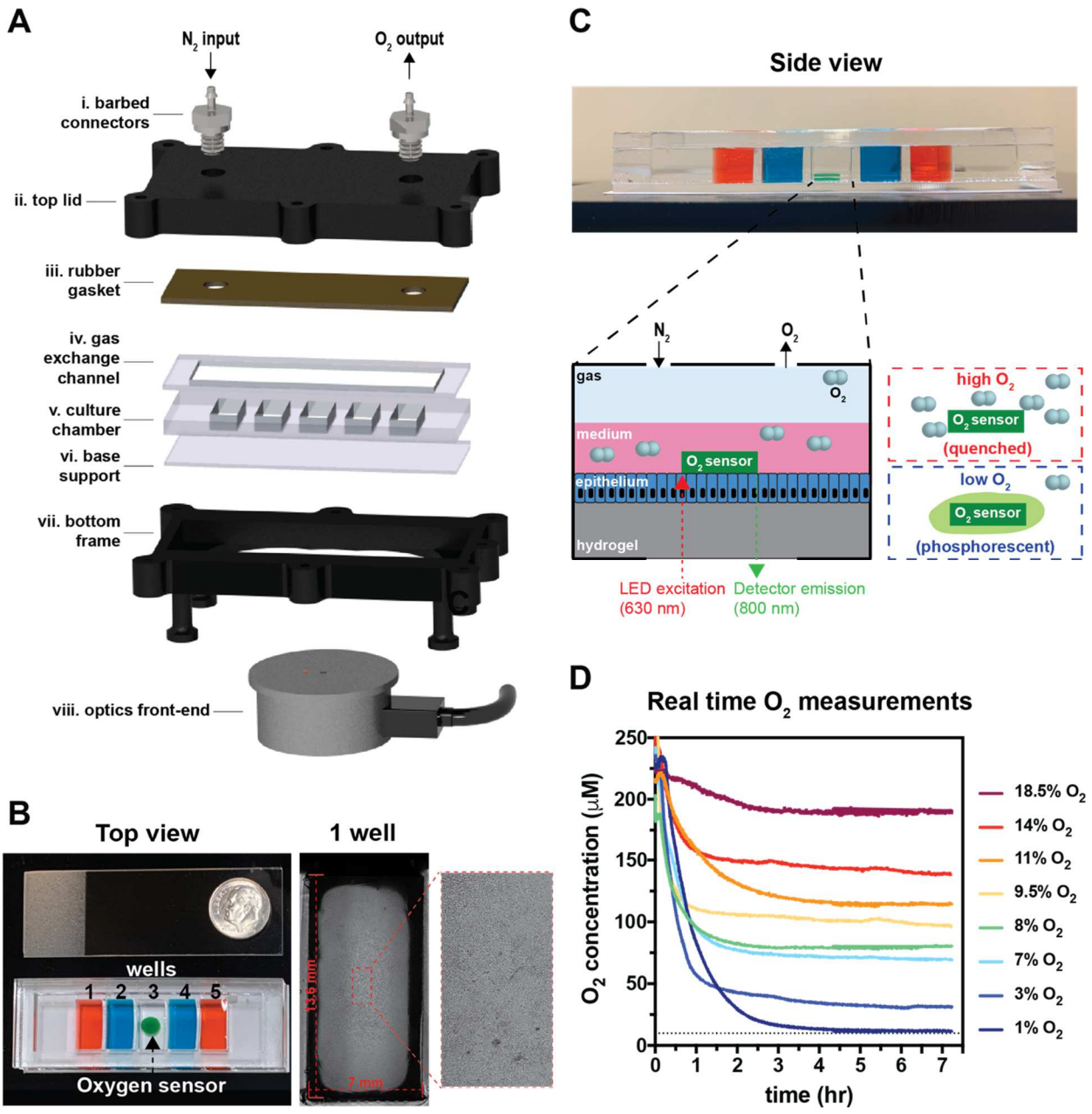

Figure 4.1 Development of a tunable hypoxia microphysiological system (MPS) with integrated oxygen sensors and primary human intestinal epithelium. (A) Schematic of exploded view of MPS compartments. (i) Barbed connectors screwed into the photopolymer resin (ii) top lid provide gas flow into and out of the device. (iii) A rubber gasket seals gas flow into and out of the Polymethyl methacrylate (PMMA) gas exchange channel. (iv) The gas exchange channel frame is

bonded to the (v) PMMA culture chamber and (vi) PMMA base support. (vii) A photopolymer resin bottom frame supports the entire PMMA device, and screws attach the top lid to the bottom frame to seal the MPS closed. (viii) The optics front-end connects via a μUSB-to-HDMI cord to a phosphorescence-lifetime fluorimeter detector and interrogates the middle culture well, where the integrated phosphorescence-based oxygen biosensor (iPOB) is located. (B) (left) Top view photograph of a standard microscope glass slide (75 x 25 mm) and dime, for reference, placed above the MPS with iPOB (black arrow) inside well 3 and red and blue dyes in wells 1 and 5 and 2 and 4, respectively. (middle) 1 well brightfield image of confluent monolayer of cells. (right) Inset from 1 well brightfield image shows magnified confluent cell monolayer. (C) (top) Side view photograph of MPS with middle well containing the green iPOB. (bottom, left) Schematic of iPOB integrated into hydrogel to measure oxygen at the cell layer inside the cell culture well. The iPOB is composed of poly(2-hydroxyethyl methacrylate) gels functionalized with palladium-benzoporphyrin derivatives (Pd-BPD). The photoluminescence excitation and detection wavelengths are 630 nm and 800 nm, respectively. (bottom, right) Schematic of porphyrin-based luminescence. In high oxygen, luminescence from the triplet state in porphyrin is quenched by energy transfer to molecular oxygen, resulting in a correlated decrease in phosphorescence lifetime. In the absence of oxygen, porphyrin molecules are excited by LED from the detector and phosphoresce with increased lifetime. (D) Plots of 8 oxygen concentration versus time (7 hours) measurements from the iPOB inside the MPS, with 8 different mixed gas inputs, show generation of 8 established oxygen environments.

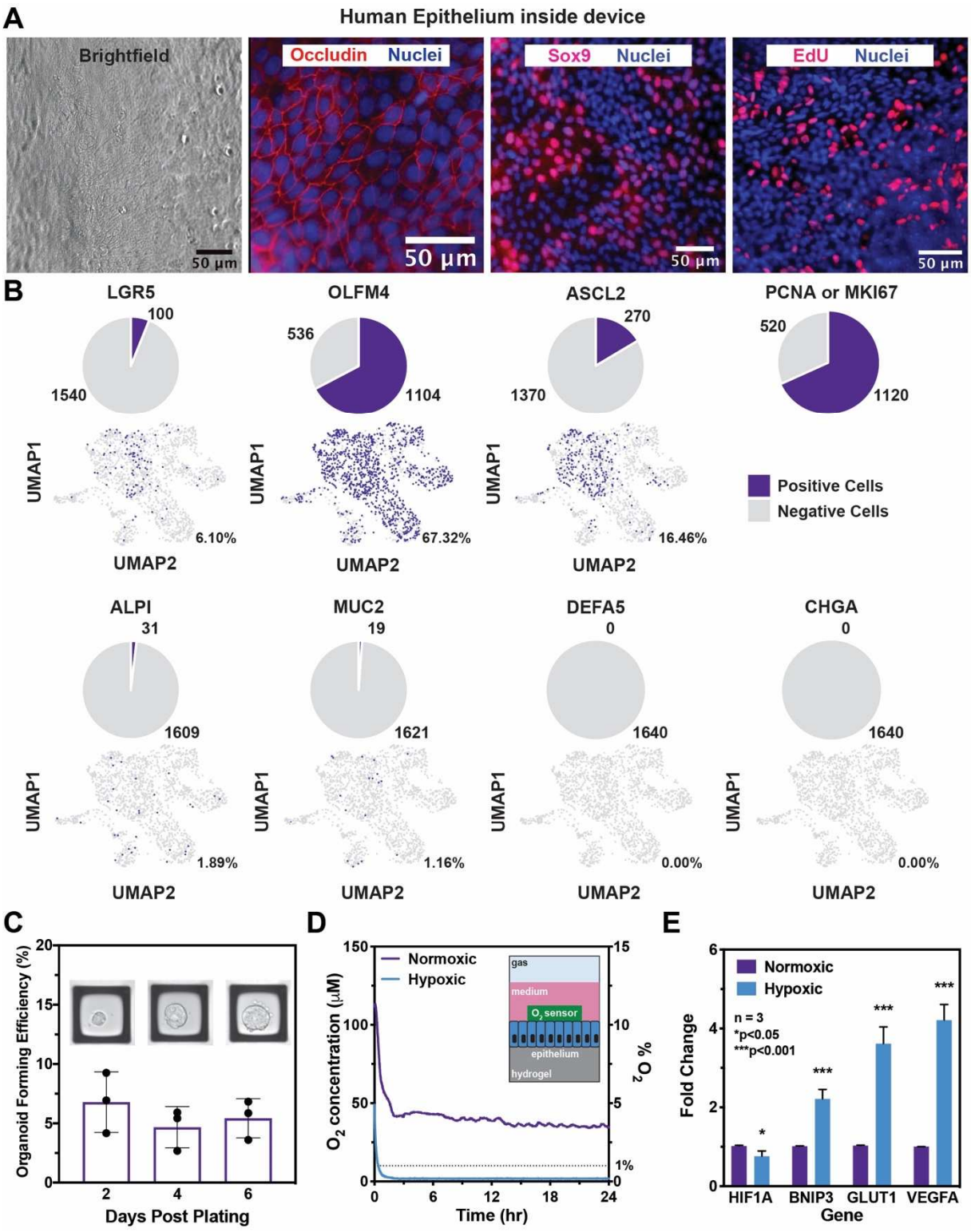

Figure 4.2 Proof of concept of hypoxic microphysiological system (MPS) with primary human intestinal epithelial stem and progenitor cells. (A) Brightfield image of human intestinal epithelial

stem and progenitor cells grown inside a MPS well to confluence. Red fluorescent images show tight junction structures between epithelial cells marked by the protein Occludin, stem cells marked by Sox9, and proliferative cells marked by EdU. In all fluorescent images, nuclei are marked by Bisbenzimide in blue. (B) (top) Single Cell RNA sequencing data of stem cell and proliferation markers shown as pie charts with number of LGR5, OLFM4, ASCL2, and PCNA or MKI67 positive cells in population of primary human epithelial cells and corresponding UMAPs. (bottom) Single cell RNA sequencing data of mature enterocyte markers ALPI, MUC2, DEFA5, and CHGA shown in pie charts and corresponding UMAPs. (C) Organoid Forming Efficiency (%) measured over 6 days from single cells isolated from MPS after 5 days in culture. (Insets) A single organoid grown inside a single well within the microarray platform and imaged on Day 2, Day 4, and Day 6. (D) Oxygen concentration tracked using the iPOB inside MPS containing the human intestinal epithelium for 24 hours with normoxic and hypoxic culture environments. (Inset) Schematic of human intestinal epithelium grown inside the MPS on top of the hydrogel scaffold. The integrated phosphorescence-based oxygen biosensor (iPOB, green) is situated within the human intestinal epithelium to measure oxygen at the cell-media interface. (E) RT-qPCR results of human intestinal epithelium for downstream HIF1A targets (BNIP3, GLUT1, VEGFA) after 24 hours of normoxia or hypoxic environment exposure. Fold Change is calculated with ΔCt, as compared to the 18S rRNA gene.

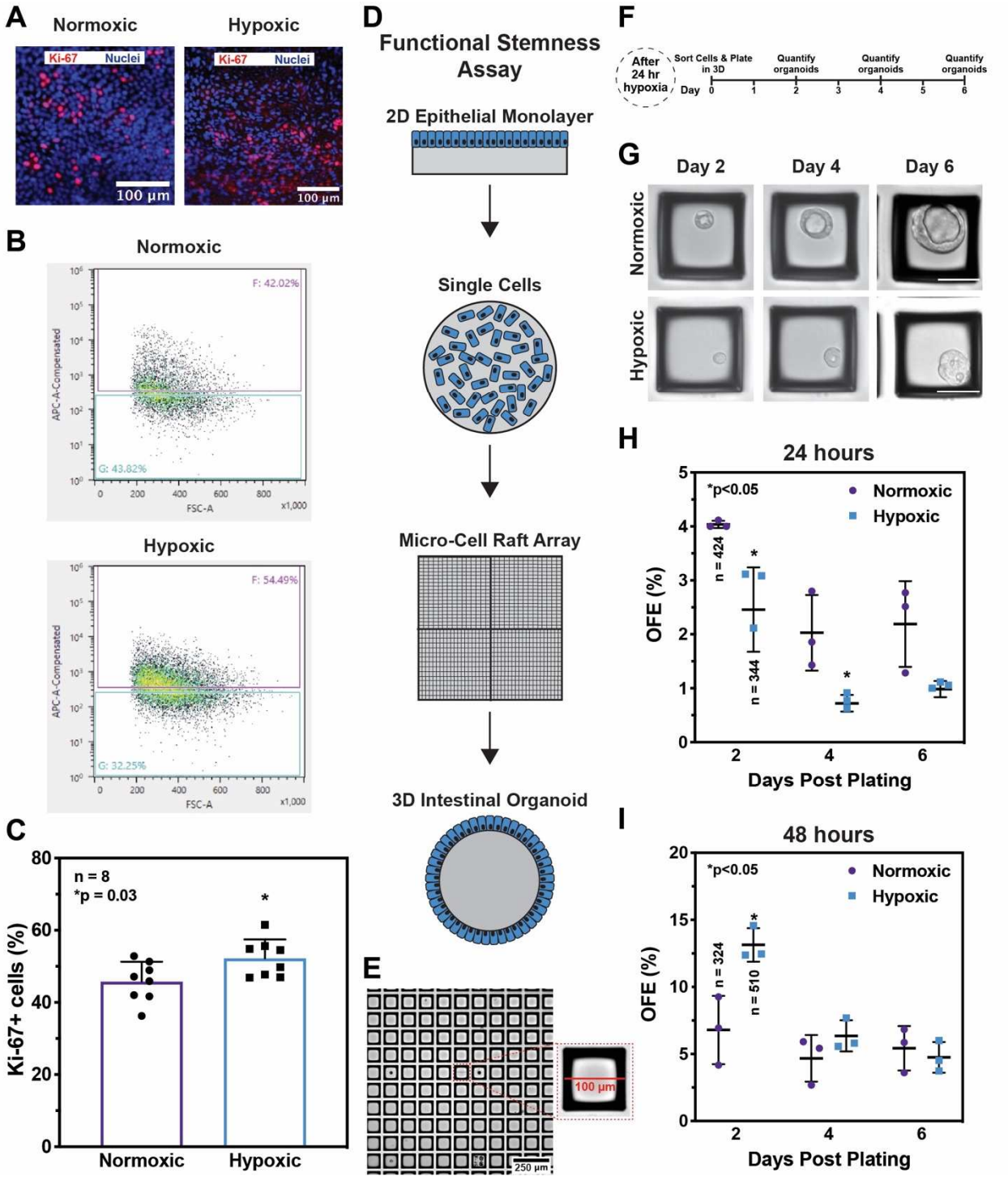

Figure 4.3 Primary human intestinal epithelium cultured under hypoxia inside microphysiological system (MPS) for 24 hours shows increased proliferative capacity, while 48 hours of hypoxia increased functional stemness. (A) Epithelium stained for Ki-67 and

bisbenzimide (nuclei) following 24 hours of normoxia or hypoxia culture inside separate MPS. (B) FACS plots from single cells dissociated from normoxic (top) and hypoxic (bottom) MPS show the population of mKi-67 APC+ cells versus the Forward Scatter Area (FSA). (C) Flow cytometry results of human intestinal epithelial single cells quantified for Ki-67 after 24 hours of culture in normoxia or hypoxia inside separate MPS. (D) Schematic of Functional Stemness Assay Steps: First, human intestinal epithelium is removed from each microphysiological system (MPS) well. Second, the hydrogel scaffold is digested to release epithelium and further dissociated to generate single cells. Third, the single live cells (Annexin V-) are isolated via Fluorescence-activated cell sorting (FACS) and seeded onto Micro-Cell Raft Arrays in 3D Matrigel. Lastly, intestinal organoids grown from single cells were imaged and quantified. (E) Image of a Micro-Cell Raft array well scanned to show grid of individual microwells. (Inset) Image of single microwell from Micro-Cell Raft array. (F) Sequential workflow for Functional Stemness Assay from each MPS cell isolation following either hypoxia or normoxia. (G) Brightfield images of tracked single intestinal organoids grown from single cells inside a microarray platform following 24 hours of normoxia or hypoxia inside separate MPS. (H) Results of Functional Stemness Assay plotted as Organoid Forming Efficiency (OFE %) for 24-hour normoxic and hypoxic samples over 6-day post plating time period. (I) Results of Functional Stemness Assay for 48-hour normoxic and hypoxic samples over 6-day post plating time period.

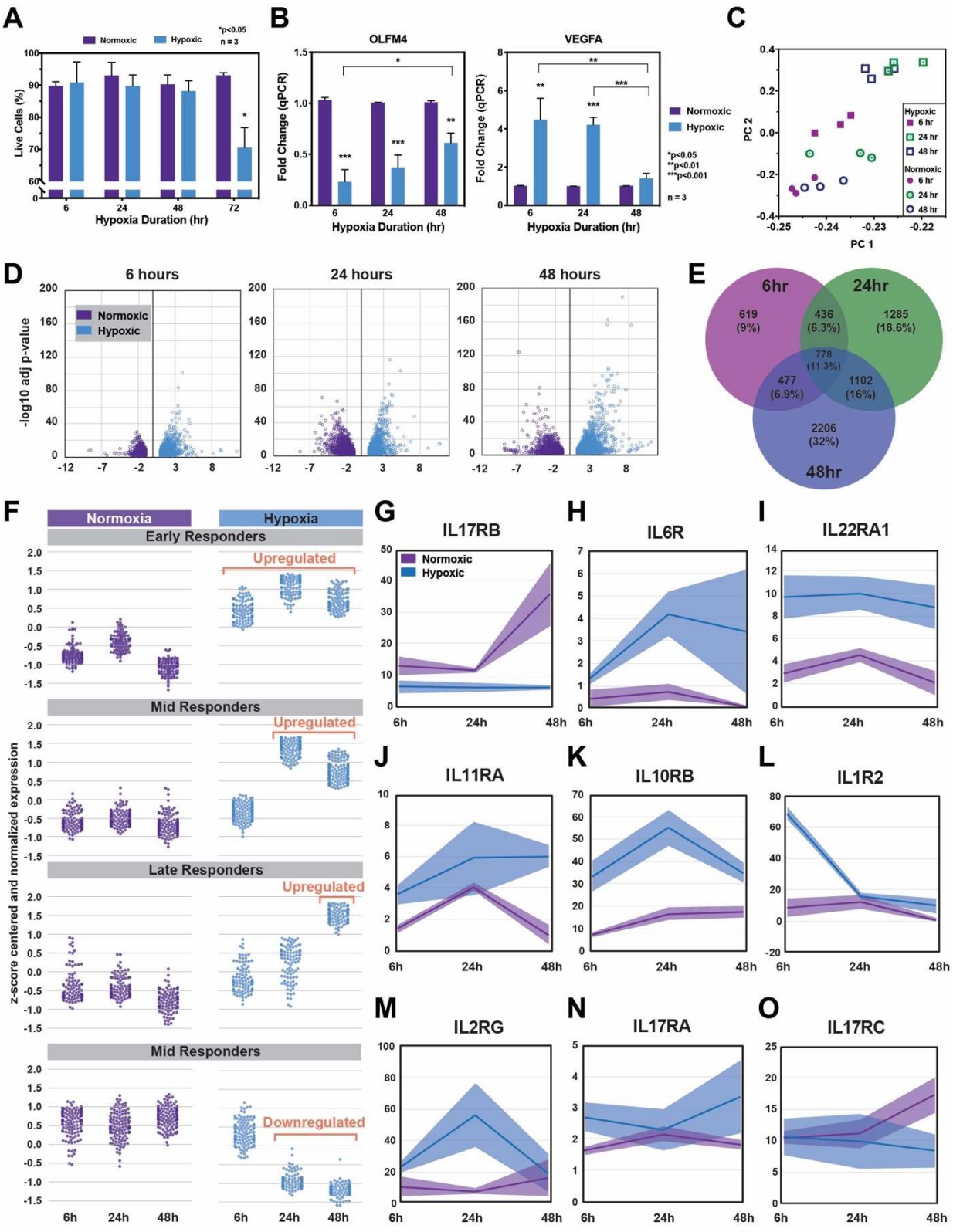
A
Normoxic
Hypoxic
*p<0.05
n = 3
Live Cells (%)
Hypoxia Duration (hr)
B
OLFM4
VEGFA
Fold Change (qPCR)
Hypoxia Duration (hr)
Normoxic
Hypoxic
*p<0.05
**p<0.01
***p<0.001
n = 3
C
PC 1
PC 2
Hypoxic
6 hr
24 hr
48 hr
Normoxic
6 hr
24 hr
48 hr
D
6 hours
24 hours
48 hours
Normoxic
Hypoxic
-log10 adj p-value
E
6hr
24hr
48hr
619
(9%)
436
(6.3%)
1285
(18.6%)
778
(11.3%)
477
(6.9%)
1102
(16%)
2206
(32%)
F
Normoxia
Hypoxia
Early Responders
Upregulated
Mid Responders
Upregulated
Late Responders
Upregulated
Mid Responders
Downregulated
z-score centered and normalized expression
6h
24h
48h
G
IL17RB
Normoxic
Hypoxic
H
IL6R
I
IL22RA1
J
IL11RA
K
IL10RB
L
IL1R2
M
IL2RG
N
IL17RA
O
IL17RC

Figure 4.4 Characterizing transcriptomic changes following 3 durations of hypoxia inside microphysiological system (MPS) using Advanta RNA-sequencing. (A) Flow cytometry results from single cells isolated after 6, 24, 48, and 72 hours from normoxic and hypoxic MPS and stained for Annexin V (-) to quantify live cells (%). (B) qRT-PCR results of human intestinal epithelium isolated from MPS for downstream HIF1A target (VEGFA) and active stem cell marker (OLFM4) after 6 hours, 24 hours, and 48 hours of normoxia or hypoxia culture inside separate MPS. (C) Principle component analysis of RNA-seq results showing clusters of replicate samples from each time point (6, 24, 48 hours) and condition (normoxia or hypoxia). Bulk RNA-sequencing samples were sequenced from a range of 39 to 93 million reads. (D) Volcano plots of each time point (6, 24, 48 hours) and condition (normoxia or hypoxia). (E) Venn Diagram of genes upregulated at each time point (6, 24, 48 hours) after hypoxia. (F) Z-score normalized and centered expression values for genes with expression shifts under hypoxic conditions consistently, at the mid-point (top down respectively) and end of the experimental period with a single group of genes being downregulated at the mid-point (bottom). (G-O) Cross sample normalized gene expression is shown with (standard deviation) under normoxic and hypoxic conditions for interleukin receptors in which at least one time point is significantly different.

CHAPTER 5: SCOPE OF WORK, SIGNIFICANCE, AND IMPLICATIONS FOR FUTURE STUDIES

5.1. Scope of Work

Biological studies of human tissues and organs can only hope to reveal accurate human-like response *in vitro* if designed to use microphysiological systems that accurately recapitulate the tissue and provide the most realistic microenvironmental factors. One microenvironmental factor that is often overlooked in biological studies is oxygen. It is a vital component of all human tissues and is required for the regular energy metabolism of most cells within the human body, apart from anaerobic bacteria. As discussed in chapter 2, most biological studies ignore oxygen unless researchers are interested in studying oxygen-cell based phenomena, either in normal physiology or pathophysiology. Moreover, questions concerning the influence of oxygen on cellular functions can only be answered using *in vitro* systems, in lieu of traditional animal models, that provide methods and readouts to measure and regulate oxygen throughout each biological study.

Here, two particular microphysiological systems (MPS) are designed and fabricated to recapitulate the 3D environment of human breast epithelium and primary human intestinal epithelial stem cells (ISCs), respectively. Both systems are monitored in real-time using biocompatible oxygen sensors that are placed within the 3D culture. Using these models, we ask specific questions concerning oxygen regulation and tissue hypoxia on cell viability, proliferation, and differentiation. ISCs are also isolated from MPS and re-introduced to an oxygen rich 3D environment to investigate stem cell pluripotency. Using primary human ISCs

isolated from MPS, we performed bulk RNA sequencing to generate a data set composed of more than 35,000 genes from three durations of hypoxia and compared these transcriptomes to time-matched control ISCs.

5.2. Significance of Research Findings

Building a microphysiological system that allowed for continuous measurement and control of oxygen involved designing a system with user interface in mind but required many iterations for optimal cell functionality. In the system described in chapter 3, human breast epithelial cells were first grown in tissue culture flasks, then transferred as single cells into 3D Matrigel with integrated phosphorescence-based photonic oxygen biosensors (iPOBs) inside the 3D matrix. It was critical to measure oxygen at the cell layer, because concentration gradients naturally exist from hydrogel to media and from media to air spaces. Once oxygen monitoring was established, we sought to study how lowering the oxygen environment down to hypoxic levels influenced both healthy human breast epithelial cells as well as tumorigenic human breast epithelial cells. We found that nontumorigenic cells were more susceptible to cell death than tumorigenic cells when exposed to hypoxic culture conditions. Interestingly, genetic analysis revealed nontumorigenic breast epithelial cells also increased their expression of genes related to glycolytic metabolism in hypoxia, as compared to normoxic culture. Using this 3D breast epithelial cell culture, it would be possible to extend these studies to longer periods of time and compare the morphology and genetic functionality of organoids formed from either tumorigenic or healthy single cells in each oxygen condition.

Intestinal injuries that include oxygen deprivation are severe and can cause irreversible damage. Oxygen deprivation, caused by ischemia or instances of hypoxia, can itself lead to tissue damage and cell death. Lack of oxygen is also a trigger that can promote the production of

harmful substances and recruitment of damaging inflammatory and immune regulators. Conversely, physiological hypoxia promotes stem cell expansion and functionality in specific tissues and organs. We sought to better define the stem cell capabilities of primary human intestinal epithelial stem cells cultured under severe hypoxia, as compared to routine normobaric culture of ISCs. We found that ISCs culture under severe hypoxia for 24 hours showed increasing proliferation but decreased organoid formation. Interestingly, 48 hours of hypoxic culture resulted in higher initial organoid survival following the return of dissociated ISC to an oxygenated environment in 3D culture. Bulk RNAseq showed a similar transcriptomic response. By 48 hours the epithelial cells had shifted to upregulation of metabolic processes instead of the regulation of cell death and regulation of cell apoptosis pathways most upregulated after 24 hours of hypoxia.

5.3. Implications for Future Studies

Microphysiological systems (MPS) with decreased replication variability and well-defined parameters can realistically replace standard tissue culture plates for many biological studies. MPS generated from patient-derived primary stem cells, as used in Chapter 4, can also be used to better inform patient-specific therapies and quickly rule out inactive drug candidates. It is important to design and build MPS for the purpose of recapitulating human physiology, whether to study normal cell processes or abnormal pathologies. The research presented in Chapter 4 focused on studying primary human intestinal epithelial stem cells in the context of oxygenation and stem cell function. Similar oxygen metrics could be applied to already diseased intestinal tissues to inform clinicians on optimal cutoffs to preserve stem cell function.

Beyond the intestine, oxygen control in other MPS can provide another metric to further investigate vascular and avascular organ systems. Many cellular pathways responsible for tissue

homeostasis and tissue development are dependent on continuous oxygen supply. When oxygen is no longer available, such as when primary cells are isolated from human tissues and grown in thick 3D scaffolds, the cells are expected to adjust or adapt to the new, potentially much lower, local concentrations of oxygen and continue performing cellular as *in vivo*. This assumption that no physiology is altered by the sharp decrease in available oxygen limits many findings from *in vitro* studies. By adding oxygen via gas flow or continuous perfusion of oxygenated media, a more physiologic environment can be established within any desired model system.

APPENDIX A: SUPPLEMENTARY MATERIAL FOR CHAPTER 3[4]

A.1 Detailed Materials and Methods

Cell Culture. Immortalized benign human breast epithelial cells (MCF-10A, CRL-10317; ATCC) [333] were cultured inside 75 cm^2 culture flasks (10062-860; VWR) containing Mammary Epithelial Cell Growth Medium (EGM) supplemented with EGM SingleQuot (CC-3124; Lonza). Non-metastatic tumorigenic human breast epithelial cells (BT474, HTB-20; ATCC) [334] were cultured inside 75 cm^2 culture flasks containing Dulbecco's Modified Eagle's Medium (DMEM) with 4.5 g/L glucose, L-glutamine and sodium pyruvate (10013CV; Corning) and supplemented with 10% fetal bovine serum (97068-086; VWR) and 1% penicillin streptomycin (30-002-Cl; Corning). MCF-10A and BT474 cells were cultured in a normobaric incubator maintaining a temperature of 37°C containing 5% CO_2, 70.2% N_2, 21% O_2 and 100% humidity. For conversion from 2D adherent monolayers to 3D embedded culture, cells were removed from 75 cm^2 culture flasks using sterile 1X DPBS (MT21040CV; ThermoFisher) and Trypsin with 0.25% EDTA (25200072; ThermoFisher) and seeded inside 8.2 mg/mL High Concentration (HC) Matrigel Basement Membrane Matrix (354248; Corning). 48-well plates (100062-898; VWR) were used to culture cells in Matrigel® for control samples. The 200 µL of cell-laded Matrigel® was cast inside the cell culture chamber following established protocols for culturing breast epithelial cells in 3D hydrogel scaffolds.[335] 200 µL of cell-laded Matrigel® inside the 3D cell culture chamber of diameter 11 mm corresponds to a height of ≈ 2.11 mm. The total height of 3D tissue scaffold

[4] Appendix A previously appeared in Biosensors and Bioelectronics. The original citation is as follows: Kristina R. Rivera, Patrick D. Erb, Ashlyn T. Young, Natalie A. Wisniewski, Scott T. Magness, Michael A. Daniele. Integrated phosphorescence-based photonic biosensor (iPOB) for monitoring oxygen levels in 3D cell culture systems. Biosensors and Bioelectronics, 123: 131-140, 2019.

(Matrigel® plus medium) with 200 μL of medium overlaid on top of the cell-laded Matrigel® was 4.21 mm.

Computational Models. The Fluid Dynamics and Transport of Dilute Species Multiphysics® were coupled to establish the boundary conditions for oxygen transport within the device. The computational model included the diffusion coefficient of oxygen through phosphate-buffered saline (1X PBS at 37°C, 2.46 x 10^{-9} $m^2 \cdot s^{-1}$[354]), the diffusion coefficient of oxygen in air (1.75 x 10^{-5} $m^2 \cdot s^{-1}$[410]), the inlet flow rate of deoxygenated air, or 100% N_2, which varied from 1 to 7 $mL \cdot min^{-1}$, and an outlet gas pressure of 0 Pa. The simulation solved for oxygen pressure in units of kilopascals (kPa); therefore, O_2 saturation coefficients were not required. The model geometry was meshed using a physics-controlled mesh and the time-dependent solver (PARADISO) computed solutions over a time range of 0 to 80 minutes with steps of 2 minutes.

Immunohistochemistry and gene expression. The breast epithelial cells encapsulated in Matrigel® were removed from the 3D culture-gas exchange chamber for IHC analysis. First, the iPOB was removed from the Matrigel® and, the remaining Matrigel® containing breast epithelial cells was placed into a 48-well plate, along with 4% paraformaldehyde (PFA) solution for fixation. After incubation at room temperature for 20 minutes, the fixative was removed from each well and samples were rinsed three times with 1X PBS. Cells encapsulated in Matrigel® were then permeabilized using a solution of 0.5% Triton-X100 in 1X PBS for 30 minutes and rinsed three times with 1X PBS. Samples were blocked with protein block solution (1:5 dilution in 1X PBS; Cat. No. X090930-2; Agilent) for 1 hour at room temperature. Briefly, after blocking, samples were stained with primary antibodies Laminin alpha V (rabbit, 1:100 dilution in protein block, Cat. No. sc-20145; Santa Cruz) and beta II Tubulin (chicken, 1:100 dilution in protein block, TUJ-S; Aves Labs) for 2 hours at room temperature and rinsed three times with 1X PBS. Next, samples

were stained with secondary antibodies, Dylight 649 (goat anti-rabbit, 1:250 dilution in protein block, Cat. No. 111-496-003; Jackson ImmunoResearch Laboratories, Inc.) and Dylight 488 (goat anti-chicken, 1:250 dilution in protein block, Cat. No. 103-485-155; Jackson) for 45 minutes at room temperature. Nuclei counterstain was then performed with bisbenzamide (1:1000 dilution in 1X PBS) for 5 minutes at room temperature.

Briefly, cells encapsulated in Matrigel® were lysed in 200 µL of RNA Lysis buffer. Total RNA was extracted using RNAqueous-Micro Total RNA Isolation Kit (AM1931; ThermoFisher) according to manufacturer's protocols and stored at −80°C. cDNA was generated from ~2 ng of total RNA from each sample using iScript Reverse Transcription Supermix for RT-qPCR (170-8891; BioRad) according to manufacturer's protocols. cDNA was diluted 1:20 and 1 µL was used for qRT-PCR using Taqman probes (Applied Biosystems) and SsoAdvanced Universal Probes Supermix (1725281; BioRad) according to manufacturer's protocols. qRT-PCR was carried out in a StepOnePlus Real Time PCR System (Applied Biosystems).

APPENDIX B: SUPPLEMENTARY MATERIAL FOR CHAPTER 4[5]

B.1 Supplemental Figures

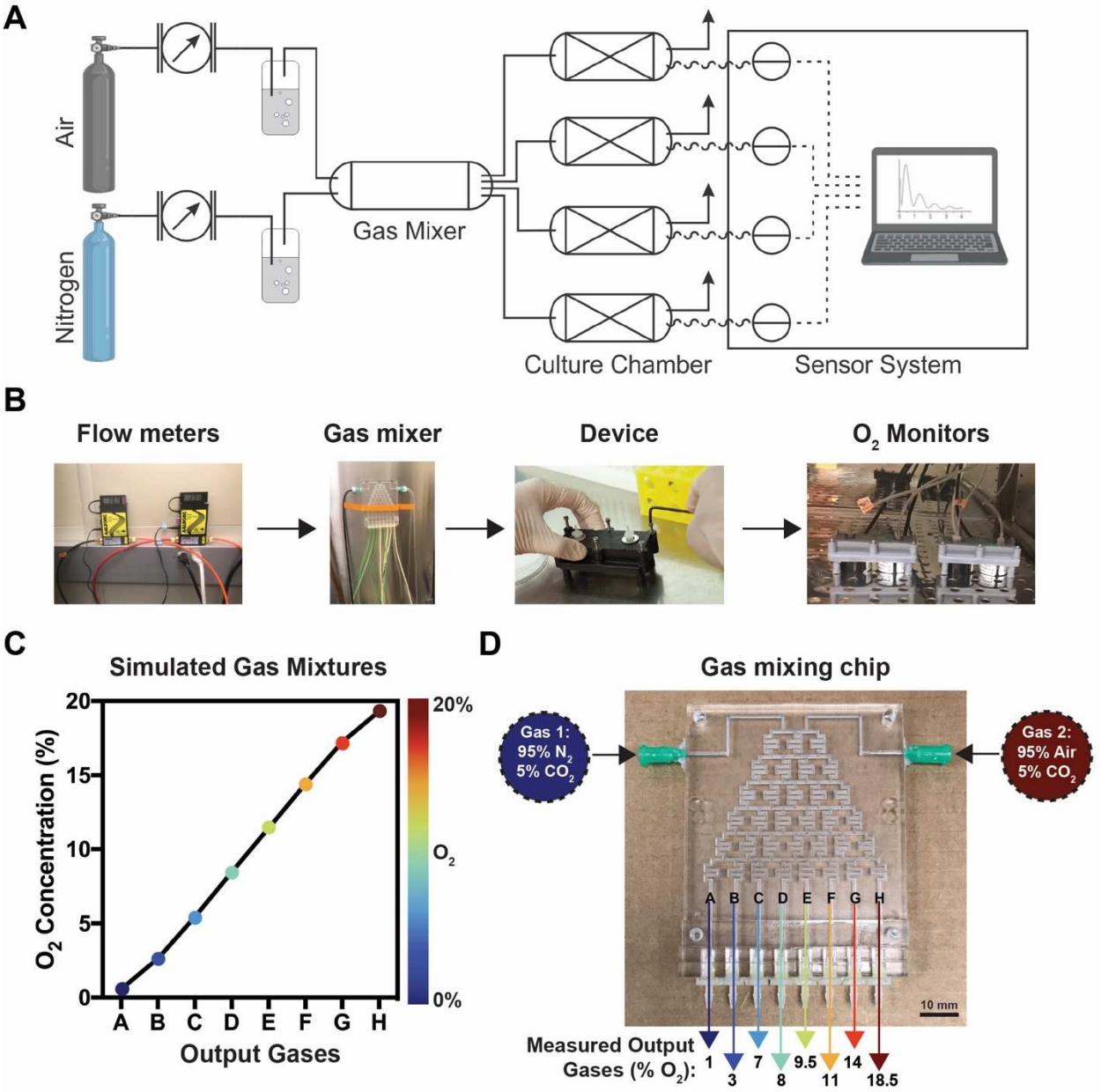

Fig. B.1 Gas mixing chip integrated into microphysiological system to generate 8 different oxygen environments. (A) Schematic of complete microphysiological system design with mixed

[5] Full list of contributing authors: Kristina R. Rivera, Michael J. Czerwinski, Vladimir A. Pozdin, Ming Yao, Michael A. Daniele, and Scott T. Magness.

gases in tanks leading into flow meters. Flow meters connect into humidification 15 mL conicals filled with sterile PBS. Humidified gases travel into each input of the gas mixer chip, and 8 concentrations of gases exit individual outlets to connect into separate microphysiological systems (devices). Device oxygen concentration is monitored using detectors that send information to a laptop located beside the incubator. (B) Images taken of each component of the system. (C) COMSOL Multiphysics results for the simulated gas mixtures from each outlet of the gas mixing chip. (D) Image of the gas mixing chip and measured output oxygen concentrations recorded inside individual devices.

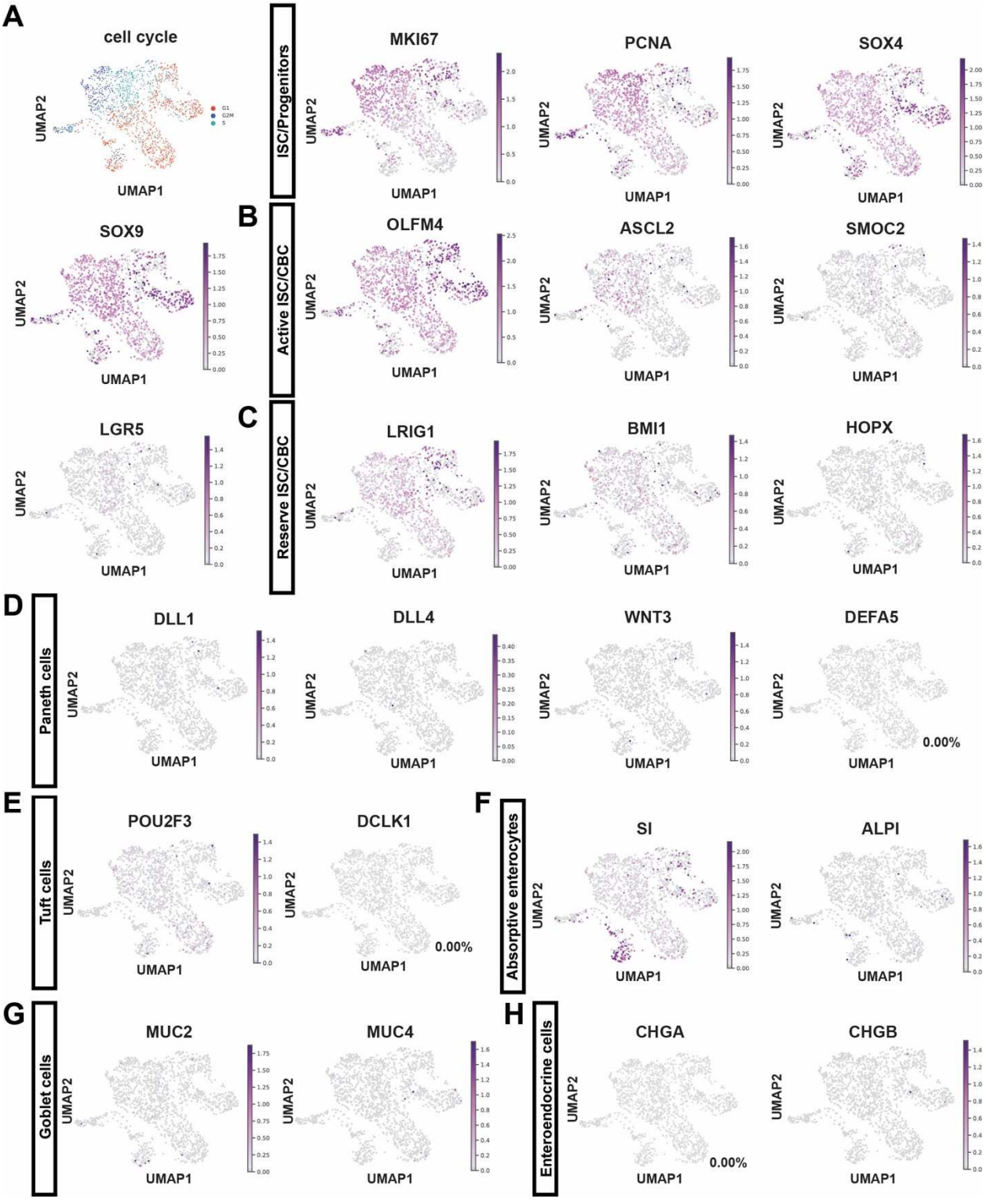

Fig. B.2 UMAP plots of cell cycle scoring and marker gene expression in singe-cell RNA sequencing data from human intestinal epithelial culture. (A) UMAP plot of assignment of cell

cycle stage based on cell cycle gene scoring (left) with accompanying proliferative marker genes. (B) UMAP plots of gene expression for stem cell marker genes. (C) UMAP plots of gene expression for putative reserve stem cell marker genes. (D) UMAP plot of gene expression for Paneth cell maker genes. (E) UMAP plot of gene expression for Tuft cell marker genes. (F) UMAP plots of gene expression for absorptive enterocyte marker genes. (G) UMAP plots of gene expression for goblet cell marker genes. (H) UMAP plots of gene expression for enteroendocrine cell marker genes. *Color scales show expression from zero/low (grey) to high (dark purple).

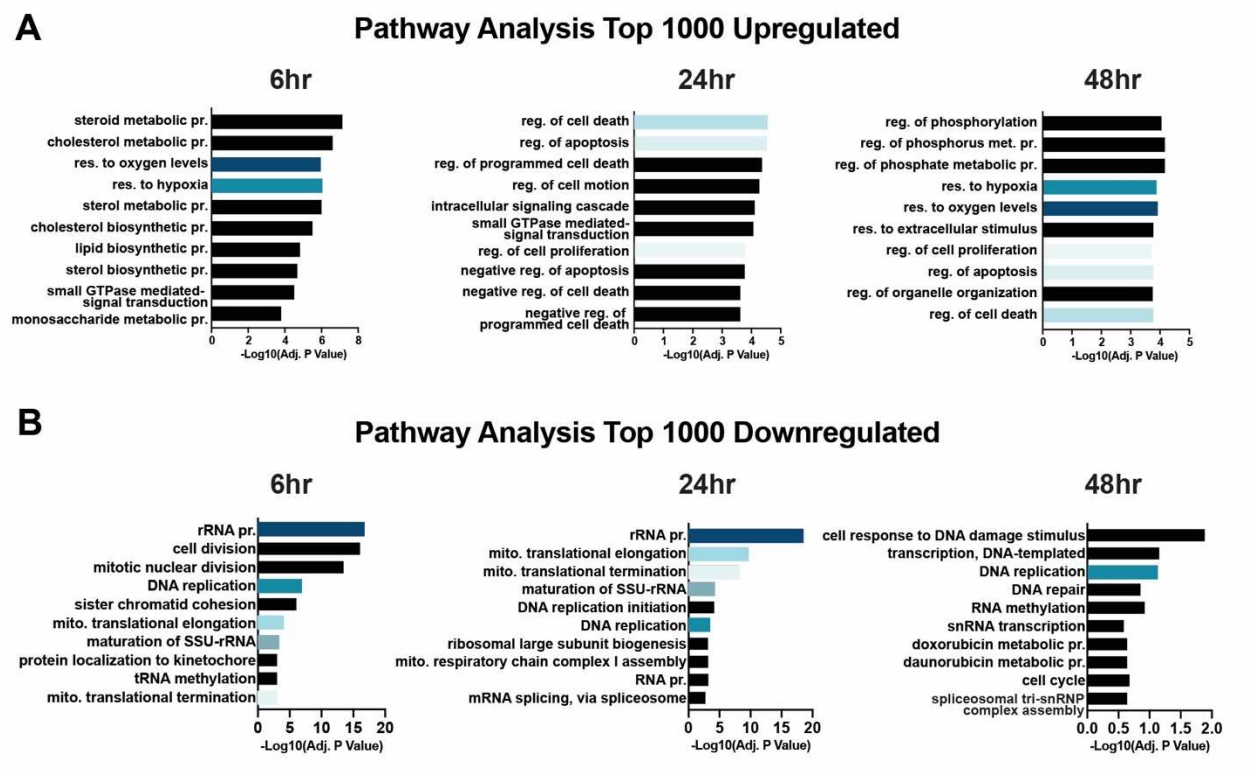

Fig. B.3 Pathway analysis of human intestinal epithelium after 3 durations of either hypoxic or normoxic culture inside the microphysiological system (MPS). (A) Pathway analysis (DAVID) of Gene Ontology (GO) comparing the Top 1000 Upregulated Genes and transcriptional signatures of hypoxic versus normoxic intestinal epithelial cells after 6 hours, 24 hours, and 48 hours. (B) Pathway analysis (DAVID) of Gene Ontology (GO) comparing the Top 1000 Downregulated Genes and transcriptional signatures of hypoxic versus normoxic intestinal epithelial cells after 6 hours, 24 hours, and 48 hours. Abbreviations for GO pathways include: pr. (process), res. (response), reg. (regulation), met. (metabolic), mito. (mitochondrial).

APPENDIX C: METHODS TO ISOLATE PRIMARY HUMAN AND MURINE INTESTINAL MICROVASCULAR ENDOTHELIAL CELLS

C.1 Overview

The vascular network beneath the intestinal epithelial barrier is responsible for delivering key signaling factors, immune cells, and, of course, oxygen in the form of bound hemoglobin, to the epithelium. Specifically, human intestinal microvascular endothelial cells (HIMECs), are chiefly responsible for creating an endothelial network that extends upward into villi at the small intestine. HIMECs provide a highway for circulating blood cells and for immune cells to extravasate when activated to target epithelial pathogens. While working in the Magness Lab with human intestinal tissues, I spent time developing and testing protocols to isolate primary HIMECs from donor small intestinal tissues, as well as primary murine intestinal microvascular endothelial cells (MIMECs) from mice small intestinal jejunum. After successfully isolating both HIMECs and MIMECs, I expanded and passaged HIMECs in standard tissue culture dishes coated with human fibronectin. Although I was able to passage the HIMECs once from freshly expanded culture, media formulations were not optimized to allow for long-term storage in liquid nitrogen.

C.2 Protocol

Reagents

2.5 mg/ml Type II Collagenase Solution

- 25 mg Type II Collagenase
- 10 mL of Medium 199
- sterile filter with 0.22 syringe filter and pre-warm

Isolation Media

- 2 mL (20% Fetal Bovine Serum)
- 100 µL of 100x penicillin/streptomycin (1X)
- 8 mL of Medium 199

Endothelial cell growth media (EGM-2) for Cell Culture*

- 500 mL EBM-2 basal medium
- 10 mL Fetal Bovine Serum
- 2 mL human Fibroblast Growth Factor beta (hFGF-β)
- 0.5 mL human Endothelial growth factor (hEGF)
- 0.5 mL Vascular endothelial growth factor (VEGF)
- 0.5 mL Human recombinant 3 Long arginine Insulin-like growth factor 1 (R3-IGF-1)
- 0.5 mL Ascorbic Acid
- 0.5 mL Heparin
- 0.2 mL Hydrocortisone
- 0.5 mL Gentamicin/Amphotericin B

* supplemented with 1:500 Primocin to prevent contamination

1. Fill 5 50mL conicals with 30mL non-sterile PBS. Label 1 tube "PBS." Fill 2 of these tubes with 180uL EDTA (3mM) and label "EDTA 1" and "EDTA 2". Fill 1 tube with 15 µL of 1M DTT to make 0.5 mmol/L dithiothreitol (DTT) solution and label "DTT". Add 30 µL of Y-27632 to 2 tubes and label "Shake 1" and "Shake 2". Put all conicals on ice.

2. Measure intestinal segment and open longitudinally, mucosal side-up into a petri dish filled with PBS

3. Perform mucosectomy by dissecting specimen into 0.5 x 2 to 3 cm mucosal strips (see image below)

4. Rinse strips briefly in PBS labeled tube.

5. Use 100 µm strainer to transfer mucosal strips from PBS tube to DTT tube.

6. Shake on rocker at room temperature for 30 min at 100 rpm.

7. Transfer strips from DTT to EDTA 1 tube.

8. Shake on rocker at 4ºC at 85 rpm for 15 minutes - prepare collagenase solution while waiting.

9. Transfer strips from EDTA 1 tube to EDTA 2 tube.

10. Return to rocker for 45 minutes (60 minutes total).

11. Pour off solution, leaving the mucosal strips in the conical. Add in Shake 1 solution.

12. Shake at 3 cycles per second for 2 minutes.

13. Transfer tissue to Shake 2 tube.

14. Shake again at 3 cycles per second for 2 minutes.

15. Use the microscope to confirm that the mucosal strips are depleted of epithelial cells.

16. Mince mucosal strips into 2 x 2 mm fragments (see image below) inside incubator and transferred fragments into Collagenase solution for 30 minutes at 37ºC to digest fragments.

17. Mechanically agitate fragments to release cells by gently shaking the tube by hand.

18. Pass suspension through 70 µm strainer and wash strainer with Isolation media to neutralize collagenase.

19. Use the microscope to confirm there are endothelial cells in solution.

20. Filter half the solution through 40 μm cell strainer to generate purer preparation, label each solution.
21. Centrifuge cell suspensions at 1800g for 3 min.
22. Resuspend each cell pellet in 2.1 mL of media, with approximately 1-5 million cells per ml.
23. Count cells with hemocytometer.
    - take 20 μl of sample
    - add 20 μl of 0.2% trypan blue dye (1:1) to each, mixed gently
    - add 10 μl of dyed cells to hemocytometer
    - count 4 squares, then take average to multiply by 20,000. This is the cell density in cells /mL.
24. Take 300 μL from each sample for single color controls. Dilute with 1200 μl of Isolation media. With this 1500 μl volume cell solution, divide equally into 5 tubes (each with 250 μL) labeled as:
    - CD326 only
    - CD45 only
    - CD31 only
    - Annexin V and 7-AAD together
    - unstained control
25. Stain 1.8 mL of cell sample with antibodies for CD45 (1:250, 7.2 μl), CD326, CD31 (both 1:100, 18 μl each) and make single color controls (1:100, 2.5 μl each, except CD45 1:250, 1 μl).

26. Incubate stained cells on ice for 45 minutes. - prepare human fibronectin coated plates while waiting, using cell count to determine # wells (assuming 5% CD31+ cells in FACS isolation)
    - Create 10 µg/ml fibronectin solution by adding 10 µl of human fibronectin (1mg/ml) to 990 µl of cold DPBS to each well of 48 well plate, incubate 30 minutes at room temperature
    - Aspirate solution, then allow each plate to dry with lid off inside tissue culture hood for 30 minutes
27. Centrifuge samples at 1800 g for 5 minutes on clinical centrifuge at 4ºC.
28. Rinse each sample 1 time with ice cold isolation media and resuspend in isolation media.
29. Add vital dyes (Annexin V 1:1000, 7-AAD 1:1000) to labeled control tube and cell sample tube right before walking over to FACS machine. Dilute stock dyes 1:10 then add 1 µL to color controls. Use 1.9 µL for cell sample.
30. Before sorting put cells stained with dead antibodies in 37ºC bath to warm for 30 seconds.
31. Sort color controls to set FACS gates, then cell sample, isolate CD31+ cells only and immediately plate on collagen coated plate at ~25,000 cells each 48 well plate well.
32. Change media in 24 hours to remove dead cells, then change media every 48 hours until expanded.

Figure C.1 Intestinal Mucosectomy (Left) Segment of human jejunum while mucosectomy is being been performed, with mucosal strips in PBS solution surrounding the segment of tissue. (Right) Mucosal strips minced into fragments to collect HIMECs after depleting the tissue of epithelial cells.

C.3 Preliminary Results

I performed this protocol one time using human intestinal tissue and three times using murine intestinal tissues. For the MIMEC FACS experiments, I replaced the human FACS antibodies for the same fluorophore conjugated FACS antibodies (CD326, CD45, and CD31) specific for murine epithelial, immune, and endothelial cells, respectively. The data showing the portion of CD31+ cells isolated from each intestinal segment, as compared to the total parent population (excluding doublets and dead cells) of live single cells and the total population of cells in each sample from each FACS experiment is plotted below.

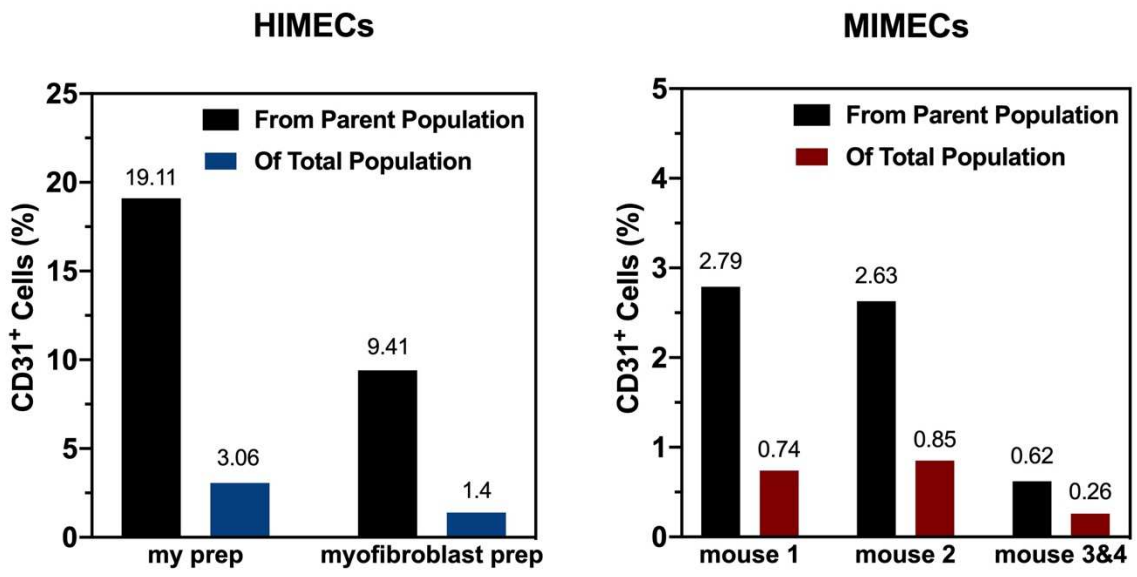

Figure C.2 Fluorescence activated cell sorting (FACS) results (Left) FACS of CD31+ cells from one HIMEC isolation using my protocol, compared to one HIMEC isolation following the protocol for isolating myofibroblasts (Magness Lab Protocol). (Right) Three separate MIMEC isolations from either a single mouse or 2 pooled mice samples.

The human FACS results show a population of approximately 3.1% HIMECs can be isolated from an intestinal segment using CD31 as the positive marker for endothelial cells, sorting out CD45+ (leukocytes) and CD326+ (epithelial cells) and Annexin V+/7-AAD+ (dead cells). We also found that the population of CD31+ cells isolated from the tissue using the protocol for myofibroblast preparation was much lower (1.4%) than the protocol established above.

I was able to culture the isolated HIMECs for 7 days (Brightfield images below) on a well plate coated with human fibronectin. After 7 days in culture, the HIMECs achieved more than 90% confluence. HIMECs were then passaged and expanded for 2 days, and then HIMECs

were fixed and stained using the marker for endothelial cells CD31 (red) used during FACS and the nuclei marker DAPI (blue).

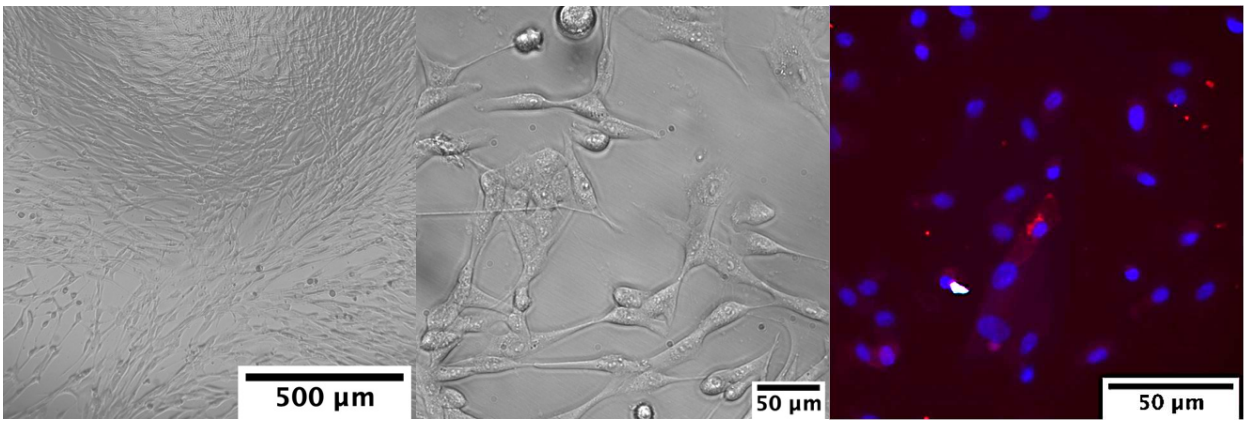

Figure C.3 Human Intestinal Microvascular Endothelial Cell (HIMEC) Expansion (Left & Middle) Day 7 brightfield images of Passage 0 sorted HIMECs. (Right) Fluorescent image of Day 2 Passage 1 HIMECs stained for endothelial cell marker CD31 (red) and nuclei DAPI (blue).

The initial results of the human isolation show that HIMECs can be isolated from intestinal tissues using a mucosectomy and FACS. Fluorescently tagged and sorted HIMECs can then be grown and expanded on fibronectin-coated well plate to confluence. The first passage also shows that HIMECs can be passaged and retain the endothelial cell marker CD31, suggesting they are true endothelial cells and not transforming into fibroblasts. There is the potential to further expand HIMECs for long-term cultures and transplant expanded HIMECs into intestinal microphysiological systems to better recapitulate the human small intestine. An ideal human intestinal microphysiological system would also include immune components and extracellular matrix supporting cells, such as fibroblasts and smooth muscle cells, derived from the same donor tissue.

APPENDIX D: REPRINTING PERMISSIONS

D.1 Reprinting Permissions

1. Chapter 2 previously appeared in Analyst. Original citation: Kristina R. Rivera, Murat A. Yokus, Patrick D. Erb, Vladimir A. Pozdin, Michael A. Daniele. Measuring and regulating oxygen levels in microphysiological systems: Design, material, and sensor considerations. Analyst 144(10), 3190-3215. (2019). - Reproduced by permission of The Royal Society of Chemistry.
2. Chapter 3 and Appendix A previously appeared in Biosensors and Bioelectronics. Original citation: Kristina R. Rivera, Patrick D. Erb, Ashlyn T. Young, Natalie A. Wisniewski, Scott T. Magness, Michael A. Daniele. Integrated phosphorescence-based photonic biosensor (iPOB) for monitoring oxygen levels in 3D cell culture systems. Biosensors and Bioelectronics, 123: 131-140, 2019. - Reproduced by permission of Elsevier.

REFERENCES

1. Kraehenbuhl, J.P., E. Pringault, and M.R. Neutra, *Review article: Intestinal epithelia and barrier functions.* Aliment Pharmacol Ther, 1997. **11 Suppl 3**: p. 3-8; discussion 8-9.

2. Martin-Belmonte, F. and M. Perez-Moreno, *Epithelial cell polarity, stem cells and cancer.* Nat Rev Cancer, 2011. **12**(1): p. 23-38.

3. Sato, T., et al., *Paneth cells constitute the niche for Lgr5 stem cells in intestinal crypts.* Nature, 2011. **469**(7330): p. 415-8.

4. Bitar, K.N. and E. Zakhem, *Bioengineering the gut: future prospects of regenerative medicine.* Nat Rev Gastroenterol Hepatol, 2016. **13**(9): p. 543-56.

5. Clevers, H.C. and C.L. Bevins, *Paneth cells: maestros of the small intestinal crypts.* Annu Rev Physiol, 2013. **75**: p. 289-311.

6. Barker, N., et al., *Crypt stem cells as the cells-of-origin of intestinal cancer.* Nature, 2009. **457**(7229): p. 608-11.

7. Kim, Y.S. and S.B. Ho, *Intestinal goblet cells and mucins in health and disease: recent insights and progress.* Curr Gastroenterol Rep, 2010. **12**(5): p. 319-30.

8. Rindi, G., et al., *The "normal" endocrine cell of the gut: changing concepts and new evidences.* Ann N Y Acad Sci, 2004. **1014**: p. 1-12.

9. Gerbe, F., et al., *DCAMKL-1 expression identifies Tuft cells rather than stem cells in the adult mouse intestinal epithelium.* Gastroenterology, 2009. **137**(6): p. 2179-80; author reply 2180-1.

10. Thermann, M., et al., *[Oxygen supply of the human small intestine in mechanical ileus]*. Langenbecks Arch Chir, 1985. **363**(3): p. 179-84.

11. Espey, M.G., *Role of oxygen gradients in shaping redox relationships between the human intestine and its microbiota.* Free Radic Biol Med, 2013. **55**: p. 130-40.

12. Carreau, A., et al., *Why is the partial oxygen pressure of human tissues a crucial parameter? Small molecules and hypoxia.* J Cell Mol Med, 2011. **15**(6): p. 1239-53.

13. Fagundes, R.R. and C.T. Taylor, *Determinants of hypoxia-inducible factor activity in the intestinal mucosa.* J Appl Physiol (1985), 2017. **123**(5): p. 1328-1334.

14. Vollmar, B. and M.D. Menger, *Intestinal ischemia/reperfusion: microcirculatory pathology and functional consequences.* Langenbecks Arch Surg, 2011. **396**(1): p. 13-29.

15. Chiu, C.J., et al., *Intestinal mucosal lesion in low-flow states. I. A morphological, hemodynamic, and metabolic reappraisal.* Arch Surg, 1970. **101**(4): p. 478-83.

16. Matthijsen, R.A., et al., *Enterocyte shedding and epithelial lining repair following ischemia of the human small intestine attenuate inflammation.* PLoS One, 2009. **4**(9): p. e7045.

17. Grootjans, J., et al., *Life and death at the mucosal-luminal interface: New perspectives on human intestinal ischemia-reperfusion.* World J Gastroenterol, 2016. **22**(9): p. 2760-70.

18. Mallick, I.H., et al., *Ischemia-reperfusion injury of the intestine and protective strategies against injury.* Dig Dis Sci, 2004. **49**(9): p. 1359-77.

19. de Groot, H. and U. Rauen, *Ischemia-reperfusion injury: processes in pathogenetic networks: a review.* Transplant Proc, 2007. **39**(2): p. 481-4.

20. Kannan, K.B., et al., *Hypoxia-inducible factor plays a gut-injurious role in intestinal ischemia reperfusion injury.* Am J Physiol Gastrointest Liver Physiol, 2011. **300**(5): p. G853-61.

21. Guan, Y., et al., *Intestinal ischemia-reperfusion injury: reversible and irreversible damage imaged in vivo.* Am J Physiol Gastrointest Liver Physiol, 2009. **297**(1): p. G187-96.

22. Cerqueira, N.F., C.A. Hussni, and W.B. Yoshida, *Pathophysiology of mesenteric ischemia/reperfusion: a review.* Acta Cir Bras, 2005. **20**(4): p. 336-43.

23. Massberg, S. and K. Messmer, *The nature of ischemia/reperfusion injury.* Transplant Proc, 1998. **30**(8): p. 4217-23.

24. Jin, Y. and A.T. Blikslager, *Intestinal Ischemia-Reperfusion: Rooting for the SOCS?* Dig Dis Sci, 2017. **62**(1): p. 4-6.

25. Noda, T., et al., *Programmed cell death induced by ischemia-reperfusion in rat intestinal mucosa.* Am J Physiol, 1998. **274**(2 Pt 1): p. G270-6.

26. Chen, Y., et al., *Depletion of intestinal resident macrophages prevents ischaemia reperfusion injury in gut.* Gut, 2004. **53**(12): p. 1772-80.

27. Manresa, M.C. and C.T. Taylor, *Hypoxia Inducible Factor (HIF) Hydroxylases as Regulators of Intestinal Epithelial Barrier Function.* Cell Mol Gastroenterol Hepatol, 2017. **3**(3): p. 303-315.

28. Morote-Garcia, J.C., et al., *Hypoxia-inducible factor-dependent repression of equilibrative nucleoside transporter 2 attenuates mucosal inflammation during intestinal hypoxia.* Gastroenterology, 2009. **136**(2): p. 607-18.

29. Biddlestone, J., D. Bandarra, and S. Rocha, *The role of hypoxia in inflammatory disease (review).* Int J Mol Med, 2015. **35**(4): p. 859-69.

30. Giles, R.H., et al., *Interplay between VHL/HIF1alpha and Wnt/beta-catenin pathways during colorectal tumorigenesis.* Oncogene, 2006. **25**(21): p. 3065-70.

31. Furuta, G.T., et al., *Hypoxia-inducible factor 1-dependent induction of intestinal trefoil factor protects barrier function during hypoxia.* J Exp Med, 2001. **193**(9): p. 1027-34.

32. Semenza, G.L., et al., *Hypoxia-inducible factor 1: from molecular biology to cardiopulmonary physiology.* Chest, 1998. **114**(1 Suppl): p. 40S-45S.

33. Schofield, C.J. and P.J. Ratcliffe, *Oxygen sensing by HIF hydroxylases.* Nat Rev Mol Cell Biol, 2004. **5**(5): p. 343-54.

34. Louis, N.A., et al., *Selective induction of mucin-3 by hypoxia in intestinal epithelia.* J Cell Biochem, 2006. **99**(6): p. 1616-27.

35. Karhausen, J., et al., *Epithelial hypoxia-inducible factor-1 is protective in murine experimental colitis.* J Clin Invest, 2004. **114**(8): p. 1098-106.

36. Giatromanolaki, A., et al., *Hypoxia inducible factor 1alpha and 2alpha overexpression in inflammatory bowel disease.* J Clin Pathol, 2003. **56**(3): p. 209-13.

37. Zhang, C., et al., *Hypoxia induces the breast cancer stem cell phenotype by HIF-dependent and ALKBH5-mediated m(6)A-demethylation of NANOG mRNA.* Proc Natl Acad Sci U S A, 2016. **113**(14): p. E2047-56.

38. Iriondo, O., et al., *Distinct breast cancer stem/progenitor cell populations require either HIF1alpha or loss of PHD3 to expand under hypoxic conditions.* Oncotarget, 2015. **6**(31): p. 31721-39.

39. Forristal, C.E., et al., *Hypoxia inducible factors regulate pluripotency and proliferation in human embryonic stem cells cultured at reduced oxygen tensions.* Reproduction, 2010. **139**(1): p. 85-97.

40. Fujimoto, K., et al., *Effect of ischemia-reperfusion on lipid digestion and absorption in rat intestine.* Am J Physiol, 1991. **260**(4 Pt 1): p. G595-602.

41. Ikeda, H., et al., *Apoptosis is a major mode of cell death caused by ischaemia and ischaemia/reperfusion injury to the rat intestinal epithelium.* Gut, 1998. **42**(4): p. 530-7.

42. Sato, N., et al., *Differential induction of PPAR-gamma by luminal glutamine and iNOS by luminal arginine in the rodent postischemic small bowel.* Am J Physiol Gastrointest Liver Physiol, 2006. **290**(4): p. G616-23.

43. Szabo, C. and T.R. Billiar, *Novel roles of nitric oxide in hemorrhagic shock.* Shock, 1999. **12**(1): p. 1-9.

44. Breithaupt-Faloppa, A.C., et al., *Protective effect of estradiol on acute lung inflammation induced by an intestinal ischemic insult is dependent on nitric oxide.* Shock, 2013. **40**(3): p. 203-9.

45. Li, Y., et al., *6-Gingerol protects intestinal barrier from ischemia/reperfusion-induced damage via inhibition of p38 MAPK to NF-kappaB signalling.* Pharmacol Res, 2017. **119**: p. 137-148.

46. Ricardo-da-Silva, F.Y., et al., *Estradiol Modulates Local Gut Injury Induced by Intestinal Ischemia-Reperfusion in Male Rats.* Shock, 2017. **48**(4): p. 477-483.

47. He, G.Z., et al., *Impact of intestinal ischemia/reperfusion and lymph drainage on distant organs in rats.* World J Gastroenterol, 2012. **18**(48): p. 7271-8.

48. Ozacmak, H.S., et al., *Pretreatment with mineralocorticoid receptor blocker reduces intestinal injury induced by ischemia and reperfusion: involvement of inhibition of inflammatory response, oxidative stress, nuclear factor kappaB, and inducible nitric oxide synthase.* J Surg Res, 2014. **191**(2): p. 350-61.

49. Turan, I., et al., *Agmatine attenuates intestinal ischemia and reperfusion injury by reducing oxidative stress and inflammatory reaction in rats.* Life Sci, 2017. **189**: p. 23-28.

50. Gonzalez, L.M., A.J. Moeser, and A.T. Blikslager, *Animal models of ischemia-reperfusion-induced intestinal injury: progress and promise for translational research.* Am J Physiol Gastrointest Liver Physiol, 2015. **308**(2): p. G63-75.

51. Hotchkiss, R.S., et al., *Rapid onset of intestinal epithelial and lymphocyte apoptotic cell death in patients with trauma and shock.* Crit Care Med, 2000. **28**(9): p. 3207-17.

52. Derikx, J.P., et al., *Rapid reversal of human intestinal ischemia-reperfusion induced damage by shedding of injured enterocytes and reepithelialisation.* PLoS One, 2008. **3**(10): p. e3428.

53. Grootjans, J., et al., *Human intestinal ischemia-reperfusion-induced inflammation characterized: experiences from a new translational model.* Am J Pathol, 2010. **176**(5): p. 2283-91.

54. Chen, L.W., et al., *The two faces of IKK and NF-kappaB inhibition: prevention of systemic inflammation but increased local injury following intestinal ischemia-reperfusion.* Nat Med, 2003. **9**(5): p. 575-81.

55. Panes, J. and D.N. Granger, *Leukocyte-endothelial cell interactions: molecular mechanisms and implications in gastrointestinal disease.* Gastroenterology, 1998. **114**(5): p. 1066-90.

56. Blikslager, A.T., et al., *Restoration of barrier function in injured intestinal mucosa.* Physiol Rev, 2007. **87**(2): p. 545-64.

57. Domenech, M., et al., *Cellular observations enabled by microculture: paracrine signaling and population demographics.* Integr Biol (Camb), 2009. **1**(3): p. 267-74.

58. Yang, Y., et al., *Amino acid deprivation disrupts barrier function and induces protective autophagy in intestinal porcine epithelial cells.* Amino Acids, 2015. **47**(10): p. 2177-84.

59. Liu, L., et al., *miR-381-3p knockdown improves intestinal epithelial proliferation and barrier function after intestinal ischemia/reperfusion injury by targeting nurr1.* Cell Death Dis, 2018. **9**(3): p. 411.

60. Wang, Y.D., M.; Gunasekara, D. B.; Dutton, J.; Proctor, A.; Lebhar, M. S.; Williamson, I. A.; Speer, J.; Howard, R. L.; Smiddy, N. M.; Bultman, S. J.; Sims, C. E.; Magness, S. T.; Allbritton, N. L., *Self-renewing Monolayer of Primary Colonic or Rectal Epithelial Cells.* Cellular and Molecular Gastroenterology and Hepatology, 2017. **4**(1): p. 165 - 182.

61. Gracz, A.D., B.J. Puthoff, and S.T. Magness, *Identification, isolation, and culture of intestinal epithelial stem cells from murine intestine.* Methods Mol Biol, 2012. **879**: p. 89-107.

62. Wang, F., et al., *Isolation and characterization of intestinal stem cells based on surface marker combinations and colony-formation assay.* Gastroenterology, 2013. **145**(2): p. 383-95 e1-21.

63. Bhatia, S.N. and D.E. Ingber, *Microfluidic organs-on-chips.* Nat Biotechnol, 2014. **32**(8): p. 760-72.

64. Kump, L.R., *The rise of atmospheric oxygen.* Nature, 2008. **451**(7176): p. 277-8.

65. Hatefi, Y., *The mitochondrial electron transport and oxidative phosphorylation system.* Annu Rev Biochem, 1985. **54**: p. 1015-69.

66. Khanal, G., S. Hiemstra, and D. Pappas, *Probing hypoxia-induced staurosporine resistance in prostate cancer cells with a microfluidic culture system.* Analyst, 2014. **139**(13): p. 3274-80.

67. Secomb, T.W., et al., *Analysis of oxygen transport to tumor tissue by microvascular networks.* Int J Radiat Oncol Biol Phys, 1993. **25**(3): p. 481-9.

68. Akimoto, T., H. Liapis, and M.R. Hammerman, *Microvessel formation from mouse embryonic aortic explants is oxygen and VEGF dependent.* Am J Physiol Regul Integr Comp Physiol, 2002. **283**(2): p. R487-95.

69. Fleury, C., B. Mignotte, and J.L. Vayssiere, *Mitochondrial reactive oxygen species in cell death signaling.* Biochimie, 2002. **84**(2-3): p. 131-41.

70. Fong, G.H., *Regulation of angiogenesis by oxygen sensing mechanisms.* J Mol Med (Berl), 2009. **87**(6): p. 549-60.

71. Helmlinger, G., et al., *Formation of endothelial cell networks.* Nature, 2000. **405**(6783): p. 139-41.

72. Mizukami, Y., et al., *Hypoxia-inducible factor-1-independent regulation of vascular endothelial growth factor by hypoxia in colon cancer.* Cancer Res, 2004. **64**(5): p. 1765-72.

73. Uchida, T., et al., *Prolonged hypoxia differentially regulates hypoxia-inducible factor (HIF)-1alpha and HIF-2alpha expression in lung epithelial cells: implication of natural antisense HIF-1alpha.* J Biol Chem, 2004. **279**(15): p. 14871-8.

74. Wenger, R.H., et al., *Frequently asked questions in hypoxia research.* Hypoxia (Auckl), 2015. **3**: p. 35-43.

75. Whitesides, G.M., *The origins and the future of microfluidics.* Nature, 2006. **442**(7101): p. 368-73.

76. Pampaloni, F., E.G. Reynaud, and E.H. Stelzer, *The third dimension bridges the gap between cell culture and live tissue.* Nat Rev Mol Cell Biol, 2007. **8**(10): p. 839-45.

77. Abaci, H.E., et al., *Microbioreactors to manipulate oxygen tension and shear stress in the microenvironment of vascular stem and progenitor cells.* Biotechnol Appl Biochem, 2012. **59**(2): p. 97-105.

78. Bhaskara, V.K., et al., *Intermittent hypoxia regulates stem-like characteristics and differentiation of neuroblastoma cells.* PLoS One, 2012. **7**(2): p. e30905.

79. Han, M., et al., *MiR-21 regulates epithelial-mesenchymal transition phenotype and hypoxia-inducible factor-1alpha expression in third-sphere forming breast cancer stem cell-like cells.* Cancer Sci, 2012. **103**(6): p. 1058-64.

80. Brennan, M.D., et al., *Oxygen control with microfluidics.* Lab Chip, 2014. **14**(22): p. 4305-18.

81. Kieninger, J., et al., *Microsensor systems for cell metabolism - from 2D culture to organ-on-chip.* Lab Chip, 2018. **18**(9): p. 1274-1291.

82. Oomen, P.E., M.D. Skolimowski, and E. Verpoorte, *Implementing oxygen control in chip-based cell and tissue culture systems.* Lab Chip, 2016. **16**(18): p. 3394-414.

83. Chen, Y.A., et al., *Generation of oxygen gradients in microfluidic devices for cell culture using spatially confined chemical reactions.* Lab on a Chip, 2011. **11**(21): p. 3626-3633.

84. Huh, D., et al., *A Human Disease Model of Drug Toxicity-Induced Pulmonary Edema in a Lung-on-a-Chip Microdevice.* Science Translational Medicine, 2012. **4**(159).

85. Khanal, G., et al., *Ischemia/reperfusion injury of primary porcine cardiomyocytes in a low-shear microfluidic culture and analysis device.* Analyst, 2011. **136**(17): p. 3519-26.

86. Xia, C. and N.X. Fang, *3D microfabricated bioreactor with capillaries.* Biomed Microdevices, 2009. **11**(6): p. 1309-15.

87. Allen, J.W. and S.N. Bhatia, *Formation of steady-state oxygen gradients in vitro: application to liver zonation.* Biotechnol Bioeng, 2003. **82**(3): p. 253-62.

88. Lo, J.F., E. Sinkala, and D.T. Eddington, *Oxygen gradients for open well cellular cultures via microfluidic substrates.* Lab Chip, 2010. **10**(18): p. 2394-401.

89. Bastarache, J.A., et al., *The alveolar epithelium can initiate the extrinsic coagulation cascade through expression of tissue factor.* Thorax, 2007. **62**(7): p. 608-616.

90. Fridovich, I., *The biology of oxygen radicals.* Science, 1978. **201**(4359): p. 875-80.

91. Burgess, K.A., et al., *Towards microfabricated biohybrid artificial lung modules for chronic respiratory support.* Biomed Microdevices, 2009. **11**(1): p. 117-27.

92. Huh, D., et al., *Reconstituting Organ-Level Lung Functions on a Chip.* Science, 2010. **328**(5986): p. 1662-1668.

93. Hassell, B.A., et al., *Human Organ Chip Models Recapitulate Orthotopic Lung Cancer Growth, Therapeutic Responses, and Tumor Dormancy In Vitro.* Cell Rep, 2017. **21**(2): p. 508-516.

94. Schurek, H.J., *[Kidney medullary hypoxia: a key to understanding acute renal failure?].* Klin Wochenschr, 1988. **66**(18): p. 828-35.

95. Schurek, H.J., et al., *Evidence for a preglomerular oxygen diffusion shunt in rat renal cortex.* Am J Physiol, 1990. **259**(6 Pt 2): p. F910-5.

96. Welch, W.J., et al., *Nephron pO2 and renal oxygen usage in the hypertensive rat kidney.* Kidney Int, 2001. **59**(1): p. 230-7.

97. Brezis, M., et al., *Role of nitric oxide in renal medullary oxygenation. Studies in isolated and intact rat kidneys.* J Clin Invest, 1991. **88**(2): p. 390-5.

98. Kalogeris, T., et al., *Cell biology of ischemia/reperfusion injury.* Int Rev Cell Mol Biol, 2012. **298**: p. 229-317.

99. Blantz, R.C. and M.R. Weir, *Are the oxygen costs of kidney function highly regulated?* Current Opinion in Nephrology and Hypertension, 2004. **13**(1): p. 67-71.

100. Koivisto, A., et al., *Oxygen-dependent inhibition of respiration in isolated renal tubules by nitric oxide.* Kidney Int, 1999. **55**(6): p. 2368-75.

101. Vaziri, N.D., et al., *Oxidative stress and dysregulation of superoxide dismutase and NADPH oxidase in renal insufficiency.* Kidney Int, 2003. **63**(1): p. 179-85.

102. Greka, A. and P. Mundel, *Cell biology and pathology of podocytes.* Annu Rev Physiol, 2012. **74**: p. 299-323.

103. Musah, S., et al., *Mature induced-pluripotent-stem-cell-derived human podocytes reconstitute kidney glomerular-capillary-wall function on a chip.* Nat Biomed Eng, 2017. **1**.

104. Brukamp, K., et al., *Hypoxia and podocyte-specific Vhlh deletion confer risk of glomerular disease.* Am J Physiol Renal Physiol, 2007. **293**(4): p. F1397-407.

105. Freeburg, P.B., et al., *Podocyte expression of hypoxia-inducible factor (HIF)-1 and HIF-2 during glomerular development.* J Am Soc Nephrol, 2003. **14**(4): p. 927-38.

106. Kietzmann, T. and K. Jungermann, *Modulation by oxygen of zonal gene expression in liver studied in primary rat hepatocyte cultures.* Cell Biol Toxicol, 1997. **13**(4-5): p. 243-55.

107. Godoy, P., et al., *Recent advances in 2D and 3D in vitro systems using primary hepatocytes, alternative hepatocyte sources and non-parenchymal liver cells and their use in investigating mechanisms of hepatotoxicity, cell signaling and ADME.* Arch Toxicol, 2013. **87**(8): p. 1315-530.

108. Giffin, B.F., et al., *Hepatic Lobular Patterns of Phosphoenolpyruvate Carboxykinase, Glycogen-Synthase, and Glycogen-Phosphorylase in Fasted and Fed Rats.* Journal of Histochemistry & Cytochemistry, 1993. **41**(12): p. 1849-1862.

109. Bavli, D., et al., *Real-time monitoring of metabolic function in liver-on-chip microdevices tracks the dynamics of mitochondrial dysfunction.* Proceedings of the National Academy of Sciences of the United States of America, 2016. **113**(16): p. E2231-E2240.

110. Domansky, K., et al., *Perfused multiwell plate for 3D liver tissue engineering.* Lab on a Chip, 2010. **10**(1): p. 51-58.

111. Jungermann, K. and T. Kietzmann, *Oxygen: modulator of metabolic zonation and disease of the liver.* Hepatology, 2000. **31**(2): p. 255-60.

112. Vivares, A., et al., *Morphological behaviour and metabolic capacity of cryopreserved human primary hepatocytes cultivated in a perfused multiwell device.* Xenobiotica, 2015. **45**(1): p. 29-44.

113. Sarkar, U., et al., *Metabolite profiling and pharmacokinetic evaluation of hydrocortisone in a perfused three-dimensional human liver bioreactor.* Drug Metab Dispos, 2015. **43**(7): p. 1091-9.

114. Tsamandouras, N., et al., *Quantitative Assessment of Population Variability in Hepatic Drug Metabolism Using a Perfused Three-Dimensional Human Liver Microphysiological System.* J Pharmacol Exp Ther, 2017. **360**(1): p. 95-105.

115. Dash, A., et al., *Liver tissue engineering in the evaluation of drug safety.* Expert Opin Drug Metab Toxicol, 2009. **5**(10): p. 1159-74.

116. Du, Y., et al., *Mimicking liver sinusoidal structures and functions using a 3D-configured microfluidic chip.* Lab on a Chip, 2017. **17**(5): p. 782-794.

117. Black, A.F., et al., *In vitro reconstruction of a human capillary-like network in a tissue-engineered skin equivalent.* FASEB J, 1998. **12**(13): p. 1331-40.

118. Klar, A.S., et al., *Tissue-engineered dermo-epidermal skin grafts prevascularized with adipose-derived cells.* Biomaterials, 2014. **35**(19): p. 5065-78.

119. Marino, D., et al., *Bioengineering dermo-epidermal skin grafts with blood and lymphatic capillaries.* Sci Transl Med, 2014. **6**(221): p. 221ra14.

120. Tremblay, P.L., et al., *In vitro evaluation of the angiostatic potential of drugs using an endothelialized tissue-engineered connective tissue.* J Pharmacol Exp Ther, 2005. **315**(2): p. 510-6.

121. DiVito, K.A., et al., *Microfabricated blood vessels undergo neoangiogenesis.* Biomaterials, 2017. **138**: p. 142-152.

122. Truskey, G.A. and C.E. Fernandez, *Tissue-engineered blood vessels as promising tools for testing drug toxicity.* Expert Opin Drug Metab Toxicol, 2015. **11**(7): p. 1021-4.

123. Mori, N., Y. Morimoto, and S. Takeuchi, *Skin integrated with perfusable vascular channels on a chip.* Biomaterials, 2017. **116**: p. 48-56.

124. Atac, B., et al., *Skin and hair on-a-chip: in vitro skin models versus ex vivo tissue maintenance with dynamic perfusion.* Lab Chip, 2013. **13**(18): p. 3555-61.

125. Shepherd, B.R., et al., *Vascularization and engraftment of a human skin substitute using circulating progenitor cell-derived endothelial cells.* FASEB J, 2006. **20**(10): p. 1739-41.

126. Supp, D.M., K. Wilson-Landy, and S.T. Boyce, *Human dermal microvascular endothelial cells form vascular analogs in cultured skin substitutes after grafting to athymic mice.* FASEB J, 2002. **16**(8): p. 797-804.

127. Wufuer, M., et al., *Skin-on-a-chip model simulating inflammation, edema and drug-based treatment.* Sci Rep, 2016. **6**: p. 37471.

128. Gordon, L.I., et al., *Blockade of the erbB2 receptor induces cardiomyocyte death through mitochondrial and reactive oxygen species-dependent pathways.* J Biol Chem, 2009. **284**(4): p. 2080-7.

129. Ganitkevich, V., et al., *Dynamic responses of single cardiomyocytes to graded ischemia studied by oxygen clamp in on-chip picochambers.* Circ Res, 2006. **99**(2): p. 165-71.

130. McDougal, A.D. and C.F. Dewey, Jr., *Modeling oxygen requirements in ischemic cardiomyocytes.* J Biol Chem, 2017. **292**(28): p. 11760-11776.

131. Unterberg, C., et al., *Oxygen free radical damage of isolated cardiomyocytes: comparative protective effect of radical scavengers and calcium antagonists.* Basic Res Cardiol, 1992. **87**(2): p. 148-60.

132. Ellis, B.W., et al., *Human iPSC-derived myocardium-on-chip with capillary-like flow for personalized medicine.* Biomicrofluidics, 2017. **11**(2): p. 024105.

133. Lee, J.M., et al., *Brain tissue responses to ischemia.* J Clin Invest, 2000. **106**(6): p. 723-31.

134. Kristian, T., *Metabolic stages, mitochondria and calcium in hypoxic/ischemic brain damage.* Cell Calcium, 2004. **36**(3-4): p. 221-33.

135. Dirnagl, U., C. Iadecola, and M.A. Moskowitz, *Pathobiology of ischaemic stroke: an integrated view.* Trends Neurosci, 1999. **22**(9): p. 391-7.

136. Winquist, R.J. and S. Kerr, *Cerebral ischemia-reperfusion injury and adhesion.* Neurology, 1997. **49**(5 Suppl 4): p. S23-6.

137. Mauleon, G., C.P. Fall, and D.T. Eddington, *Precise spatial and temporal control of oxygen within in vitro brain slices via microfluidic gas channels.* PLoS One, 2012. **7**(8): p. e43309.

138. Peterson, B.L., et al., *Blunted neuronal calcium response to hypoxia in naked mole-rat hippocampus.* PLoS One, 2012. **7**(2): p. e31568.

139. Mauleon, G., et al., *Enhanced loading of Fura-2/AM calcium indicator dye in adult rodent brain slices via a microfluidic oxygenator.* J Neurosci Methods, 2013. **216**(2): p. 110-7.

140. Johnson, B.N., et al., *3D printed nervous system on a chip.* Lab Chip, 2016. **16**(8): p. 1393-400.

141. Aznavoorian, S., et al., *Signal transduction for chemotaxis and haptotaxis by matrix molecules in tumor cells.* J Cell Biol, 1990. **110**(4): p. 1427-38.

142. Tredan, O., et al., *Drug resistance and the solid tumor microenvironment.* J Natl Cancer Inst, 2007. **99**(19): p. 1441-54.

143. Acosta, M.A., et al., *A microfluidic device to study cancer metastasis under chronic and intermittent hypoxia.* Biomicrofluidics, 2014. **8**(5).

144. Funamoto, K., et al., *A novel microfluidic platform for high-resolution imaging of a three-dimensional cell culture under a controlled hypoxic environment.* Lab Chip, 2012. **12**(22): p. 4855-63.

145. Lewis, D.M., et al., *Intratumoral oxygen gradients mediate sarcoma cell invasion.* Cancer Research, 2017. **77**.

146. Lewis, D.M.T., V.; Jain, N.; Isser, A.; Xia, Z.; Gerecht, S., *Collagen Fiber Architecture Regulates Hypoxia Sarcoma Cell Migration.* ACS Biomaterials Science and Engineering, 2017: p. 10.

147. Lewis, D.M., et al., *O2-controllable hydrogels for studying cellular responses to hypoxic gradients in three dimensions in vitro and in vivo.* Nat Protoc, 2017. **12**(8): p. 1620-1638.

148. Abaci, H.E., et al., *Unforeseen decreases in dissolved oxygen levels affect tube formation kinetics in collagen gels.* Am J Physiol Cell Physiol, 2011. **301**(2): p. C431-40.

149. Colgan, S.P. and C.T. Taylor, *Hypoxia: an alarm signal during intestinal inflammation.* Nat Rev Gastroenterol Hepatol, 2010. **7**(5): p. 281-7.

150. Bohlen, H.G., *Intestinal tissue PO2 and microvascular responses during glucose exposure.* Am J Physiol, 1980. **238**(2): p. H164-71.

151. Turner, J.R., *Intestinal mucosal barrier function in health and disease.* Nat Rev Immunol, 2009. **9**(11): p. 799-809.

152. Kim, H.J., et al., *Human gut-on-a-chip inhabited by microbial flora that experiences intestinal peristalsis-like motions and flow.* Lab Chip, 2012. **12**(12): p. 2165-74.

153. Kim, H.J., et al., *Co-culture of Living Microbiome with Microengineered Human Intestinal Villi in a Gut-on-a-Chip Microfluidic Device.* J Vis Exp, 2016(114).

154. Shah, P., et al., *A microfluidics-based in vitro model of the gastrointestinal human-microbe interface.* Nat Commun, 2016. **7**: p. 11535.

155. Kim, H.J., et al., *Contributions of microbiome and mechanical deformation to intestinal bacterial overgrowth and inflammation in a human gut-on-a-chip.* Proc Natl Acad Sci U S A, 2016. **113**(1): p. E7-15.

156. Artursson, P., K. Palm, and K. Luthman, *Caco-2 monolayers in experimental and theoretical predictions of drug transport.* Adv Drug Deliv Rev, 2001. **46**(1-3): p. 27-43.

157. Mehta, G., et al., *Quantitative measurement and control of oxygen levels in microfluidic poly(dimethylsiloxane) bioreactors during cell culture.* Biomedical Microdevices, 2007. **9**(2): p. 123-134.

158. Duffy, D.C., et al., *Rapid Prototyping of Microfluidic Systems in Poly(dimethylsiloxane).* Anal Chem, 1998. **70**(23): p. 4974-84.

159. Merkel, T.C., et al., *Gas sorption, diffusion, and permeation in poly(dimethylsiloxane).* Journal of Polymer Science Part B-Polymer Physics, 2000. **38**(3): p. 415-434.

160. Toepke, M.W. and D.J. Beebe, *PDMS absorption of small molecules and consequences in microfluidic applications.* Lab Chip, 2006. **6**(12): p. 1484-6.

161. Regehr, K.J., et al., *Biological implications of polydimethylsiloxane-based microfluidic cell culture.* Lab Chip, 2009. **9**(15): p. 2132-9.

162. Domansky, K., et al., *Clear castable polyurethane elastomer for fabrication of microfluidic devices.* Lab Chip, 2013. **13**(19): p. 3956-64.

163. Olah, A., H. Hillborg, and G.J. Vancso, *Hydrophobic recovery of UV/ozone treated poly(dimethylsiloxane): adhesion studies by contact mechanics and mechanism of surface modification.* Applied Surface Science, 2005. **239**(3-4): p. 410-423.

164. Gao, Y.P., et al., *Activation Barriers for Oxygen Diffusion in Polystyrene and Polycarbonate Glasses - Effects of Low-Molecular-Weight Additives.* Macromolecules, 1994. **27**(24): p. 7041-7048.

165. Ramsey, W.S., et al., *Surface treatments and cell attachment.* In Vitro, 1984. **20**(10): p. 802-8.

166. Amstein, C.F. and P.A. Hartman, *Adaptation of plastic surfaces for tissue culture by glow discharge.* J Clin Microbiol, 1975. **2**(1): p. 46-54.

167. Trinh, K.T.L.C., N.M.; Lee, N.Y., *Fabrication of an integrated polystyrene microdevice for pre-concentration and amplification of Escherichia coli O157:H7 from raw milk.* Anal. Methods, 2018.

168. Barbari, T.A., W.J. Koros, and D.R. Paul, *Gas-Transport in Polymers Based on Bisphenol-A.* Journal of Polymer Science Part B-Polymer Physics, 1988. **26**(4): p. 709-727.

169. Oppegard, S.C., et al., *Precise control over the oxygen conditions within the Boyden chamber using a microfabricated insert.* Lab Chip, 2010. **10**(18): p. 2366-73.

170. Rowe, L., et al., *Active 3-D microscaffold system with fluid perfusion for culturing in vitro neuronal networks.* Lab Chip, 2007. **7**(4): p. 475-82.

171. Chang, T.Y., et al., *Cell and protein compatibility of parylene-C surfaces.* Langmuir, 2007. **23**(23): p. 11718-25.

172. Hoshino, T., et al., *Improvement of neuronal cell adhesiveness on parylene with oxygen plasma treatment.* J Biosci Bioeng, 2012. **113**(3): p. 395-8.

173. Trantidou, T., et al., *Selective hydrophilic modification of Parylene C films: a new approach to cell micro-patterning for synthetic biology applications.* Biofabrication, 2014. **6**(2): p. 025004.

174. Klinger, M., et al., *Effect of Polymer Cross-Links on Oxygen Diffusion in Glassy PMMA Films.* Acs Applied Materials & Interfaces, 2009. **1**(3): p. 661-667.

175. Abaci, H.E., et al., *Design and development of microbioreactors for long-term cell culture in controlled oxygen microenvironments.* Biomed Microdevices, 2012. **14**(1): p. 145-52.

176. Polinkovsky, M., et al., *Fine temporal control of the medium gas content and acidity and on-chip generation of series of oxygen concentrations for cell cultures.* Lab Chip, 2009. **9**(8): p. 1073-84.

177. Skolimowski, M., et al., *Microfluidic dissolved oxygen gradient generator biochip as a useful tool in bacterial biofilm studies.* Lab on a Chip, 2010. **10**(16): p. 2162-2169.

178. Weltin, A., et al., *Cell culture monitoring for drug screening and cancer research: a transparent, microfluidic, multi-sensor microsystem.* Lab Chip, 2014. **14**(1): p. 138-46.

179. Day, D. and M. Gu, *Microchannel fabrication in PMMA based on localized heating by nanojoule high repetition rate femtosecond pulses.* Opt Express, 2005. **13**(16): p. 5939-46.

180. Frazer, R.Q., et al., *PMMA: an essential material in medicine and dentistry.* J Long Term Eff Med Implants, 2005. **15**(6): p. 629-39.

181. Klank, H., J.P. Kutter, and O. Geschke, *CO(2)-laser micromachining and back-end processing for rapid production of PMMA-based microfluidic systems.* Lab Chip, 2002. **2**(4): p. 242-6.

182. Yao, L., et al., *Micro flow-through PCR in a PMMA chip fabricated by KrF excimer laser.* Biomed Microdevices, 2005. **7**(3): p. 253-7.

183. Rivera, K.R., et al., *Integrated phosphorescence-based photonic biosensor (iPOB) for monitoring oxygen levels in 3D cell culture systems. Manuscript submitted for publication.* Biosens Bioelectron, 2018.

184. de Jong, J., et al., *New replication technique for the fabrication of thin polymeric microfluidic devices with tunable porosity.* Lab Chip, 2005. **5**(11): p. 1240-7.

185. Park, K.M. and S. Gerecht, *Hypoxia-inducible hydrogels.* Nat Commun, 2014. **5**: p. 4075.

186. Oppegard, S.C. and D.T. Eddington, *A microfabricated platform for establishing oxygen gradients in 3-D constructs.* Biomed Microdevices, 2013. **15**(3): p. 407-14.

187. Adler, M., et al., *Generation of oxygen gradients with arbitrary shapes in a microfluidic device.* Lab Chip, 2010. **10**(3): p. 388-91.

188. Adler, M., et al., *Studies of bacterial aerotaxis in a microfluidic device.* Lab Chip, 2012. **12**(22): p. 4835-47.

189. Vollmer, A.P., et al., *Development of an integrated microfluidic platform for dynamic oxygen sensing and delivery in a flowing medium.* Lab on a Chip, 2005. **5**(10): p. 1059-1066.

190. Aitken, C.E., R.A. Marshall, and J.D. Puglisi, *An oxygen scavenging system for improvement of dye stability in single-molecule fluorescence experiments.* Biophys J, 2008. **94**(5): p. 1826-35.

191. Wang, L., et al., *Construction of oxygen and chemical concentration gradients in a single microfluidic device for studying tumor cell-drug interactions in a dynamic hypoxia microenvironment.* Lab Chip, 2013. **13**(4): p. 695-705.

192. Reist, M., et al., *Toxic effects of sulphite in combination with peroxynitrite on neuronal cells.* J Neurochem, 1998. **71**(6): p. 2431-8.

193. Mathur, A., et al., *Human iPSC-based cardiac microphysiological system for drug screening applications.* Sci Rep, 2015. **5**: p. 8883.

194. Allen, J.W., S.R. Khetani, and S.N. Bhatia, *In vitro zonation and toxicity in a hepatocyte bioreactor.* Toxicol Sci, 2005. **84**(1): p. 110-9.

195. Kamholz, A.E. and P. Yager, *Theoretical analysis of molecular diffusion in pressure-driven laminar flow in microfluidic channels.* Biophys J, 2001. **80**(1): p. 155-60.

196. Pera-Titus, M., et al., *Direct volumetric measurement of gas oversolubility in nanoliquids: beyond Henry's law.* Chemphyschem, 2009. **10**(12): p. 2082-9.

197. Foy, B.D., et al., *A device to measure the oxygen uptake rate of attached cells: importance in bioartificial organ design.* Cell Transplant, 1994. **3**(6): p. 515-27.

198. Gracz, A.D., et al., *A high-throughput platform for stem cell niche co-cultures and downstream gene expression analysis.* Nat Cell Biol, 2015. **17**(3): p. 340-9.

199. Lee-Montiel, F.T., et al., *Control of oxygen tension recapitulates zone-specific functions in human liver microphysiology systems.* Exp Biol Med (Maywood), 2017. **242**(16): p. 1617-1632.

200. Shuk, P. and R. Jantz, *Oxygen Gas Sensing Technologies: A Comprehensive Review.* 2015 9th International Conference on Sensing Technology (Icst), 2015: p. 12-17.

201. Eguchi, T., *Short review: Design guide of sensing electrode for realizing fast response of the ambient temperature solid-state oxygen sensor.* Electrochemistry, 1999. **67**(7): p. 819-819.

202. Hauser, C.J., et al., *Visceral surface oxygen tension in experimental colitis in the rabbit.* J Lab Clin Med, 1988. **112**(1): p. 68-71.

203. Sheridan, W.G., R.H. Lowndes, and H.L. Young, *Intraoperative tissue oximetry in the human gastrointestinal tract.* Am J Surg, 1990. **159**(3): p. 314-9.

204. Cooper, G.J., K.M. Sherry, and J.A. Thorpe, *Changes in gastric tissue oxygenation during mobilisation for oesophageal replacement.* Eur J Cardiothorac Surg, 1995. **9**(3): p. 158-60; discussion 160.

205. He, G., et al., *Noninvasive measurement of anatomic structure and intraluminal oxygenation in the gastrointestinal tract of living mice with spatial and spectral EPR imaging.* Proc Natl Acad Sci U S A, 1999. **96**(8): p. 4586-91.

206. Albenberg, L., et al., *Correlation between intraluminal oxygen gradient and radial partitioning of intestinal microbiota.* Gastroenterology, 2014. **147**(5): p. 1055-63 e8.

207. Ramamoorthy, R., P.K. Dutta, and S.A. Akbar, *Oxygen sensors: Materials, methods, designs and applications.* Journal of Materials Science, 2003. **38**(21): p. 4271-4282.

208. Yi, C., et al., *Optical and electrochemical detection techniques for cell-based microfluidic systems.* Anal Bioanal Chem, 2006. **384**(6): p. 1259-68.

209. Wang, X.D. and O.S. Wolfbeis, *Optical methods for sensing and imaging oxygen: materials, spectroscopies and applications.* Chemical Society Reviews, 2014. **43**(10): p. 3666-3761.

210. Grist, S.M., L. Chrostowski, and K.C. Cheung, *Optical Oxygen Sensors for Applications in Microfluidic Cell Culture.* Sensors, 2010. **10**(10): p. 9286-9316.

211. Helm, I., et al., *Comparative validation of amperometric and optical analyzers of dissolved oxygen: a case study.* Environmental Monitoring and Assessment, 2018. **190**(5).

212. Feng, Y., et al., *Ratiometric optical oxygen sensing: a review in respect of material design.* Analyst, 2012. **137**(21): p. 4885-4901.

213. Akmal, N. and J. Lauer, *Electrochemical oxygen sensors: Principles and applications.* Polymers in Sensors, 1998. **690**: p. 149-160.

214. Pham, A.Q. and R.S. Glass, *Characteristics of the amperometric oxygen sensor.* Journal of the Electrochemical Society, 1997. **144**(11): p. 3929-3934.

215. Martinez-Manez, R., et al., *New potentiometric dissolved oxygen sensors in thick film technology.* Sensors and Actuators B: Chemical, 2004. **101**(3): p. 295-301.

216. Zimmermann, P., et al., *Active Potentiometry for Dissolved Oxygen Monitoring with Platinum Electrodes.* Sensors, 2018. **18**(8).

217. Ramamoorthy, R., S.A. Akbar, and P.K. Dutta, *Dependence of potentiometric oxygen sensing characteristics on the nature of electrodes.* Sensors and Actuators B-Chemical, 2006. **113**(1): p. 162-168.

218. Maskell, W.C. and B.C.H. Steele, *Solid-State Potentiometric Oxygen Gas Sensors.* Journal of Applied Electrochemistry, 1986. **16**(4): p. 475-489.

219. Hahn, P.B., et al., *Sodium Tungsten Bronze as a Potentiometric Indicating Electrode for Dissolved-Oxygen in Aqueous-Solution.* Analytical Chemistry, 1973. **45**(7): p. 1016-1021.

220. Yim, H.S. and M.E. Meyerhoff, *Reversible Potentiometric Oxygen Sensors Based on Polymeric and Metallic Film Electrodes.* Analytical Chemistry, 1992. **64**(17): p. 1777-1784.

221. Meruva, R.K. and M.E. Meyerhoff, *Catheter-Type sensor for potentiometric monitoring of oxygen, pH and carbon dioxide.* Biosensors & Bioelectronics, 1998. **13**(2): p. 201-212.

222. Li, M., et al., *Improved Potentiometric and Optic Sensitivity of Polyaniline Film to Dissolved Oxygen by Incorporating Iron-Porphyrin.* Electroanalysis, 2015. **27**(6): p. 1427-1435.

223. Linsenmeier, R.A. and C.M. Yancey, *Improved Fabrication of Double-Barreled Recessed Cathode O2 Microelectrodes.* Journal of Applied Physiology, 1987. **63**(6): p. 2554-2557.

224. Gao, C., et al., *A fully integrated biosensor array for measurement of metabolic parameters in human blood.* 2nd Annual International Ieee-Embs Special Topic Conference on Microtechnologies in Medicine & Biology, Proceedings, 2002: p. 223-226.

225. Park, J., Y.K. Pak, and J.J. Pak, *A microfabricated reservoir-type oxygen sensor for measuring the real-time cellular oxygen consumption rate at various conditions.* Sensors and Actuators B-Chemical, 2010. **147**(1): p. 263-269.

226. Mitrovski, S.M. and R.G. Nuzzo, *An electrochemically driven poly(dimethylsiloxane) microfluidic actuator: oxygen sensing and programmable flows and pH gradients.* Lab on a Chip, 2005. **5**(6): p. 634-645.

227. Clark, L.C., et al., *Continuous Recording of Blood Oxygen Tensions by Polarography.* Journal of Applied Physiology, 1953. **6**(3): p. 189-193.

228. Lee, J.H., et al., *Needle-type dissolved oxygen microelectrode array sensors for in situ measurements.* Sensors and Actuators B-Chemical, 2007. **128**(1): p. 179-185.

229. Wu, C.C., et al., *A Clark-type oxygen chip for in situ estimation of the respiratory activity of adhering cells.* Talanta, 2010. **81**(1-2): p. 228-234.

230. Khine, M., et al., *A combined neural-oxygen sensing multi-channel electrode array.* 1st International Ieee Embs Conference on Neural Engineering 2003, Conference Proceedings, 2003: p. 204-207.

231. Luo, J., T. Dziubla, and R. Eitel, *A low temperature co-fired ceramic based microfluidic Clark-type oxygen sensor for real-time oxygen sensing.* Sensors and Actuators B-Chemical, 2017. **240**: p. 392-397.

232. Suzuki, H., et al., *Development of a Miniature Clark-Type Oxygen-Electrode Using Semiconductor Techniques and Its Improvement for Practical Applications.* Sensors and Actuators B-Chemical, 1990. **2**(3): p. 185-191.

233. Suzuki, H., A. Sugama, and N. Kojima, *Effect of Anode Materials on the Characteristics of the Miniature Clark-Type Oxygen-Electrode.* Analytica Chimica Acta, 1990. **233**(2): p. 275-280.

234. Suzuki, H., et al., *A Miniature Clark-Type Oxygen-Electrode Using a Polyelectrolyte and Its Application as a Glucose Sensor.* Biosensors & Bioelectronics, 1991. **6**(5): p. 395-400.

235. Wu, C.C., et al., *Fabrication of miniature Clark oxygen sensor integrated with microstructure.* Sensors and Actuators B-Chemical, 2005. **110**(2): p. 342-349.

236. Yamagishi, A., et al., *Microfluidic device coupled with a microfabricated oxygen electrode for the measurement of bactericidal activity of neutrophil-like cells.* Analytica Chimica Acta, 2017. **985**: p. 1-6.

237. Suzuki, H.S., A.; Kojima, N., *Miniature Clark-type oxygen electrode with a three-electrode configuration.* Sensors and Actuators B-Chemical, 1990. **2**(4): p. 297-303.

238. Park, J., Youngmi, K.P., James J.P., *A microfabricated reservoir-type oxygen sensor for measuring the real-time cellular oxygen consumption rate at various conditions.* Sensors and Actuators B: Chemical, 2010. **147**(1): p. 263-269.

239. Date, Y., et al., *Monitoring oxygen consumption of single mouse embryos using an integrated electrochemical microdevice.* Biosensors & Bioelectronics, 2011. **30**(1): p. 100-106.

240. Amatore, C., et al., *Electrochemical detection in a microfluidic device of oxidative stress generated by macrophage cells.* Lab on a Chip, 2007. **7**(2): p. 233-238.

241. Kieninger, J., et al., *Pericellular oxygen monitoring with integrated sensor chips for reproducible cell culture experiments.* Cell Proliferation, 2014. **47**(2): p. 180-188.

242. Kieninger, J., et al., *Amperometric oxygen sensor array with novel chronoamperometric protocols for hypoxic tumor cell cultures.* Transducers '07 & Eurosensors Xxi, Digest of Technical Papers, Vols 1 and 2, 2007.

243. Park, J.H., et al., *Electrochemical sensing of high density photosynthetic cells using a microfluidic chip.* Sensors and Actuators B-Chemical, 2013. **188**: p. 1300-1305.

244. Demuth, C., et al., *Novel probes for pH and dissolved oxygen measurements in cultivations from millilitre to benchtop scale.* Applied Microbiology and Biotechnology, 2016. **100**(9): p. 3853-3863.

245. Brischwein, M., et al., *Functional cellular assays with multiparametric silicon sensor chips.* Lab on a Chip, 2003. **3**(4): p. 234-240.

246. Ahn, C.H., et al., *Disposable Smart lab on a chip for point-of-care clinical diagnostics.* Proceedings of the Ieee, 2004. **92**(1): p. 154-173.

247. Clark, L.C. and E.W. Clark, *A Personalized History of the Clark Oxygen-Electrode.* International Anesthesiology Clinics, 1987. **25**(3): p. 1-29.

248. Azad, A.M., et al., *Solid-State Gas Sensors - a Review.* Journal of the Electrochemical Society, 1992. **139**(12): p. 3690-3704.

249. Fratoddi, I., et al., *Chemiresistive polyaniline-based gas sensors: A mini review.* Sensors and Actuators B-Chemical, 2015. **220**: p. 534-548.

250. Llobet, E., *Gas sensors using carbon nanomaterials: A review.* Sensors and Actuators B-Chemical, 2013. **179**: p. 32-45.

251. Stetter, J.R. and J. Li, *Amperometric gas sensors--a review.* Chem Rev, 2008. **108**(2): p. 352-66.

252. Glasspool, W. and J. Atkinson, *A screen-printed amperometric dissolved oxygen sensor utilising an immobilised electrolyte gel and membrane.* Sensors and Actuators B-Chemical, 1998. **48**(1-3): p. 308-317.

253. Wang, P., et al., *Micromachined dissolved oxygen sensor based on solid polymer electrolyte.* Sensors and Actuators B-Chemical, 2011. **153**(1): p. 145-151.

254. Zhang, H., et al., *Electrochemical Oxygen Sensor Based on the Interaction of Double-Layer Ionic Liquid Film (DLILF).* Journal of the Electrochemical Society, 2018. **165**(16): p. B779-B786.

255. Moya, A., et al., *Flexible Microfluidic Bio-Lab-on-a-Chip Multi-Sensor Platform for Electrochemical Measurements.* 2014 Ieee Sensors, 2014.

256. Rodrigues, N.P., Y. Sakai, and T. Fujii, *Cell-based microfluidic biochip for the electrochemical real-time monitoring of glucose and oxygen.* Sensors and Actuators B-Chemical, 2008. **132**(2): p. 608-613.

257. Choi, S.H., et al., *Planar amperometric oxygen sensor with improved preconditioning property.* Analytica Chimica Acta, 2001. **431**(2): p. 261-267.

258. Severinghaus, J.W. and A.F. Bradley, *Electrodes for blood pO2 and pCO2 determination.* J Appl Physiol, 1958. **13**(3): p. 515-20.

259. Arquint, P., et al., *Integrated Blood-Gas Sensor for Po2, Pco2 and Ph.* Sensors and Actuators B-Chemical, 1993. **13**(1-3): p. 340-344.

260. Ratner, B.D. and I.F. Miller, *Transport through Crosslinked Poly(2-Hydroxyethyl Methacrylate) Hydrogel Membranes.* Journal of Biomedical Materials Research, 1973. **7**(4): p. 353-367.

261. Naylor, P.F.D. and N.T.S. Evans, *Polystyrene Membranes for Covering Oxygen Electrodes for Use in Tissue.* Nature, 1963. **199**(489): p. 911-&.

262. Rumsey, W.L., J.M. Vanderkooi, and D.F. Wilson, *Imaging of Phosphorescence - a Novel Method for Measuring Oxygen Distribution in Perfused Tissue.* Science, 1988. **241**(4873): p. 1649-1651.

263. Bergman, I., *Rapid-Response Atmospheric Oxygen Monitor Based on Fluorescence Quenching.* Nature, 1968. **218**(5139): p. 396-&.

264. Wolfbeis, O.S., *Luminescent sensing and imaging of oxygen: fierce competition to the Clark electrode.* Bioessays, 2015. **37**(8): p. 921-8.

265. Sud, D., et al., *Optical imaging in microfluidic bioreactors enables oxygen monitoring for continuous cell culture.* Journal of Biomedical Optics, 2006. **11**(5).

266. Deepa, N. and A.B. Ganesh, *Sol-gel based portable optical sensor for simultaneous and minimal invasive measurement of pH and dissolved oxygen.* Measurement, 2015. **59**: p. 337-343.

267. Lin, Z., et al., *In-situ measurement of cellular microenvironments in a microfluidic device.* Lab on a Chip, 2009. **9**(2): p. 257-262.

268. Sin, A., et al., *The design and fabrication of three-chamber microscale cell culture analog devices with integrated dissolved oxygen sensors.* Biotechnology Progress, 2004. **20**(1): p. 338-345.

269. Acosta, M.A., et al., *Fluorescent microparticles for sensing cell microenvironment oxygen levels within 3D scaffolds.* Biomaterials, 2009. **30**(17): p. 3068-3074.

270. Lambrechts, D., et al., *Fluorescent oxygen sensitive microbead incorporation for measuring oxygen tension in cell aggregates.* Biomaterials, 2013. **34**(4): p. 922-9.

271. Chang-Yen, D.A., et al., *Electrostatic self-assembly of a ruthenium-based oxygen sensitive dye using polyion-dye interpolyelectrolyte formation.* Sensors and Actuators B-Chemical, 2002. **87**(2): p. 336-345.

272. Mehta, G., et al., *Hard Top Soft Bottom Microfluidic Devices for Cell Culture and Chemical Analysis.* Analytical Chemistry, 2009. **81**(10): p. 3714-3722.

273. Mills, A. and A. Lepre, *Controlling the response characteristics of luminescent porphyrin plastic film sensors for oxygen.* Analytical Chemistry, 1997. **69**(22): p. 4653-4659.

274. Papkovsky, D.B. and T.C. O'Riordan, *Emerging applications of phosphorescent metalloporphyrins.* Journal of Fluorescence, 2005. **15**(4): p. 569-584.

275. Gitlin, L., et al., *Micro flow reactor chips with integrated luminescent chemosensors for spatially resolved on-line chemical reaction monitoring.* Lab on a Chip, 2013. **13**(20): p. 4134-4141.

276. Grist, S.M., et al., *Designing a Microfluidic Device with Integrated Ratiometric Oxygen Sensors for the Long-Term Control and Monitoring of Chronic and Cyclic Hypoxia.* Sensors, 2015. **15**(8): p. 20030-20052.

277. Thomas, P.C., S.R. Raghavan, and S.P. Forry, *Regulating oxygen levels in a microfluidic device.* Anal Chem, 2011. **83**(22): p. 8821-4.

278. Ungerbock, B., et al., *Microfluidic oxygen imaging using integrated optical sensor layers and a color camera.* Lab on a Chip, 2013. **13**(8): p. 1593-1601.

279. Ehgartner, J., et al., *Online analysis of oxygen inside silicon-glass microreactors with integrated optical sensors.* Sensors and Actuators B-Chemical, 2016. **228**: p. 748-757.

280. Sato, A., et al., *An in vitro hepatic zonation model with a continuous oxygen gradient in a microdevice.* Biochemical and Biophysical Research Communications, 2014. **453**(4): p. 767-771.

281. Lee, H.L.T., et al., *Microbioreactor arrays with integrated mixers and fluid injectors for high-throughput experimentation with pH and dissolved oxygen control.* Lab on a Chip, 2006. **6**(9): p. 1229-1235.

282. Lasave, L.C., et al., *Quick and simple integration of optical oxygen sensors into glass-based microfluidic devices.* Rsc Advances, 2015. **5**(87): p. 70808-70816.

283. John, G.T., et al., *Integrated optical sensing of dissolved oxygen in microtiter plates: A novel tool for microbial cultivation.* Biotechnology and Bioengineering, 2003. **81**(7): p. 829-836.

284. Hartmann, P. and W. Trettnak, *Effects of polymer matrices on calibration functions of luminescent oxygen sensors based on porphyrin ketone complexes.* Analytical Chemistry, 1996. **68**(15): p. 2615-2620.

285. Amao, Y., *Probes and polymers for optical sensing of oxygen.* Microchimica Acta, 2003. **143**(1): p. 1-12.

286. Pfeiffer, S.A. and S. Nagl, *Microfluidic platforms employing integrated fluorescent or luminescent chemical sensors: a review of methods, scope and applications.* Methods and Applications in Fluorescence, 2015. **3**(3).

287. Nourmohammadzadeh, M., et al., *Microfluidic Array with Integrated Oxygenation Control for Real-Time Live-Cell Imaging: Effect of Hypoxia on Physiology of Microencapsulated Pancreatic Islets.* Analytical Chemistry, 2013. **85**(23): p. 11240-11249.

288. Carter, W.O., P.K. Narayanan, and J.P. Robinson, *Intracellular hydrogen peroxide and superoxide anion detection in endothelial cells.* J Leukoc Biol, 1994. **55**(2): p. 253-8.

289. Oppegard, S.C. and D.T. Eddington, *Device for the control of oxygen concentration in multiwell cell culture plates.* Conf Proc IEEE Eng Med Biol Soc, 2009. **2009**: p. 2097-100.

290. Oppegard, S.C., et al., *Modulating temporal and spatial oxygenation over adherent cellular cultures.* PLoS One, 2009. **4**(9): p. e6891.

291. Ochs, C.J., et al., *Oxygen levels in thermoplastic microfluidic devices during cell culture.* Lab on a Chip, 2014. **14**(3): p. 459-462.

292. Hartmann, P., et al., *Oxygen flux fluorescence lifetime imaging.* Sensors and Actuators B-Chemical, 1997. **38**(1-3): p. 110-115.

293. Lakowicz, J.R., *Principle of fluorescence spectroscopy*, in *Principle of fluorescence spectroscopy*. 2006, Springer US. p. 99.

294. Liebsch, G., et al., *Luminescence lifetime imaging of oxygen, pH, and carbon dioxide distribution using optical sensors.* Applied Spectroscopy, 2000. **54**(4): p. 548-559.

295. Leong, J.X.W.D., W. R.; Ghasemi, M.; Ahmad, A.; Ismail, M.; Liew, K. B., *Composite membrane containing graphene oxide in sulfonated polyether ether ketone in microbial fuel cell applications.* International Journal of Hydrogen Energy, 2015. **40**(35): p. 11604-11614.

296. Koros, W.J.W., J.; Felder, R. M., *Oxygen permeation through FEP Teflon and Kapton polyimide.* Journal of Applied Polymer Science, 1981. **26**(8): p. 2805–2809.

297. Mirzadeh, A.K., M., *The effect of composition and draw-down ratio on morphology and oxygen permeability of polypropylene nanocomposite blown films.* European Polymer Journal, 2007. **43**(9): p. 3757-3765.

298. Chen, S.A.J., H.L., *Permeation of Oxygen Through Polyurethane-Polyepoxide Interpenetrating Polymer Networks.* Journal of Applied Polymer Science, 1980. **25**: p. 1105-1116.

299. Orchard, G.A.J.S., P.; Ward, I. M., *Oxygen and water-vapor diffusion through biaxially oriented poly(ethylene terephthalate).* Journal of Polymer Science Part B-Polymer Physics, 1990. **28**(5): p. 603–621.

300. Zanzotto, A., et al., *Membrane-aerated microbioreactor for high-throughput bioprocessing.* Biotechnol Bioeng, 2004. **87**(2): p. 243-54.

301. Sin, A., et al., *The design and fabrication of three-chamber microscale cell culture analog devices with integrated dissolved oxygen sensors.* Biotechnol Prog, 2004. **20**(1): p. 338-45.

302. Zhang, Y.S., et al., *A cost-effective fluorescence mini-microscope for biomedical applications.* Lab Chip, 2015. **15**(18): p. 3661-9.

303. Nourmohammadzadeh, M., et al., *Microfluidic array with integrated oxygenation control for real-time live-cell imaging: effect of hypoxia on physiology of microencapsulated pancreatic islets.* Anal Chem, 2013. **85**(23): p. 11240-9.

304. Gitlin, L., et al., *Micro flow reactor chips with integrated luminescent chemosensors for spatially resolved on-line chemical reaction monitoring.* Lab Chip, 2013. **13**(20): p. 4134-41.

305. Cooper, P.D., A.M. Burt, and J.N. Wilson, *Critical effect of oxygen tension on rate of growth of animal cells in continuous suspended culture.* Nature, 1958. **182**(4648): p. 1508-9.

306. Lind Due, V., et al., *Extremely low oxygen tension in the rectal lumen of human subjects.* Acta Anaesthesiol Scand, 2003. **47**(3): p. 372.

307. Hashimoto, H., *Study for Germination under Oxygen Partial Pressure of 1 kPa.* Origins of Life and Evolution of Biospheres, 2010. **40**(6): p. 568-568.

308. Saglio, P.H., M.C. Drew, and A. Pradet, *Metabolic Acclimation to Anoxia Induced by Low (2-4 Kpa Partial-Pressure) Oxygen Pretreatment (Hypoxia) in Root-Tips of Zea-Mays.* Plant Physiology, 1988. **86**(1): p. 61-66.

309. Evans, S.M., et al., *Detection of hypoxia in human squamous cell carcinoma by EF5 binding.* Cancer Research, 2000. **60**(7): p. 2018-2024.

310. Aquino-Parsons, C., et al., *Comparison between the comet assay and the oxygen microelectrode for measurement of tumor hypoxia.* Radiotherapy and Oncology, 1999. **51**(2): p. 179-185.

311. Matsumura, T., et al., *O-2 Uptake in Periportal and Pericentral Regions of Liver Lobule in Perfused Liver.* American Journal of Physiology, 1986. **250**(6): p. G800-G805.

312. Gabig, T.G., S.I. Bearman, and B.M. Babior, *Effects of Oxygen-Tension and Ph on the Respiratory Burst of Human-Neutrophils.* Blood, 1979. **53**(6): p. 1133-1139.

313. McKeown, S.R., *Defining normoxia, physoxia and hypoxia in tumours-implications for treatment response.* British Journal of Radiology, 2014. **87**(1035).

314. Chou, C.C. and R.W. Coatney, *Nutrient-induced changes in intestinal blood flow in the dog.* Br Vet J, 1994. **150**(5): p. 423-37.

315. Shephard, R.J., *The oxygen cost of breathing during vigorous exercise.* Q J Exp Physiol Cogn Med Sci, 1966. **51**(4): p. 336-50.

316. Ivanovic, Z., *Hypoxia or in situ normoxia: The stem cell paradigm.* J Cell Physiol, 2009. **219**(2): p. 271-5.

317. Richter, A., K.K. Sanford, and V.J. Evans, *Influence of oxygen and culture media on plating efficiency of some mammalian tissue cells.* J Natl Cancer Inst, 1972. **49**(6): p. 1705-12.

318. Toussaint, O., et al., *Artefactual effects of oxygen on cell culture models of cellular senescence and stem cell biology.* J Cell Physiol, 2011. **226**(2): p. 315-21.

319. Heathman, T.R., et al., *The translation of cell-based therapies: clinical landscape and manufacturing challenges.* Regen Med, 2015. **10**(1): p. 49-64.

320. Elliott, N.T. and F. Yuan, *A review of three-dimensional in vitro tissue models for drug discovery and transport studies.* J Pharm Sci, 2011. **100**(1): p. 59-74.

321. Kim, J.B., R. Stein, and M.J. O'Hare, *Three-dimensional in vitro tissue culture models of breast cancer-- a review.* Breast Cancer Res Treat, 2004. **85**(3): p. 281-91.

322. Nelson, C.M. and M.J. Bissell, *Modeling dynamic reciprocity: engineering three-dimensional culture models of breast architecture, function, and neoplastic transformation.* Semin Cancer Biol, 2005. **15**(5): p. 342-52.

323. Walsh, J.C., et al., *The clinical importance of assessing tumor hypoxia: relationship of tumor hypoxia to prognosis and therapeutic opportunities.* Antioxid Redox Signal, 2014. **21**(10): p. 1516-54.

324. Brizel, D.M., et al., *Tumor oxygenation predicts for the likelihood of distant metastases in human soft tissue sarcoma.* Cancer Res, 1996. **56**(5): p. 941-3.

325. Francis, P., et al., *Diagnostic and prognostic gene expression signatures in 177 soft tissue sarcomas: hypoxia-induced transcription profile signifies metastatic potential.* BMC Genomics, 2007. **8**: p. 73.

326. Jiang, B.H., et al., *Hypoxia-inducible factor 1 levels vary exponentially over a physiologically relevant range of O-2 tension.* American Journal of Physiology-Cell Physiology, 1996. **271**(4): p. C1172-C1180.

327. Semenza, G.L., *Vascular responses to hypoxia and ischemia.* Arterioscler Thromb Vasc Biol, 2010. **30**(4): p. 648-52.

328. Esteban, M.A. and P.H. Maxwell, *Manipulation of oxygen tensions for in vitro cell culture using a hypoxic workstation.* Expert Rev Proteomics, 2005. **2**(3): p. 307-14.

329. Post, D.E. and E.G. Van Meir, *A novel hypoxia-inducible factor (HIF) activated oncolytic adenovirus for cancer therapy.* Oncogene, 2003. **22**(14): p. 2065-72.

330. Wu, D. and P. Yotnda, *Induction and testing of hypoxia in cell culture.* J Vis Exp, 2011(54).

331. Byrne, M.B., et al., *Methods to study the tumor microenvironment under controlled oxygen conditions.* Trends Biotechnol, 2014. **32**(11): p. 556-563.

332. Wisniewski, N.A., et al., *Tissue-Integrating Oxygen Sensors: Continuous Tracking of Tissue Hypoxia.* Adv Exp Med Biol, 2017. **977**: p. 377-383.

333. Pauley, R.J., et al., *The MCF10 family of spontaneously immortalized human breast epithelial cell lines: models of neoplastic progression.* Eur J Cancer Prev, 1993. **2 Suppl 3**: p. 67-76.

334. Lasfargues, E.Y., W.G. Coutinho, and E.S. Redfield, *Isolation of two human tumor epithelial cell lines from solid breast carcinomas.* J Natl Cancer Inst, 1978. **61**(4): p. 967-78.

335. Lee, G.Y., et al., *Three-dimensional culture models of normal and malignant breast epithelial cells.* Nat Methods, 2007. **4**(4): p. 359-65.

336. Schneider, C.A., W.S. Rasband, and K.W. Eliceiri, *NIH Image to ImageJ: 25 years of image analysis.* Nat Methods, 2012. **9**(7): p. 671-5.

337. Livak, K.J. and T.D. Schmittgen, *Analysis of relative gene expression data using real-time quantitative PCR and the 2(-Delta Delta C(T)) Method.* Methods, 2001. **25**(4): p. 402-8.

338. Hsiao, S.T., et al., *Hypoxic conditioning enhances the angiogenic paracrine activity of human adipose-derived stem cells.* Stem Cells Dev, 2013. **22**(10): p. 1614-23.

339. Mathew, S.A., B. Chandravanshi, and R. Bhonde, *Hypoxia primed placental mesenchymal stem cells for wound healing.* Life Sci, 2017. **182**: p. 85-92.

340. Quinn, P., *Culture media, solutions, and systems in human ART*. 2014, Cambridge ; New York: Cambridge University Press. xi, 289 pages.

341. Lo, L.W., C.J. Koch, and D.F. Wilson, *Calibration of oxygen-dependent quenching of the phosphorescence of Pd-meso-tetra (4-carboxyphenyl) porphine: a phosphor with general*

application for measuring oxygen concentration in biological systems. Anal Biochem, 1996. **236**(1): p. 153-60.

342. Rumsey, W.L., J.M. Vanderkooi, and D.F. Wilson, *Imaging of phosphorescence: a novel method for measuring oxygen distribution in perfused tissue.* Science, 1988. **241**(4873): p. 1649-51.

343. Vinogradov, S. and D.F. Wilson, *Porphyrin Compounds for Imaging Tissue Oxygen*, U. States., Editor. 2002, The Trustees of the University of Pennsylvania.

344. Eastwood, D. and Gouterma.M, *Porphyrins .18. Luminescence of (Co), (Ni), Pd, Pt Complexes.* Journal of Molecular Spectroscopy, 1970. **35**(3): p. 359-&.

345. Montero-Baker, M.F., et al., *The First-in-Man "Si Se Puede" Study for the use of micro-oxygen sensors (MOXYs) to determine dynamic relative oxygen indices in the feet of patients with limb-threatening ischemia during endovascular therapy.* J Vasc Surg, 2015. **61**(6): p. 1501-9 e1.

346. Vanderkooi, J.M. and D.F. Wilson, *A new method for measuring oxygen concentration in biological systems.* Adv Exp Med Biol, 1986. **200**: p. 189-93.

347. Vinogradov, S.A., et al., *Oxygen distributions in tissue measured by phosphorescence quenching.* Adv Exp Med Biol, 2003. **510**: p. 181-5.

348. Wilson, D.F., et al., *Imaging oxygen pressure in the rodent retina by phosphorescence lifetime.* Adv Exp Med Biol, 2006. **578**: p. 119-24.

349. Einstein, A., *The motion of elements suspended in static liquids as claimed in the molecular kinetic theory of heat.* Annalen Der Physik, 1905. **17**(8): p. 549-560.

350. Einstein, A., *The theory of the Brownian Motion.* Annalen Der Physik, 1906. **19**(2): p. 371-381.

351. Einstein, A., *Theoretical remarks on the Brownian Motion.* Zeitschrift Fur Elektrochemie Und Angewandte Physikalische Chemie, 1907. **13**: p. 41-42.

352. Einstein, A., *Elementary theory of the Brownian motion.* Zeitschrift Fur Elektrochemie Und Angewandte Physikalische Chemie, 1908. **14**: p. 235-239.

353. von Smoluchowski, M., *The kinetic theory of Brownian molecular motion and suspensions.* Annalen Der Physik, 1906. **21**(14): p. 756-780.

354. van Stroe-Biezen, S.A.M., Everaerts, F.M., Janssen, L.J.J., Tacken, R.A., *Diffusion coefficients of oxygen, hydrogen peroxide and glucose in a hydrogel.* Analytica Chimica Acta, 1993. **273**(1-2): p. 553-560.

355. Braunstein, S., et al., *A hypoxia-controlled cap-dependent to cap-independent translation switch in breast cancer.* Mol Cell, 2007. **28**(3): p. 501-12.

356. Gabai, V.L., et al., *Heat shock transcription factor Hsf1 is involved in tumor progression via regulation of hypoxia-inducible factor 1 and RNA-binding protein HuR.* Mol Cell Biol, 2012. **32**(5): p. 929-40.

357. Bashari, M.H., et al., *Mcl-1 confers protection of Her2-positive breast cancer cells to hypoxia: therapeutic implications.* Breast Cancer Res, 2016. **18**(1): p. 26.

358. Chun, Y.S., P.S. Adusumilli, and Y. Fong, *Employing tumor hypoxia for oncolytic therapy in breast cancer.* J Mammary Gland Biol Neoplasia, 2005. **10**(4): p. 311-8.

359. Wigerup, C., S. Pahlman, and D. Bexell, *Therapeutic targeting of hypoxia and hypoxia-inducible factors in cancer.* Pharmacol Ther, 2016. **164**: p. 152-69.

360. Wang, G.L., et al., *Hypoxia-inducible factor 1 is a basic-helix-loop-helix-PAS heterodimer regulated by cellular O2 tension.* Proc Natl Acad Sci U S A, 1995. **92**(12): p. 5510-4.

361. Airley, R.E., et al., *GLUT-1 and CAIX as intrinsic markers of hypoxia in carcinoma of the cervix: relationship to pimonidazole binding.* Int J Cancer, 2003. **104**(1): p. 85-91.

362. Forsythe, J.A., et al., *Activation of vascular endothelial growth factor gene transcription by hypoxia-inducible factor 1.* Mol Cell Biol, 1996. **16**(9): p. 4604-13.

363. Ebert, B.L., J.D. Firth, and P.J. Ratcliffe, *Hypoxia and mitochondrial inhibitors regulate expression of glucose transporter-1 via distinct Cis-acting sequences.* J Biol Chem, 1995. **270**(49): p. 29083-9.

364. Kothari, S., et al., *BNIP3 plays a role in hypoxic cell death in human epithelial cells that is inhibited by growth factors EGF and IGF.* Oncogene, 2003. **22**(30): p. 4734-44.

365. Gradin, K., et al., *Functional interference between hypoxia and dioxin signal transduction pathways: competition for recruitment of the Arnt transcription factor.* Mol Cell Biol, 1996. **16**(10): p. 5221-31.

366. Huang, L.E., et al., *Activation of hypoxia-inducible transcription factor depends primarily upon redox-sensitive stabilization of its alpha subunit.* J Biol Chem, 1996. **271**(50): p. 32253-9.

367. Thienpont, B., et al., *Tumour hypoxia causes DNA hypermethylation by reducing TET activity.* Nature, 2016. **537**(7618): p. 63-68.

368. Zhu, H. and H.F. Bunn, *Oxygen sensing and signaling: impact on the regulation of physiologically important genes.* Respir Physiol, 1999. **115**(2): p. 239-47.

369. Kallio, P.J., et al., *Activation of hypoxia-inducible factor 1alpha: posttranscriptional regulation and conformational change by recruitment of the Arnt transcription factor.* Proc Natl Acad Sci U S A, 1997. **94**(11): p. 5667-72.

370. Zheng, L., C.J. Kelly, and S.P. Colgan, *Physiologic hypoxia and oxygen homeostasis in the healthy intestine. A Review in the Theme: Cellular Responses to Hypoxia.* Am J Physiol Cell Physiol, 2015. **309**(6): p. C350-60.

371. Taylor, C.T. and S.P. Colgan, *Hypoxia and gastrointestinal disease.* J Mol Med (Berl), 2007. **85**(12): p. 1295-300.

372. Ziegler, A., L. Gonzalez, and A. Blikslager, *Large Animal Models: The Key to Translational Discovery in Digestive Disease Research.* Cell Mol Gastroenterol Hepatol, 2016. **2**(6): p. 716-724.

373. Gonzalez, L.M., et al., *Preservation of reserve intestinal epithelial stem cells following severe ischemic injury.* Am J Physiol Gastrointest Liver Physiol, 2019. **316**(4): p. G482-G494.

374. Wang, Y., et al., *Long-Term Culture Captures Injury-Repair Cycles of Colonic Stem Cells.* Cell, 2019. **179**(5): p. 1144-1159 e15.

375. Camara-Lemarroy, C.R., *Remote ischemic preconditioning as treatment for non-ischemic gastrointestinal disorders: beyond ischemia-reperfusion injury.* World J Gastroenterol, 2014. **20**(13): p. 3572-81.

376. Chen, Y., et al., *Ischemic preconditioning increased the intestinal stem cell activities in the intestinal crypts in mice.* J Surg Res, 2014. **187**(1): p. 85-93.

377. Hundscheid, I.H., et al., *The Human Colon Is More Resistant to Ischemia-reperfusion-induced Tissue Damage Than the Small Intestine: An Observational Study.* Ann Surg, 2015. **262**(2): p. 304-11.

378. Yao, M., et al., *Mixing and delivery of multiple controlled oxygen environments to a single multiwell culture plate.* Am J Physiol Cell Physiol, 2018. **315**(5): p. C766-C775.

379. Tian, H., et al., *Opposing activities of Notch and Wnt signaling regulate intestinal stem cells and gut homeostasis.* Cell Rep, 2015. **11**(1): p. 33-42.

380. Pinto, D., et al., *Canonical Wnt signals are essential for homeostasis of the intestinal epithelium.* Genes Dev, 2003. **17**(14): p. 1709-13.

381. Formeister, E.J., et al., *Distinct SOX9 levels differentially mark stem/progenitor populations and enteroendocrine cells of the small intestine epithelium.* Am J Physiol Gastrointest Liver Physiol, 2009. **296**(5): p. G1108-18.

382. Gracz, A.D., S. Ramalingam, and S.T. Magness, *Sox9 expression marks a subset of CD24-expressing small intestine epithelial stem cells that form organoids in vitro.* Am J Physiol Gastrointest Liver Physiol, 2010. **298**(5): p. G590-600.

383. Barker, N., et al., *Identification of stem cells in small intestine and colon by marker gene Lgr5.* Nature, 2007. **449**(7165): p. 1003-7.

384. Schuijers, J., et al., *Robust cre-mediated recombination in small intestinal stem cells utilizing the olfm4 locus.* Stem Cell Reports, 2014. **3**(2): p. 234-41.

385. Schuijers, J., et al., *Ascl2 acts as an R-spondin/Wnt-responsive switch to control stemness in intestinal crypts.* Cell Stem Cell, 2015. **16**(2): p. 158-70.

386. Sato, T. and H. Clevers, *Growing self-organizing mini-guts from a single intestinal stem cell: mechanism and applications.* Science, 2013. **340**(6137): p. 1190-4.

387. Wang, Y., et al., *Capture and 3D culture of colonic crypts and colonoids in a microarray platform.* Lab Chip, 2013. **13**(23): p. 4625-34.

388. Gjorevski, N., et al., *Designer matrices for intestinal stem cell and organoid culture.* Nature, 2016. **539**(7630): p. 560-564.

389. Ebbesen, P., et al., *Hypoxia, normoxia and hyperoxia--terminology for medical in vitro cell biology.* Acta Oncol, 2000. **39**(2): p. 247-8.

390. Koopman, G., et al., *Annexin V for flow cytometric detection of phosphatidylserine expression on B cells undergoing apoptosis.* Blood, 1994. **84**(5): p. 1415-20.

391. Dawson, A.M., D. Trenchard, and A. Guz, *Small bowel tonometry: assessment of small gut mucosal oxygen tension in dog and man.* Nature, 1965. **206**(987): p. 943-4.

392. Matheson, P.J., et al., *Glucose-induced intestinal hyperemia is mediated by nitric oxide.* J Surg Res, 1997. **72**(2): p. 146-54.

393. Bellio, M.A., et al., *Physiological and hypoxic oxygen concentration differentially regulates human c-Kit+ cardiac stem cell proliferation and migration.* Am J Physiol Heart Circ Physiol, 2016. **311**(6): p. H1509-H1519.

394. Zhi, X., et al., *Physiological Hypoxia Enhances Stemness Preservation, Proliferation, and Bidifferentiation of Induced Hepatic Stem Cells.* Oxid Med Cell Longev, 2018. **2018**: p. 7618704.

395. Guo, C.W., et al., *Culture under low physiological oxygen conditions improves the stemness and quality of induced pluripotent stem cells.* J Cell Physiol, 2013. **228**(11): p. 2159-66.

396. Estrada, J.C., et al., *Culture of human mesenchymal stem cells at low oxygen tension improves growth and genetic stability by activating glycolysis.* Cell Death Differ, 2012. **19**(5): p. 743-55.

397. Jin, X., et al., *Interleukin-6 is an important in vivo inhibitor of intestinal epithelial cell death in mice.* Gut, 2010. **59**(2): p. 186-96.

398. Jeffery, V., et al., *IL-6 Signaling Regulates Small Intestinal Crypt Homeostasis.* J Immunol, 2017. **199**(1): p. 304-311.

399. Bell, B.I., et al., *Interleukin 6 Signaling Blockade Exacerbates Acute and Late Injury From Focal Intestinal Irradiation.* Int J Radiat Oncol Biol Phys, 2019. **103**(3): p. 719-727.

400. Sato, T., et al., *Long-term expansion of epithelial organoids from human colon, adenoma, adenocarcinoma, and Barrett's epithelium.* Gastroenterology, 2011. **141**(5): p. 1762-72.

401. Miyoshi, H. and T.S. Stappenbeck, *In vitro expansion and genetic modification of gastrointestinal stem cells in spheroid culture.* Nat Protoc, 2013. **8**(12): p. 2471-82.

402. Rivera, K.R., et al., *Measuring and regulating oxygen levels in microphysiological systems: design, material, and sensor considerations.* Analyst, 2019. **144**(10): p. 3190-3215.

403. Bray, N.L., et al., *Near-optimal probabilistic RNA-seq quantification.* Nat Biotechnol, 2016. **34**(5): p. 525-7.

404. Huber, W., et al., *Orchestrating high-throughput genomic analysis with Bioconductor.* Nat Methods, 2015. **12**(2): p. 115-21.

405. Love, M.I., W. Huber, and S. Anders, *Moderated estimation of fold change and dispersion for RNA-seq data with DESeq2.* Genome Biol, 2014. **15**(12): p. 550.

406. Robinson, M.D., D.J. McCarthy, and G.K. Smyth, *edgeR: a Bioconductor package for differential expression analysis of digital gene expression data.* Bioinformatics, 2010. **26**(1): p. 139-40.

407. Carbon, S., et al., *AmiGO: online access to ontology and annotation data.* Bioinformatics, 2009. **25**(2): p. 288-9.

408. Huang da, W., B.T. Sherman, and R.A. Lempicki, *Bioinformatics enrichment tools: paths toward the comprehensive functional analysis of large gene lists.* Nucleic Acids Res, 2009. **37**(1): p. 1-13.

409. Huang da, W., B.T. Sherman, and R.A. Lempicki, *Systematic and integrative analysis of large gene lists using DAVID bioinformatics resources.* Nat Protoc, 2009. **4**(1): p. 44-57.

410. Lugg, G.A., *Diffusion Coefficients of Some Organic and Other Vapors in Air.* Analytical Chemistry, 1968. **40**(7): p. 1072-&.